DOCTORAL COURSE IN

TRANSLATIONAL NEUROSCIENCE AND NEUROTECHNOLOGIES

CYCLE XXXV

COORDINATOR Prof. Fadiga Luciano

OPTIMIZATION OF TIME-RESPONSE AND AMPLIFICATION FEATURES OF EGOTs FOR NEUROPHYSIOLOGICAL APPLICATIONS

Scientific/Disciplinary Sector (SDS) BIO/09

Candidate

Dott. De Salvo Anna

_____

(firma)

Supervisor

Prof. Biscarini Fabio

_____

(firma)

Co-Tutor

Dott. Di Lauro Michele

_____

(firma)

Anni 2019/2023

"Science is a journey, not a destination,
And you just can't tell just what tomorrow brings."

Contents

Abstract

In device engineering, basic neuron-to-neuron communication has recently inspired the development of increasingly structured and efficient brain-mimicking setups in which the information flow can be processed with strategies resembling physiological ones. This is possible thanks to the use of organic neuromorphic devices, which can share the same electrolytic medium and adjust reciprocal connection weights according to temporal features of the input signals. In a parallel - although conceptually deeply interconnected - fashion, device engineers are directing their efforts towards novel tools to interface the brain and to decipher its signalling strategies. This led to several technological advances which allow scientists to transduce brain activity and, piece by piece, to create a detailed map of its functions. This effort extends over a wide spectrum of length-scales, zooming out from neuron-to-neuron communication up to global activity of neural populations. Both these scientific endeavours, namely mimicking neural communication and transducing brain activity, can benefit from the technology of Electrolyte-Gated Organic Transistors (EGOTs).

Electrolyte-Gated Organic Transistors (EGOTs) are low-power electronic devices that functionally integrate the electrolytic environment through the exploitation of organic mixed ionic-electronic conductors. This enables the conversion of ionic signals into electronic ones, making such architectures ideal building blocks for neuroelectronics. This has driven extensive scientific and technological investigation on EGOTs. Such devices have been successfully demonstrated both as transducers and amplifiers of electrophysiological activity and as neuromorphic units. These promising results arise from the fact that EGOTs are active devices, which widely extend their applicability window over the capabilities of passive electronics (i.e. electrodes) but pose major integration hurdles. Being transistors, EGOTs need two driving voltages to be operated. If, on the one hand, the presence of

two voltages becomes an advantage for the modulation of the device response (e.g., for devising EGOT-based neuromorphic circuitry), on the other hand it can become detrimental in brain interfaces, since it may result in a non-null bias directly applied on the brain. If such voltage exceeds the electrochemical stability window of water, undesired faradic reactions may lead to critical tissue and/or device damage.

This work addresses EGOTs applications in neuroelectronics from the above-described dual perspective, spanning from neuromorphic device engineering to in vivo brain-device interfaces implementation. The advantages of using three-terminal architectures for neuromorphic devices, achieving reversible fine-tuning of their response plasticity, are highlighted. Jointly, the possibility of obtaining a multilevel memory unit by acting on the gate potential is discussed. Additionally, a novel mode of operation for EGOTs is introduced, enabling full retention of amplification capability while, at the same time, avoiding the application of a bias in the brain. Starting on these premises, a novel set of ultra-conformable active micro-epicortical arrays is presented, which fully integrate in situ fabricated EGOT recording sites onto medical-grade polyimide substrates. Finally, a whole organic circuitry for signal processing is presented, exploiting ad-hoc designed organic passive components coupled with EGOT devices. This unprecedented approach provides the possibility to sort complex signals into their constitutive frequency components in real time, thereby delineating innovative strategies to devise organic-based functional building-blocks for brain-machine interfaces.

Chapter 1: Organic Bioelectronics

This introductive chapter defines the vision of this work.
Starting with the duality between brain and brain-inspired technological advancements, the fundamental aspects of bioelectronics and neurophysiology are presented, leading to the use of organic bioelectronics in neuromorphic circuits and translational neuroscience.

Introduction

Present-day society has access to a large amount of information which can spring from a variety of sources, ranging from the Internet to physiological systems. However, developing meaningful methods for information extraction, processing, and representation is still under investigation. Most technological attempts to manage this vast amount of information in an energy-efficient manner have been closely linked to the understanding and the imitation of the inner-principles of brain data processing.

Animals and humans can be regarded as *machines* living in a complex environment that continuously overloads their senses with information that may be crucial to establish social bonding or to decide their next course of action. Therefore, the brain constantly filters out irrelevant data while integrating relevant ones into an internal representation that is used to predict what is next. This complexity leads to the transformation of endogenous and exogenous signals into a sophisticated mixture of electrical and chemical signals that constitute the core currency upon which computations are run by the Central Nervous System (CNS).

Neurons, which are electrically excitable cells that originate and transmit basic communication events in biological signal processing, are the building blocks of the brain network. They are linked to one another via synapses, which are nanogap junctions between neuronal cells. When a neuron accumulates signals above a certain threshold, it fires an action potential (i.e., an electrical impulse) towards the next cells via the axon, eliciting the release of chemical neurotransmitters from the presynaptic to the postsynaptic neuron (i.e., chemical synapses), or modulating the voltage of the postsynaptic neuron with ionic currents when the action potential arrives at the presynaptic neuron (i.e., electrical synapses). Electrical activity at the presynaptic neuron modifies the connection strength between the pre- and post-synaptic neurons in both types of synapses, which may be quantified

and characterized referring to the synaptic weight, *w*. Synaptic plasticity refers to changes of *w* in time, which can occur over a wide range of periods. Short-term Plasticity (STP) is associated with various computing activities and can last from milliseconds to minutes, whereas Long-term Plasticity (LTP) is considered the biological substrate for learning and memory and can endure from minutes to the lifetime of the brain itself [1,2].

These neural processing phenomena are the primary source of inspiration for artificial neural networks and brain-like computing implementations, which are frequently based on specific algorithms that mimic the working principles of the brain and are implemented in software, i.e., artificial neural networks, ANNs. ANNs are commonly executed on conventional computers that run tasks sequentially, in stark contrast with what happens in the brain, which performs computational tasks in parallel, through a densely interconnected network of neurons. Owing to parallel "computing", the brain can recognize patterns and perform tasks with remarkable precision [3]. Emulating synaptic functionality would be highly desirable to perform neural network algorithms with comparable energy efficiency and interconnectedness to that of the brain. In ANNs, each synaptic weight is simulated by a hardware-based tunable non-volatile resistive memory element. The resistance state of such non-volatile memory device is the sole repository of the information. Bioinspired devices, on the other hand, can be used to simulate additional neuromorphic functions such as spike-timing-dependent plasticity (STDP), and short-term and long-term potentiation [4,5]. Developing devices and architectures capable of performing neuro-inspired information processing at the interface with biological environment remains a challenge.

Organic materials and electronics have recently emerged as neural processing building blocks [6], with basic forms of neuroplasticity capable of mimicking brain functionality at the device level [7]. Organic electronic materials, in contrast with their inorganic counterparts, exhibit highly desirable properties for the development of bio-integrable electronics, such as biocompatibility, softness, and structural conformability, as well as mixed

ionic-electronic conduction. They are also solution-processable and can be functionalized to tune their properties, enabling the high-throughput development of a variety of materials featuring different levels of conductivity and time responses, which are both key enabling features for envisioning the functional core of efficient neuromorphic computing systems [8,9]. Organic neuromorphic devices have been demonstrated to show multiterminal operation, global connectivity control due to their ability to operate in shared electrolytes[9,10], and multifaceted circuitry applications to implement artificial neural systems [8,11]. Additionally, their time-response has been shown to be sensitive to the chemical composition of the environment and, thus, they have been used as selective sensors for neurotransmitters [12,13].

Starting from these two-electrodes neuromorphic organic devices, and aiming at multi-level memory storage, significant effort has been devoted to repurpose the three-terminal Electrolyte-Gated Organic Transistors (EGOTs) architecture for neuromorphic applications. This resulted in the achievement of a greater number of programmable memory states [7,14].

EGOTs feature three electrodes, named source (S), drain (D) and gate (G). The S electrode is grounded and connected with the D by means of a (semi-)conductive polymer film, which forms the 'channel', meanwhile an electrolyte solution puts the channel in communication with the G electrode. With respect to S, two driving voltages are applied at D and G. A current - I_{DS} - flows in the channel when a voltage - V_{DS} - is applied between D and S. Magnitude of this current depends on the resistance of the channel which, for a certain class of semi-conductive organic materials, is a function of the ion concentration in close proximity to the channel. By arbitrarily modulating the potential at G with respect to S - V_{GS} – it is possible to set the electrochemical potential of the electrolyte, which governs the ionic density at the channel/electrolyte interface and, ultimately, the channel resistance. EGOTs offer the possibility of modulating channel resistance of several orders of magnitude at low operational voltages (-1 V <V< 1 V), while contextually enabling the conversion of ionic currents into electrical ones. Additionally,

they can be finely tuned by means of operational and/or fabrication variables, thus establishing themselves as a technology of great interest for implementing electronic devices for interfacing aqueous environment of different nature and complexity and for mimicking the conductance non-linearity of biological electro-active units.

As a consequence, a dual and bidirectional nature of the relationship between EGOTs and brain can be envisioned: if, on the one hand, synaptic communication mechanisms inspire the development of ever more complex EGOT-based organic neuromorphic devices and circuitry, on the other hand EGOTs may prove themselves as powerful tools for transducing brain activity, zooming out from the neuro-to-neuron communication and focusing on the global outcome of the electrical activity of a neural population, namely on the transduction of local field potential (LFP)[15].

It is well known that neurons account for roughly half of the brain cell population. The remaining part of the nervous tissue is constituted by glial cells, which include astrocytes, oligodendrocytes, and microglia[16,17]. As a result, according to the distribution of current flow in a volume conductor, any type of transmembrane current arising from excitable cells within a volume of brain tissue superimposes to the neighbouring ones at a given point in the extracellular medium, thus generating a potential with respect to a reference location, giving rise to an electric field, which for all ionic processes in that volume. Such processes cover a wide spectrum of timescales, from fast action potentials (in the range of milliseconds) to the slowest fluctuations (in the range of seconds), leading to a fluctuating cumulative voltage, the LFP. The amplitude and frequency of the LFP waveform are determined by the proportional contribution of the multiple sources as well as the various properties of the brain tissue[15]. Of course, the distance between the signal source and the recording site influences the measurement of electrical potential.

Extracellular electrodes are currently the most promising interfaces for recording local field potentials, spikes, and multi-unit activity with high spatial-temporal resolution and signal-to-noise ratio (SNR)[15,18,19]. The miniaturization of microelectrodes and the fabrication of high-density micro-electrocorticography (µ-ECoG) arrays allow neuroscientists to record the orchestrated/synchronized activity underlying neural network functions with unprecedented spatial and temporal resolution, as well as to precisely stimulate selected neuronal ensembles[20,21]. Smaller microelectrodes, however, yield biotic/abiotic interfaces with higher electrolyte resistance and lower double layer capacitance with respect to larger microelectrodes, resulting in higher impedance[22,23]. Since the ability to record biological signals is determined by impedance (i.e., the electrical resistance to alternating current flow) itself, extreme miniaturization, while increasing spatial resolution, severely hampers recording capability. Other issues that may arise from electrode miniaturization include electromagnetic coupling between adjacent lines (crosstalk)[24], chemical instability of the electrode surface, and integration challenges due to high density small connectors and leads [25,26]. Furthermore, since thermal noise scales with electrode impedance, reducing the electrode size is expected to reduce the output SNR [27]. This, coupled with signal loss via shunt pathways electronic noise from the amplifier and flicker noise, can have a dramatic effect on SNR in vivo[28,29]. In this complex scenario, where chemical, electrochemical, and biological aspects are intertwined, the selection of electrode material is extremely difficult since no individual material is likely to possess all the desirable properties.

Conductive polymers (CPs) have emerged as an appealing class of materials in the last two decades due to their highly porous structure, which contributes a large electroactive area, low impedance, mixed ionic-electronic conduction, and high charge storage capacitance (CSC). As a result, there has been a growing interest in the neuroelectronics community about CPs, fuelled by the possibility of creating high-performance neural

recording devices[30]. Additionally, CPs can be engineered in transistor devices, such as EGOTs, which may overcome the inherent limitation of increased noise resulting from miniaturization by providing in situ amplification of ECoG signals.

The primary distinction between a transistor and an electrode is that the former is an active device that behaves as a voltage-controlled current amplifier. A voltage-controlled current amplifier converts small voltage modulations at the gate electrode into big current modulations in the drain-source channel, thus amplifying in situ the ECoG signal and increasing SNR[31].

Neural activity manifests itself as a wide range of oscillations with varying frequencies. These neural oscillations are typically classified as two types of voltage signals: slow varying potentials (LFPs with frequencies below 300 Hz) and fast varying potentials (LFPs with frequency above 300 Hz and spikes). Analogue and digital filters can be applied to raw data to selectively separate signals in lower and higher frequency bands[15,32] and to decouple it in all its constitutive frequency bands whenever it is necessary to discriminate frequency-dependent events[33]. If such discrimination capability was implemented in closed-loop brain machine interfaces, it would enable management and treatment of chronic diseases only in response to specific symptomatic episodes, thereby minimizing the side effects of overuse and improving compliance. This remains a major open challenge in biomedical fields[34].

By using organic moieties as substrates and as active (semi-)conducting materials in biotic/abiotic interfaces, organic bioelectronics can help to overcome problems related to biocompatibility and durability of devices used in the biological environment [35,36]. Furthermore, the well-established mixed ionic-electronic conduction of CPs coupled with the amplification and filtering properties of EGOT architectures may be advantageous to implement novel organic circuits suitable not only for recording and transmitting electrophysiological data but also for data processing and

memorization, paving the way for a novel class of neuroelectronic building-blocks for brain-machine interfaces.

Electrolyte-gated organic transistors, which have been validated as both neuromorphic devices and recording sites for electrophysiological activity in vivo, are the mainstays of this work. The devices time-response, i.e., their neuromorphic behaviour, is explored in Chapter 2 and Chapter 5, in relation to short-term plasticity, short-term potentiation and paired-pulse plasticity (PPP) by acting on both gate potential and drain potential. The translational aspects of EGOTs are introduced in Chapter 2, and extensively discussed in Chapter 6, which presents a novel connection scheme to ensure a safe in vivo amplification of the electrophysiological signal. A whole organic circuit for signal amplification and sorting is also presented, leveraging ad-hoc designed organic passive components, such as capacitors and resistors, coupled with EGOT devices. Epicortical flexible transistor arrays ready for translation are presented and validated at the bench-side.

The findings of this thesis have a dual impact on the newly born scientific field of organic neuroelectronics by demonstrating tunable neuromorphic devices with real-time signal processing features and fostering the development of safe and efficient transistor-based ECoG arrays, **Figure 1**.
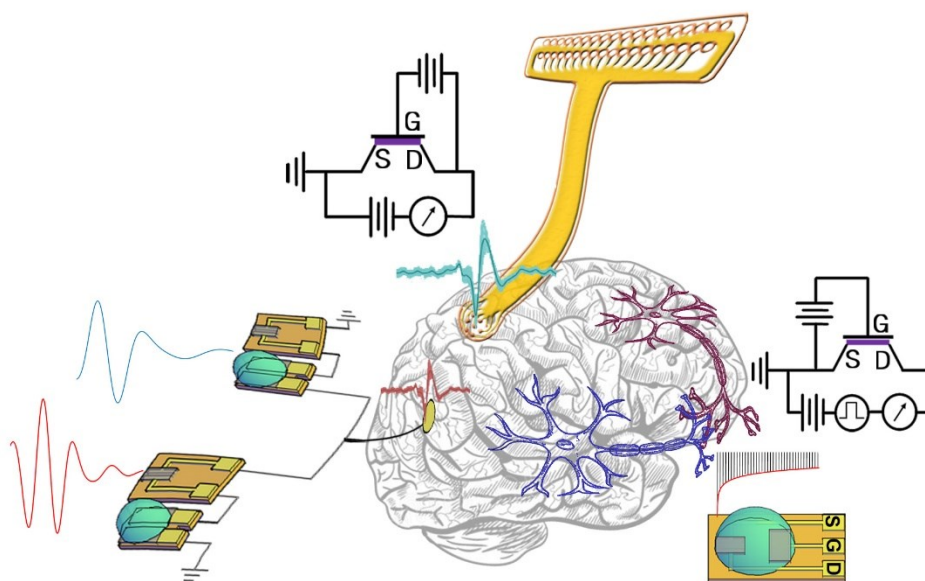
Figure 1. Vision. Multifaceted application of organic transistors as brain interfaces. As neuromorphic device (bottom right), micro-electrocorticography array featuring electrolyte-gated organic transistors as recording sites(top), whole organic circuit for real-time sorting (bottom left).

1.Bioelectronics: biotic/abiotic interface aspects

Everything in our universe communicates via an interface. Interfacial communication can be mediated by a variety of mechanisms, making interface research a fundamental trait shared by many different research fields. Within this framework, a significant challenge is to interface artificial devices with living systems, establishing connections between living matter (i.e., cells, the human brain, tissues, etc.) and electronic devices aimed at probing biological reactions (e.g., biosensors) or inducing biological processes in a controlled manner (e.g., pacemakers, cochlear implants, and stimulation/recording electrode systems).

When biological and electronic worlds collide, a new intersectional scientific and technological field, commonly known as *bioelectronics*, emerges. Since biological signal carriers are mainly ions and molecules, whereas electronic communication is established mainly by electron flow, achieving efficient bidirectional communication at the interface crucially demands the conversion of molecular/ionic signals into electrical ones. The term "bidirectional" refers to data flow in both directions, **Figure 2**. Consequently, *bioelectronics* is a research field that is heavily reliant on the materials used for the fabrication of devices that are promptly translatable to interact directly with at biological interfaces. Neural interfaces are a case-in-point of this conceptual, scientific, and technological framework.

Neuroelectronic devices are essential bioelectronic tools for the detection and treatment of disorders of the nervous system. Indeed, taking advantage of neural interfaces as therapeutic tools allowed great feedback in the treatment of several neurological disorders (e.g., epilepsy, Parkinson's disease, or essential tremor) [37–39]. Likewise, their implementation in brain computer interfaces (i.e., BCI) applications is enabling the rehabilitation of severely motor-impaired patients [40–42]. Even so, any neural probe implanted into the body sets off an unavoidable chain of events that leads to its attack and encapsulation, known as the foreign body reaction (FBR)[43,44]. The

process of implantation injures the tissue around the foreign object, which triggers an inflammatory process. Over a period of weeks to months this inflammatory process develops into a fibrotic response, which encapsulates and isolates the implanted material [45]. Medical devices must remain in contact with their target tissue for extended periods of time to work properly. Tissue and devices continue to interact at their interface over time. While this interaction can be minimally harmful, an improperly designed device can cause a severe reaction in the tissue and potentially destroy the target of interest. The degree to which a device can be harmlessly implanted in a surrounding tissue is known as biocompatibility, and the failure of the tissue-implant interface is one of the leading causes of failure in medical devices [46]. Aiming at the development of highly biocompatible interfaces, soft or flexible devices are being extensively explored. Material selection is part of this complex developmental effort. A material may be 'too soft' for one site or application while being 'too hard' for another. Materials' mechanical properties can influence critical feature dimensions, which can then determine device shape and biocompatibility[47]. The Young's modulus, which measures material stiffness, is directly related to implant compliance. The stiffness of brain tissue is about 1 kPa, while that of silicon is more than 100 GPa. As a result, the interaction between the brain and silicon-based electronics is far from ideal, resulting in major trauma and scarring[48,49]. Polymers are an excellent alternative, with a wide range of lower stiffness values. Because of their compatibility with MEMS (microelectromechanical systems) processing, parylene and polyimide have emerged as strong candidates for implant miniaturization. These two polymers have Young's moduli below 9 GPa and can be processed to yield ultra-thin films (< 10 μm) which are sufficiently robust to engineer highly fenestrated geometries, enabling a significant reduction of the bending stiffness and ensuring compliance to brain tissue[26,50]. MuSA and NeuroGrid are examples of epicortical implants that can conform to the brain's smallest curvatures, creating a tight and stable interface between implant and tissue [51,52].

Another critical aspect concerning integration, besides the stiffness of a device, is the bio-chemical interaction between recording site and the biological medium, which can be a cell culture medium or a biological fluid or tissue. Electrodes for neural interfaces must be made of materials with high chemical and mechanical stability to prevent degradation, corrosion, and eventual diffusion of toxic products into the tissue. Classical examples of such materials include polarisable electrodes with low surface reactivity, such as platinum and gold.

Ion transport in the brain regulates neural communication by generating electrical currents that give rise to dynamic electric fields in the brain volume, which can be sensed and measured by electrodes as potential fluctuations with respect to a reference potential [53–55]. In salt water, Pt or Au electrodes are inert, which means that there is little to no charge transfer between metal and electrolyte via redox reactions. Conversely, charge is capacitively stored at the interface. This class of electrodes is known as polarisable electrodes, a term indicating the build-up of large potential deviations from the equilibrium potential with virtually no change in current density[56]. When a polarisable electrode contacts an aqueous electrolyte, water molecules create a phase boundary between the solid and liquid states[53,57]. Water dipoles adhere to the electrode surface and, depending on the electrode surface charge, hydrated cations and anions are repelled or attracted to the interface. Hydrated cations are attracted to the interface of a negatively charged electrode, covering the water dipole layer along the so-called outer Helmholtz layer (OHL). A double layer capacitor is formed by the accumulation of opposing charge on both sides of the phase boundary. In a nutshell, polarisable electrodes allow potential oscillations from the brain to be picked up by charging and discharging the double layer capacitor. Since double layer capacitance is inversely proportional to electrochemical impedance, the higher the capacitance of the interface, the lower its impedance, improving electrode recording performances[53,57]. Nonetheless, planar Pt and Au electrodes are characterized by a high interfacial

impedance, which is a limitation for their recording applications, especially in the case of miniaturised electrodes. Considering this argument, efforts are being made to modify/functionalize the microelectrode surface to reduce overall impedance and achieve high-quality recordings, particularly in the case of high-density small recording sites. One of the most pursued approaches towards this aim is the roughening of the electrode surface to increase its electroactive area and reduce its impedance. This resulted in flake-like gold or nanostructured platinum electrodes showing impedance values orders of magnitude lower than pristine smooth electrodes [58,59]. Electrochemical oxidation or sputtering can also be used to grow smooth or
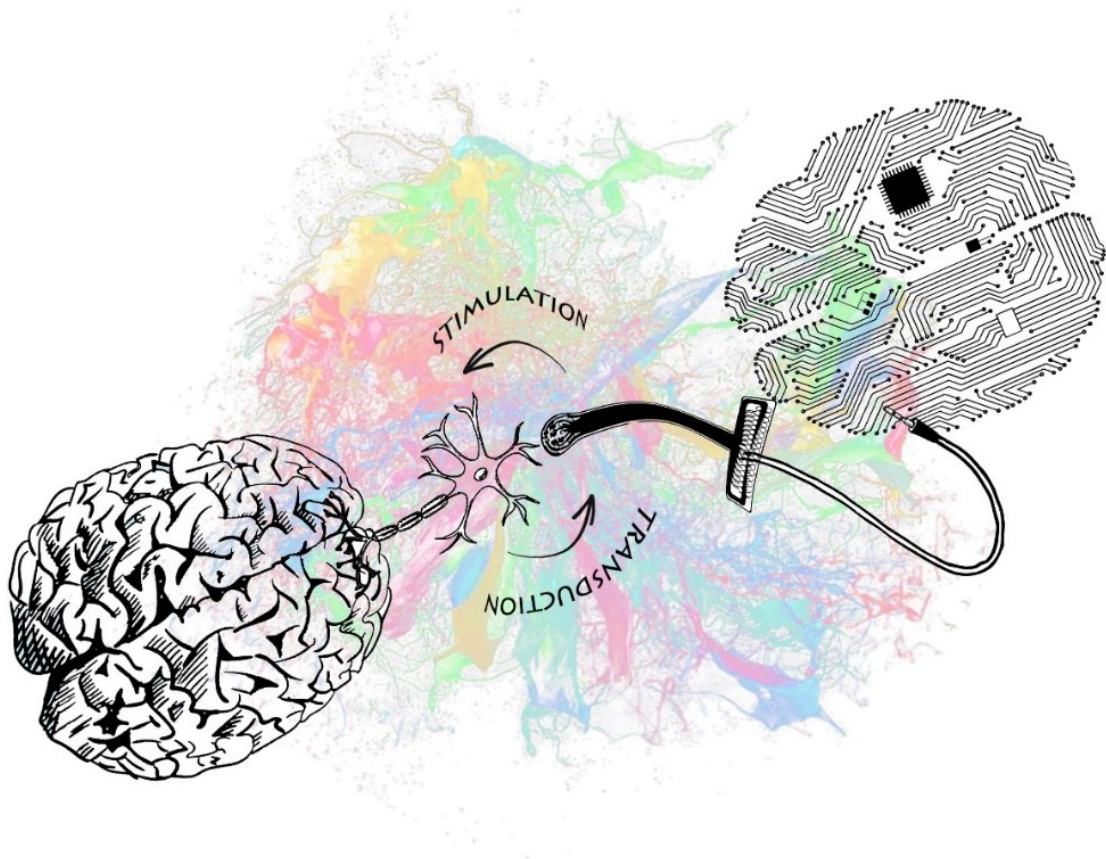
Figure 2. Bidirectional communication between biological and electronic worlds. A biological phenomenon is transduced by a bioelectronic device; an electrical stimulus activates a biological process.

porous oxide layers on the electrode surface[60]. However, activated metal oxide layers can undergo further electrochemical reactions and passivate with time in chronic implants, leading to the deterioration of recording

capability over time[22]. In addition, the release of potentially harmful metal ions in the peri-implant environment by electrochemical processes has not been deeply investigated so far[44,61,62].

To provide solutions to this deeply entangled scientific problem, where mechanical, chemical, electrochemical, and biological aspects are intertwined, the selection of materials for electrode fabrication is challenging, since any material choice arise from compromise consideration and an individual material possessing all the desirable properties has not been identified yet.

Keeping this in mind, it is worth remarking how conductive polymers (CPs) have emerged in the last two decades as appealing materials for bioelectronic interfaces, due to their highly porous structure, which contributes a large electroactive area, low impedance, mixed ionic-electronic conduction, high charge storage capacitance (CSC). Furthermore, CPs often are highly biocompatible and can be biofunctionalised. As a result, since they match a vast majority of the requirements regarding biocompatibility, material science, chemical and electrochemical aspects which define the guidelines for obtaining high-quality bioelectronic devices for bidirectional communication, CPs have been identified as good candidate materials for next generation neuroelectronics.

1.1 Conductive polymers

Conductive polymers (CPs) are a versatile class of materials with applications ranging from the microelectronics industry (including solar cells, antistatic coatings, and energy storage technology)[63,64] to biomedical applications[22,62]. CPs are conjugated polymers with conductivities greater than 1000 S cm^{-1}, comparable to metals or highly doped inorganic

semiconductors, **Figure 3**. They are characterised by a system of extensively delocalized π-molecular orbitals and, because of delocalization, charge-separated states of these molecules (i.e., their oxidized or reduced form) are stable and long-living. Due to these characteristics, the charged states behave as "quasi-particles," with the ability to drift and diffuse across the material. For this, these charged states are also known as charge-carriers. Chemical synthesis (condensation or addition polymerization reactions), electrochemical polymerization, and photo-induced oxidation are all methods for obtaining CPs by oxidative coupling of monomers [65].

Charge transport in CPs, like in organic molecular semiconductors, occurs via hopping between localized Wannier states, in contrast to metals, where electrons can occupy any position in the conduction band. The term "doping," lexically borrowed by the semiconductor field, refers to the generation of charge carriers in CPs, either through the injection of extra electrons (i.e., reduction or n-type doping) or the removal of electrons (i.e., oxidation or p-type doping), resulting in so-called "holes" that can be transported across the conjugated polymer backbone upon application of an external bias. In the most basic and common scenario, when a bias is applied to a p-type CP film between two electrodes, holes are injected (electrons are removed) at the positive electrode and collected at the negative one, resulting in a cascade of localized oxidation reactions that proceed from the positive to the negative electrode. During CP synthesis, doping can occur either chemically or electrochemically, resulting in charge carriers that are typically in the form of polarons (radical anions/cations) or bipolarons (dianions/dications). During device operation, the amount of mobile charge carriers can be controlled electrostatically, allowing switching between insulating and conductive regimes [66].

Many intrinsic and extrinsic parameters influence the conductive properties of CPs, including charge carrier density, delocalization length scale of π-electrons and structural defects, intra-and inter-chain interactions, interaction of charge carriers with other charges (e.g., (counter)ions, static

charge) and dipoles (either from polarization of the material, water, solvent) or reactive species (oxygen, peroxides, superoxides), morphology, crystallinity, and processing parameters[67–69]. The high chemical versatility, compliant mechanical properties, compatibility with a wide range of cell types, and low impedance over a wide frequency bandwidth make CPs ideal materials for improving the recording performance of conventional metal-based neural interfaces[70–72]. The coupled electronic and ionic transport exhibited by a specific subset of CPs known as organic mixed ionic-electronic conductors (OMIECs) is particularly interesting for neuroelectronic applications [73]. OMIECs support both electronic charge transport along the π-conjugated polymer chain and ionic transport through the bulk, which explains their high (pseudo)capacitance.

OMIECs are classified basing on their polymeric structure (i.e., heterogeneous blend/co-polymer or homogeneous single-component polymer) or on the base of exposition of an ionic moiety (or a stabilized charge carrier) along their chains. OMIECs can incorporate ions during
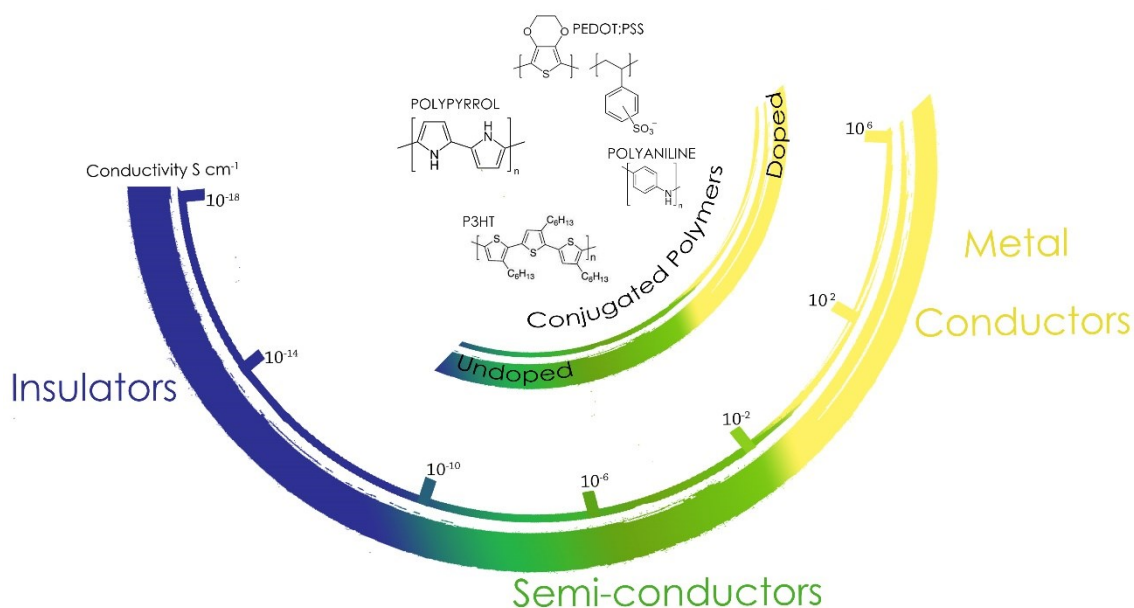
Figure 3. Organic (semi-)conductors. On the top, polyaniline (PA), polypyrrole (PPy), polythiophene (P3HT), and poly(3,4-ethylenedioxythiophene):poly-(styrene sulfonate) (PEDOT:PSS), four of the most common CPs used for neural applications. Inner semicircle, sketch of the conductivity range encompassed by (undoped and doped) conjugated polymers. Outer semicircle, sketch of the conductivity ranges from insulator to metal conductors.

deposition or directly after exposure to the electrolyte, in the case of non-intrinsically charged polymers.

Electronic transport, ionic transport, and ionic-electronic coupling are the fundamental processes that determine the characteristic figures of merit of OMIEC-based devices. In general, these processes are not independent (due to their highly complex and still partially unknown interplay) and are primarily determined by the material's synthetic design and the processing techniques [74]. It is also worth noting that several CPs have higher charge storage capacity (CSC) and charge injection capacitance limit values than metal and metal oxide electrodes due to their porous structure and high ionic conductivity [70].

Nonetheless, poor adhesion to metals such as Pt and Au, or to alloys such as PtIr, as well as swelling upon hydration and conductivity drifting, particularly under cyclic stress conditions, have severely limited the use of CPs in chronic applications to date[75,76]. Notably, it has recently been reported that it is possible to ensure long-term adhesion by modifying the surface of metal electrodes, for example, by increasing roughness as in the case of nanostructured Pt or gold electrodes, or by growing an adhesion promoter layer of porous iridium oxide (IrOx), capable of establishing a stronger bonding with the CP via carbide bond formation [59,77].

Furthermore, by reducing the mechanical mismatch between the electrode material and the neural tissue, the stability and biocompatibility of the tissue-electrode interface can be improved. The ability of OMIECs to support ion penetration, control the amount of charge carriers during device operation, as well as their non-linear time response, coupled with chemical stability and biocompatibility, has enabled the development of electrolyte-gated organic transistors (EGOTs) for in situ amplification of neural signal [52,72], organic ion pumps for on-demand release of small molecules and drugs [78,79], and neuromorphic devices [7,8,80].

1.1.1 PEDOT:PSS

PEDOT:PSS is a polymer blend of poly(3,4ethylenedioxythiophene)(PEDOT) and poly-(styrene sulfonate) (PSS), and it is the prototypical OMIEC material as well as the most used CP in bioelectronics. PEDOT:PSS is the first choice as a signal transducing component in bioelectronics devices that operate in aqueous electrolytes or hydrogels, such as EGOT-based biosensors and transducers, low-impedance multi-electrode arrays (MEAs) interfaced with the nervous system, and neuromorphic logic-based devices and sensors[13,81,82]. The presence of two physically distinct, albeit intimately interpenetrated, phases in PEDOT:PSS results in mixed ionic/electronic conductivity, one acting as a hole transport region (PEDOT-rich phase) and the other as an ion transport region (PSS-rich phase). Atomic force microscopy (AFM) can detect multiscale phase separation on length scales ranging from nanometers to mesoscopic length scales [83].

One of the most desirable properties of PEDOT:PSS for bioelectronic applications is the large effective capacitance of its interfaces with aqueous electrolytes. For relatively small amounts of polymer, such as those used in EGOTs and microelectrodes, the capacitance of PEDOT:PSS is linearly correlated to its volume [84,85]. However, deviations from this trend have been reported at higher polymer volumes, due to incomplete film hydration and electroactive area saturation[12].

The oxidation and polymerization of the 3,4-ethylenedioxythiophene (EDOT) monomer demands the presence of a counterion to ensure solubility and to stabilize the otherwise unbalanced positive charges introduced either chemically or electrochemically in the PEDOT backbone. When carried out in the presence of PSS counter ion it yields a p-type highly doped semiconductor with conductivities around 1 S cm^{-1}. When PEDOT:PSS is chemically synthesized, it forms polymeric particles with positively charged PEDOT cores surrounded by poly-anionic PSS shells, the latter providing enough stability for PEDOT+ chains to be dispersed in water [86]. Conductive

PEDOT/PSS films can be grown on metal or conductive oxide electrodes by dissolving monomeric EDOT in aqueous solution and applying galvanostatic (constant current) or potentiostatic (constant voltage) procedures in the presence of PSS, allowing mask-less coating [51].

Chemically polymerized PEDOT:PSS is now commercially available in aqueous dispersions with varying conductivity, viscosity, and transparency under the trade name Clevios™, which identifies a family of formulations that differ primarily on the basis of the PEDOT to PSS ratio; as a general trend, conductivity increases with this ratio [87]. Commercial water-dispersed PEDOT:PSS formulations have the distinct advantage of being a commodity, allowing for the simple fabrication of antistatic coatings[88] and devices such as transistors [85,89], memristors [5], solar cells [90], OLEDs [91], and artificial synapses using low-cost additive techniques [7,8]. In general, pristine PEDOT:PSS has conductivities ranging from 0.1 to 10 S cm^{-1} [81], which can be increased using a variety of methods, including the addition of organic compounds such as ethylene glycol (EG) or dimethyl sulphoxide (DMSO) to the PEDOT:PSS aqueous dispersion or the treatment with strong acidic solutions [92]. To further improve film stability in aqueous environment, it is common the addition glycidyloxypropyl-trimethoxysilane, GOPS, to act as surface adhesion promoter and as cross-linking agent.

Such PEDOT:PSS formulations can be easily deposited via spin-coating, yielding transparent films with low sheet resistance [93]. Usually, these films exhibit a peculiar surface morphology, with small grains (diameters in the range of 5 - 20 nm) [83,83]. Since PEDOT chains are typically composed of a few hundred monomer units, the polymer grains are most likely defined by the PSS random coil which embeds charged PEDOT cores. The enlargement of PEDOT grains upon treating PEDOT:PSS films with organic compounds improves electron mobility [94]. Finally, PEDOT is easily modifiable via standard synthetic chemistry routes due to the residual reactivity of the thiophene ring after polymerization, which enables the introduction of ad-hoc and application-specific functional groups in the material backbone.

1.2 Organic Bioelectronics

Bioelectronics is a multidisciplinary field of research that is heavily reliant on technology development and cutting-edge research in chemistry, biology, (micro-)engineering, and physical science. Organic Bioelectronics synergically combines two major fields: bioelectronic devices and conductive polymers development, exploring and exploiting their properties at the interface with biological systems. As previously mentioned, CPs and, in particular, OMIECs, have the advantage of being mechanically flexible, of having a surface structure that is modifiable by standard synthetic chemical processes and of supporting both electronic and ionic charge transport. Importantly, mechanical properties of such materials aid in the reduction of inflammation by reducing strain between tissue and bioelectronic implant, thereby providing interfaces for transduction close to ideality. Wearable electronics [95] , sensors[12] and brain interfaces [51] are only few examples amongst the plethora of devices which have been implemented in this intersectional technological field.

1.3 Organic Neuromorphic Electronics

1.3.1 Communication between neurons

Neurons to communicate with one another via electrochemical processes. While transmembrane potential is propagated within the same neuron as a time-varying gradient of ionic concentrations and therefore can be regarded as merely electrical phenomena involving the propagation of an ionic current, communication between neurons is accomplished through the conversion of electrical signals into chemical signals. As a result, signal transmission through the nervous system demands the constant conversion of electrical signals into chemical signals and vice versa. Each neuron has a cell body (soma) with up to a thousand dendrites and an axon projection.

The cell body houses all the neurons' metabolic and genetic functions. It contains the nucleus as well as a biosynthetic apparatus for the synthesis of all the substances required for the nerve cells' specialized functions. The soma is also where the neuron receives synaptic input (electrical and chemical signals from other neurons). Dendrites are tapering and branching extensions of the soma and are the main direct recipients of signals from other neurons. The axon is an elongated segment deputed to the propagation of action potentials, which terminates in fine branches that form communication sites with dentrites of other neurons. These sites, namely nanogap junctions between neuronal cells, are known as synapses. The nerve cell that sends the signal is known as a presynaptic neuron, while the cell that receives the signal is termed post-synaptic. As previously mentioned, the axon's primary function is to propagate action potentials. An action potential is a rapid change in membrane potential followed by a return to the resting state of the membrane. Voltage-dependent ion channels in the plasma membrane generate action potentials, which propagate along the axon, conserving shape, magnitude and duration. An action potential arises from sequential changes in the membrane's selective permeability to Na^+ and K^+ ions, changing its potential from a rest value of about -65 mV to a peak of roughly 30 mV in a milli-second [96].

According to the Hodgkin-Huxley model, an action potential involves the following sequence of events. A depolarization of the membrane causes Na^+ channels to open rapidly, resulting in an inward Na^+ current. This current, by discharging the membrane capacitance, causes further depolarization, thereby opening more Na^+ channels, resulting in a further increase of the inward current. This regenerative process drives the membrane potential towards an equilibrium, causing the rising phase of the action potential. The depolarizing state of the action potential is self-limited in two ways: (1) it gradually inactivates the Na^+ channels, and (2) it opens, with some delay, the voltage-gated K^+ channels. Consequently, the inward Na^+ current

(depolarization) is followed by an outward K⁺ current that tends to repolarize the membrane [97].

When an action potential reaches a neuron's terminal, the synapse acts as a one-way valve, allowing the neuron's action potential to exert its influence via neurotransmitter release across the synaptic cleft to the receptive segment of the postsynaptic neuron. Neurotransmitters are synthesized by neurons and are stored in vesicles, which are typically located in the presynaptic terminal. The amount of released transmitter is determined by the number and frequency of the action potentials at the presynaptic terminals. After a neurotransmitter is released from the presynaptic neuron, it diffuses across the synaptic cleft to receptors in the membrane of the postsynaptic neuron. Receptor activation results in either the opening or the closing of ion channels in the membrane of the post-synaptic cell, which alters its membrane permeability causing the cell to produce its own action potential, thereby transmitting the electrical impulse [96]. Synapses transmit signals between neurons in a constantly changing manner. The effect of a synaptic signal transmitted from one neuron to another can vary greatly depending on the recent history of activity at either or both sides of the synapse. The ensemble of mechanisms that cause activity-dependent changes in synaptic transmission is collectively known as "synaptic plasticity".

1.3.2 Synaptic plasticity

One of the most fascinating properties of the brain, known as plasticity, is the ability of neural activity produced by experience to modify neural circuit function and thus impact on subsequent thoughts, feelings, and behaviour. It is well known that synaptic plasticity, which refers to the activity-dependent modification of the strength or efficacy of synaptic transmission at pre-existing synapses, plays a critical role in the brain's capability to incorporate

transient experiences into persistent memory traces. Furthermore, synaptic plasticity plays an important role in the early development of neural circuitry[98]. Given the peculiar mechanism's complexity and diversity, a basic definition will be provided in this paragraph only to lay the groundwork for the terminology that will be used in the next Chapters.

Short-term, long-term, and paired-pulse plasticity are the neural processing phenomena most used as primary sources of inspiration for artificial neural network and brain-like computing implementations. Below, a brief overview of these synaptic paradigms will be provided.

Short-term synaptic plasticity can last from milliseconds to minutes. Short bursts of activity cause a transient accumulation of calcium in presynaptic nerve terminals, which causes most forms of short-term synaptic plasticity. This increase in presynaptic calcium alters the likelihood of neurotransmitter release by directly modifying the biochemical processes responsible for synaptic strength [99], thereby either reducing it, resulting in short-term synaptic depression, or enhancing it, resulting in short-term synaptic potentiation [100].

Paired-pulse plasticity occurs when two stimuli are delivered within a short interval across a synapse: the response to the second stimulus can be either enhanced or suppressed in comparison to the response to the first [101,102]. Paired-pulse depression is commonly observed at short (less than 20 ms) inter-stimulus intervals (ISI), and is most likely caused by voltage-dependent sodium or calcium channels inactivation [99]. At longer ISIs (20-500 ms), many synapses exhibit paired-pulse facilitation. A simple explanation for this phenomenon is that residual calcium from the invasion of the first action potential contributes to additional release during the second stimulation, nonetheless additional more sophisticated mechanisms are likely to be involved [98]. The recent history of activation of the synapse determines whether it exhibits paired-pulse facilitation or depression. Since these types of plasticity are largely caused by changes in the probability (p) of transmitter release, synapses with a very high p tend to depress their

response to the second pulse, whereas those with a very low p tend to facilitate it[103].

Long-term synaptic plasticity is a fundamental property of the nervous system and is widely regarded as a primary learning and memory mechanism [97,104]. Long-term synaptic plasticity is characterized by a sustained, activity-dependent change in synaptic efficacy. Long-term plasticity can affect synaptic strength in both directions, either increasing (ltp, long-term potentiation) or decreasing (ltd, long-term depression). Synaptic strength can be altered on either side of the synapse. Postsynaptic plasticity is characterized by changes in the number or properties of postsynaptic receptors, whereas presynaptic plasticity is characterized by an increase or decrease in neurotransmitter release [104].

1.3.3 State-of-art on organic neuromorphic devices

For many years, hardware and software-based technology has been used to implement, represent, and mimic information about biological system processing aspects. Neuromorphic computing is the way of referring to this scientific field. As previously discussed, biological signals are generated and propagated through a common milieu which contributes to determining their amplitude and frequency. Silicon-based technology cannot effectively integrate this peculiarity of biological environments. Conversely, OMIEC-based devices, and EGOTs in particular, can functionally integrate liquid electrolytes and can therefore be engineered as organic neuromorphic unit, exhibiting the basic signal processing features of biological synapses and neurons. Some of the most successful applications are highlighted in this section.

Due to EGOTs capability to operate in global or shared electrolytes, Gkoupidenis and co-workers demonstrated the global control of an array of

two-terminal devices immersed in an electrolyte, where each device consists of a PEDOT:PSS channel that serves as a hard connection between an input and an output wire. They have shown that the weights of these hard connections (i.e., their resistances) are modulated globally by the voltage applied with a common gate electrode in the electrolyte and by ion concentration, emulating neural homeoplasticity phenomena. These findings show that electrolyte gating provides significant benefits for the realization of networks of neuromorphic devices of higher complexity and with minimal hardwired connectivity, demonstrating that changing the electrolytic medium enables tuning of the device performance and definition of spatial or directional dependent soft connection weights[9]. The same group demonstrated in 2019 functional connectivity in an array of organic neuromorphic devices connected through an electrolyte. Showing that the devices output is synchronized by a global oscillatory input even though individual inputs are stochastic and independent. This temporal coupling is induced at a specific phase of the global oscillation in a way that is reminiscent of phase locking of neurons to brain oscillations [105].

Pecqueur and co-workers showed that both sensing and computing can be obtained from the intrinsic properties of a transistor array. They proposed the implementation of a spatial reservoir composed by an array of PEDOT:PSS-based EGOTs, termed organic electrochemical transistors (OECTs), that exhibit a nonlinear response to the stimulus propagating in an elecgtrolyte, exploiting the OECT channel resistance variation upon a voltage applied in the electrolyte itself. They successfully discriminated dynamic patterns out of their OECT network by using a well-established neuromorphic learning algorithm. This approach could be applied to various practical cases since most biological processes (such as electrical activity in brain cells or evolution of composition in physiological medium) belongs to the class of dynamic patterns[106].

Moreover, Desbief and co-workers demonstrated de possibility to integrate biological entities with neuromorphic devices by directly coupling an

organic neuromorphic device with a network of neurons grown and differentiated in situ, showing retention and modification of the STP of their device and good proliferation of the neuron network [107]. Following the same concept, Keene and co-workers demonstrated integration between dopaminergic cells and organic neuromorphic devices to constitute a biohybrid synapse with neurotransmitter-mediated synaptic plasticity. By mimicking the dopamine recycling machinery of the synaptic cleft, they demonstrate both long-term conditioning and recovery of the synaptic weight [108].

Harikesh et al. reported the first examples of organic electrochemical neuron (OECN) with Ion-modulated spiking, based on all printed organic electrochemical transistors. By integration of OECNs with printed OECT-based artificial synapses, they demonstrated a wide range of learning behaviours, including long-term and short-term potentiation and depression. Also, they integrated OECNs with Venus Flytrap (Dionaea muscipula) to induce lobe closure upon input stimuli, demonstrating a neuro-synaptic system with much fewer elements in comparison to Si-based circuits. Their neuron can be fully printed on flexible substrates and operates at a much lower power compared to OFET-based circuits[8]. The same group in 2023 reported a biorealistic conductance-based organic electrochemical neuron (c-OECN) using a mixed ion–electron conducting ladder-type polymer with stable ion-tunable antiambipolarity, which is used to emulate the activation/inactivation of sodium channels and delayed activation of potassium channels of biological neurons. These c-OECNs can spike at bioplausible frequencies near 100 Hz, can emulate most critical biological neural features, exhibit stochastic spiking and enable neurotransmitter-/amino acid-/ion-based spiking modulation, which is then used to stimulate biological nerves in vivo [109].

Giordani et al. demonstrated the ultrasensitive and selective detection of dopamine by means of a neuroinspired device platform without the need of a specific recognition moiety. The sensor is a whole organic device

featuring two electrodes made of PEDOT:PSS patterned on a polydimethylsiloxane (PDMS)flexible substrate. Mimicking presynaptic neuron behaviour by pulsing one electrode, the other is used to record the displacement current, mimicking the postsynaptic neuron. They demonstrated that current response exhibits the features of synaptic Short-Term Plasticity (STP) with facilitating or depressing response according to the stimulus frequency, and that the device response characteristic time depends on dopamine (DA) concentration in solution, reaching a sensitivity at the lowest concentrations below 1 nM [12]. The same group in 2020 demonstrated that, exploiting the same device architecture, the dynamic measurement of the STP transient current enabled discrimination of DA with respect to other chemical species that are produced from DA metabolic and catabolic pathways [13].

In 2022, Sarkar and co-workers reported an organic artificial neuron that is based on a compact nonlinear electrochemical element. The artificial neuron can operate in a liquid and is sensitive to the concentration of biological species (such as dopamine or ions) in its surroundings. Moreover, the system features in situ operation and spiking behaviour in biologically relevant environments — including typical physiological and pathological concentration ranges (5 – 150 mM) — and ion specificity[11]. Organic neuromorphic device development is progressing toward ever-lower-power-consuming and bio-integrable technology, paving the way for more sophisticated sensory and processing systems to be built. More about Organic transistors and their neuromorphic behaviour will be investigated in Chapter 2 and 5.

1.4 Translational organic neuroelectronics

1.4.1 Extracellular field

Electric current contributions from all active cellular processes within a volume of brain tissue superimpose and generate a potential, V_e, with respect to a reference potential. A V_e vs time trace is referred to as the electroencephalogram (EEG) when recorded from the scalp, as the electrocorticogram (ECoG) when recorded by subdural grid electrodes on the cortical surface, and as the local field potential (LFP; also known as micro-, depth or intracranial EEG) when recorded by a small-size electrode in the brain.

The extracellular field is influenced by any excitable membrane, whether it is a spine, dendrite, soma, axon, or axon terminal, as well as any type of transmembrane current. All ionic processes, from fast action potentials to the slowest fluctuations in glia activity, are superimposed in the field. Thus, regardless of its origin, any transmembrane current causes an intracellular as well as an extracellular (that is, LFP) voltage. The amplitude and frequency of the LFP waveform are determined by the proportional contribution of the multiple sources and by the chemo-physical and structural properties of the brain tissue. For instance, the greater the distance between the recording electrode and the current source, the less informative the measured LFP becomes about the events occurring at the source location. This is primarily because the amplitude of the V_e signal scales with the inverse of the distance, r, between the source and the recording site [15].

In addition to the magnitude and sign of the individual current sources, and their spatial density, the temporal coordination of the various current sources (that is, their synchrony) shapes the extracellular field.

Thus, extracellular currents can emerge from multiple sources as synaptic activity[110], calcium spikes[111], and from neuronal geometry and architecture [112].

1.4.2 State of art of PEDOT-based neural interfaces for recording

As previously mentioned, the deterioration of recording/stimulation performance over time is a major issue when interfacing brain tissue by means of invasive neural interfaces. This deterioration is mainly due to the occurrence of the foreign body reaction (FBR)[113,114], eventually leading to the encapsulation of the device by an insulating layer primarily composed of activated glia and astrocyte cells. The formation of the so-called "glial scar," combined with a concurrent reduction of the number of neurons in the probe's vicinity (within a radius of 100 m) [113], due to cell death or migration, depletes the amplitude of the recorded signals in a matter of weeks [44,115].

Aside from biotic factors, abiotic mechanisms can also impair recording quality. These abiotic mechanisms are typically referred to as "lack of structural biocompatibility." They include cyclic stresses applied to brain tissue as a result of shear micro-motion at the interface between the device or the (stiff) connector and the (soft) brain tissue, as a result of brain pulsations and micro-movements, the device's inability to conform to the cortex surface (particularly for epicortical or subdural arrays), and delamination or chemical leaching from the electrode surface, particularly when coatings are used [61,116].

To reduce the biotic and abiotic phenomena which impair interface quality, thus maintaining stable, high-quality chronic recording and stimulation, technological advances are focusing on the development of highly-flexible compliant devices. Such solutions are envisioned to reduce the invasiveness of the probe implantation [51], and to minimize the mechanical mismatch at the nervous tissue/neural device interface[75]. In this section, a brief summary of the latest results in this research field is reported.

In 2011, Khodagholy and co-workers reported highly conformable μ-ECoG arrays with PEDOT:PSS-coated Au microelectrodes [117]. PEDOT:PSS coated microelectrodes outperformed Au microelectrodes in the recording of bicucculine-triggered sharp-wave events due to their intrinsic lower

impedance. Surprisingly, the recording quality of PEDOT:PSS-coated electrodes was comparable to that of standard intracortical silicon probes with Ir microelectrodes. The same research group developed the "Neurogrid", a flexible high-density array of neuron-sized PEDOT:PSS coated microelectrodes, a few years later [85]. In freely moving rats, Neurogrid enabled mapping of action potentials from the surface of the cortex or the hippocampus, as well as detection of LFPs and action potential waveforms of individual neurons (spikes) from the cortical surface of human subjects undergoing neurosurgery for the treatment of epilepsy [118]. In their work, they highlight how array conformability to the brain's surface is a necessary prerequisite for obtaining a stable and high-quality recording. In 2022, Khodagholy's group upgraded Neurogrid by incorporating features for probe placement, long-term stability, and creating a miniaturized, biocompatible, and serializable hard-to-soft electronics interface using high resolution anisotropic mixed conducting particulate composites (MCPs), to decrease physical footprint and permit signal acquisition during minimally invasive neurosurgical procedures. They also developed a packaging system that allows touch-free array evaluation via impedance spectroscopy to improve procedure fidelity. To investigate the quality of data acquired by these devices, they recorded LFP and neural spiking data from human subjects undergoing implantation of electrodes for clinical deep brain stimulation. Spikes detected from the cortical surface by these MCP-based NeuroGrids were amenable to clustering into single units, determining design parameters for interface optimization.

These findings have shown that non-penetrating surface arrays are able to transduce single-unit activity with high-throuput and high-quality from the human brain. Such probes permit advanced interrogation of neural network operations and can be designed to be compatible with a variety of clinically relevant neurosurgical procedures, that could be useful settings to study human physiology and pathology[119].

Vomero and co-workers investigated the relationship between polyimide μ-ECoG conformability, rat cortex depression after implantation, andimpedance and recording quality in a chronic scenario. Highly flexible multi-species array, MuSA, implants of varying thickness (4 μm, 8 μm, 12 μm) and conformability were designed and manufactured, with 10 μm and 100 μm diameter microelectrodes of various materials (Pt, IrOx, and PEDOT:PSS) . Despite showing similar values in the first few weeks after implantation, the impedance of poorly conformable arrays began to significantly increase starting from the third week. Histological analysis revealed that brain depression caused by highly conformable (i.e., thin, and fenestrated) arrays was significantly smaller than that caused by poorly conformable arrays. In their study, structural biocompatibility was demonstrated to impact more than electrode material on the quality of the recording [51], meaning that both aspects shall be tackled together when designing neural probes.

Donahue and colleagues recorded neural signals and two-photon calcium imaging from the same location in the cortex of epileptic rats making advantage of the low impedance of multi-arrays of PEDOT:PSS electrodes and of the optical transparency of a thin parylene substrate[120]. High correlation between the local variations of fluorescence, due to fluctuations of intracellular calcium concentrations, and the local electrophysiological activity (i.e., LFPs) was demonstrated.

Besides electrode technology, electrolyte-gated organic transistors can provide valid alternatives or powerful supporting tools for neuroelectronics. Khodagholy and colleagues reported in 2013 the ability of OECT arrays to record neural signals with high SNR[31]. The key idea underlying the use of OECTs instead of electrodes is the super-linear amplification of LFPs into variations of the channel current[121]. Highly conformable sub-cortical arrays of PEDOT:PSS-based OECTs, implanted in the somatosensory cortex of epileptic rat models, detected both bicuculline-induced and spontaneous spikes with higher SNR than PEDOT:PSS sub-cortical electrodes and Ir intracortical microelectrodes [31]. Ultra-flexible and transparent arrays of

PEDOT:PSS based OECTs were also developed for high-resolution mapping μECoG signals evoked by blue laser light stimulation targeted on the rat's brain surface through a fibre-guided system[122].

Although electrode's technology is predominant in neurophysiology, CP-based organic transistors are likely the most reliable approach to make the leap toward high SNR recording in vivo, due to their inherent in situ signal amplification. Since they are active devices, novel propositions addressing the safety "in operando" were found to effectively overcome issues concerning the applications of additional voltages to the brain surface[72]. All these aspects will be investigated in Chapter 2 and Chapter 6.

BIBLIOGRAPHY

1. Lamprecht, R. & LeDoux, J. Structural plasticity and memory. *Nat. Rev. Neurosci.* **5**, 45–54 (2004).

2. Hu, M. *et al.* Memristor-Based Analog Computation and Neural Network Classification with a Dot Product Engine. *Adv. Mater.* **30**, 1705914 (2018).

3. Keene, S. T., Gkoupidenis, P. & Burgt, Y. van de. Neuromorphic computing systems based on flexible organic electronics. in *Organic Flexible Electronics* 531–574 (Elsevier, 2021). doi:10.1016/B978-0-12-818890-3.00018-7.

4. Chang, T., Jo, S.-H. & Lu, W. Short-Term Memory to Long-Term Memory Transition in a Nanoscale Memristor. *ACS Nano* **5**, 7669–7676 (2011).

5. Wang, Z. *et al.* Memristors with diffusive dynamics as synaptic emulators for neuromorphic computing. *Nat. Mater.* **16**, 101–108 (2017).

6. van de Burgt, Y. *et al.* A non-volatile organic electrochemical device as a low-voltage artificial synapse for neuromorphic computing. *Nat. Mater.* **16**, 414–418 (2017).

7. Di Lauro, M. *et al.* Tunable Short-Term Plasticity Response in Three-Terminal Organic Neuromorphic Devices. *ACS Appl. Electron. Mater.* **2**, 1849–1854 (2020).

8. Harikesh, P. C. *et al.* Organic electrochemical neurons and synapses with ion mediated spiking. *Nat. Commun.* **13**, 901 (2022).

9. Gkoupidenis, P., Koutsouras, D. A. & Malliaras, G. G. Neuromorphic device architectures with global connectivity through electrolyte gating. *Nat. Commun.* **8**, 15448 (2017).

10. Gkoupidenis, P., Koutsouras, D. A., Lonjaret, T., Fairfield, J. A. & Malliaras, G. G. Orientation selectivity in a multi-gated organic electrochemical transistor. *Sci. Rep.* **6**, (2016).

11. Sarkar, T. *et al.* An organic artificial spiking neuron for in situ neuromorphic sensing and biointerfacing. *Nat. Electron.* **5**, 774–783 (2022).

12. Giordani, M. *et al.* Specific Dopamine Sensing Based on Short-Term Plasticity Behavior of a Whole Organic Artificial Synapse. *ACS Sens.* **2**, 1756–1760 (2017).

13. Giordani, M. *et al.* Neuromorphic Organic Devices that Specifically Discriminate Dopamine from Its Metabolites by Nonspecific Interactions. *Adv. Funct. Mater.* **30**, (2020).

14. Gkoupidenis, P., Schaefer, N., Garlan, B. & Malliaras, G. G. Neuromorphic Functions in PEDOT:PSS Organic Electrochemical Transistors. *Adv. Mater.* **27**, 7176–7180 (2015).

15. Buzsáki, G., Anastassiou, C. A. & Koch, C. The origin of extracellular fields and currents-EEG, ECoG, LFP and spikes. *Nat. Rev. Neurosci.* **13**, 407–420 (2012).

16. Haydon, P. G. Glia: listening and talking to the synapse. *Nat. Rev. Neurosci.* **2**, 185–193 (2001).

17. Barres, B. A. The Mystery and Magic of Glia: A Perspective on Their Roles in Health and Disease. *Neuron* **60**, 430–440 (2008).

18. Miller, J. F. *et al.* Neural Activity in Human Hippocampal Formation Reveals the Spatial Context of Retrieved Memories. *Science* **342**, 1111–1114 (2013).

19. Thakor, N. V. Translating the Brain-Machine Interface. *Sci. Transl. Med.* **5**, (2013).

20. Rembado, I. *et al.* Independent Component Decomposition of Human Somatosensory Evoked Potentials Recorded by Micro-Electrocorticography. *Int. J. Neural Syst.* **27**, 1650052 (2017).

21. Nicolelis, M. A. L. & Lebedev, M. A. Principles of neural ensemble physiology underlying the operation of brain–machine interfaces. *Nat. Rev. Neurosci.* **10**, 530–540 (2009).

22. Cogan, S. F. Neural stimulation and recording electrodes. *Annu. Rev. Biomed. Eng.* **10**, 275–309 (2008).

23. Skousen, J. L. *et al.* Reducing surface area while maintaining implant penetrating profile lowers the brain foreign body response to chronically implanted planar silicon microelectrode arrays. *Progress in Brain Research* vol. 194 167–180 (2011).

24. Cruz, M. F. P. *et al.* Can Crosstalk Compromise the Recording of High-Frequency Neural Signals? in *2019 9th International IEEE/EMBS Conference on Neural Engineering (NER)* 924–927 (2019). doi:10.1109/NER.2019.8717009.

25. Koch, J., Schuettler, M., Pasluosta, C. & Stieglitz, T. Electrical connectors for neural implants: design, state of the art and future challenges of an underestimated component. *J. Neural Eng.* **16**, 061002 (2019).

26. Vomero, M. *et al.* Achieving Ultra-Conformability With Polyimide-Based ECoG Arrays. in *2018 40th Annual International Conference of the IEEE Engineering in Medicine and Biology Society (EMBC)* vols 2018-July 4464–4467 (IEEE, 2018).

27. Zhao, Z., Gong, R., Zheng, L. & Wang, J. In Vivo Neural Recording and Electrochemical Performance of Microelectrode Arrays Modified by Rough-Surfaced AuPt Alloy Nanoparticles with Nanoporosity. *Sensors* **16**, 1851 (2016).

28. Even-Chen, N. *et al.* Power-saving design opportunities for wireless intracortical brain–computer interfaces. *Nat. Biomed. Eng.* **4**, 984–996 (2020).

29. Neto, J. P. *et al.* Does Impedance Matter When Recording Spikes With Polytrodes? *Front. Neurosci.* **12**, 715 (2018).

30. Bianchi, M. *et al.* Poly(3,4-ethylenedioxythiophene)-Based Neural Interfaces for Recording and Stimulation: Fundamental Aspects and In Vivo Applications. *Adv. Sci.* **9**, 2104701 (2022).

31. Khodagholy, D. *et al.* In vivo recordings of brain activity using organic transistors. *Nat. Commun.* **4**, 1575 (2013).

32. Yuste, R. From the neuron doctrine to neural networks. *Nat. Rev. Neurosci.* **16**, 487–497 (2015).

33. Delfino, E. *et al.* Prediction of Speech Onset by Micro-Electrocorticography of the Human Brain. *Int. J. Neural Syst.* **31**, 2150025 (2021).

34. Zhang, Q. *et al.* A prototype closed-loop brain–machine interface for the study and treatment of pain. *Nat. Biomed. Eng.* (2021) doi:10.1038/s41551-021-00736-7.

35. Simon, D. T., Gabrielsson, E. O., Tybrandt, K. & Berggren, M. Organic Bioelectronics: Bridging the Signaling Gap between Biology and Technology. *Chem. Rev.* **116**, 13009–13041 (2016).

36. Larsson, K. C., Kjäll, P. & Richter-Dahlfors, A. Organic bioelectronics for electronic-to-chemical translation in modulation of neuronal signaling and machine-to-brain interfacing. *Biochim. Biophys. Acta BBA - Gen. Subj.* **1830**, 4334–4344 (2013).

37. Pais-Vieira, M. *et al.* A Closed Loop Brain-machine Interface for Epilepsy Control Using Dorsal Column Electrical Stimulation. *Sci. Rep.* **6**, 32814 (2016).

38. Fang, J. Y. & Tolleson, C. The role of deep brain stimulation in Parkinson’s disease: an overview and update on new developments. *Neuropsychiatr. Dis. Treat.* **Volume 13**, 723–732 (2017).

39. Limousin, P. & Foltynie, T. Long-term outcomes of deep brain stimulation in Parkinson disease. *Nat. Rev. Neurol.* **15**, 234–242 (2019).

40. Hochberg, L. R. *et al.* Neuronal ensemble control of prosthetic devices by a human with tetraplegia. *Nature* **442**, 164–171 (2006).

41. Carmena, J. M. *et al.* Learning to Control a Brain–Machine Interface for Reaching and Grasping by Primates. *PLoS Biol.* **1**, e42 (2003).

42. Collinger, J. L. *et al.* High-performance neuroprosthetic control by an individual with tetraplegia. *The Lancet* **381**, 557–564 (2013).

43. Fernández, E. *et al.* Acute human brain responses to intracortical microelectrode arrays: Challenges and future prospects. *Front. Neuroengineering* **7**, (2014).

44. Jorfi, M., Skousen, J. L., Weder, C. & Capadona, J. R. Progress towards biocompatible intracortical microelectrodes for neural interfacing applications. *J. Neural Eng.* **12**, 011001 (2015).

45. Carnicer-Lombarte, A., Chen, S.-T., Malliaras, G. G. & Barone, D. G. Foreign Body Reaction to Implanted Biomaterials and Its Impact in Nerve Neuroprosthetics. *Front. Bioeng. Biotechnol.* **9**, 622524 (2021).

46. Carnicer-Lombarte,Alejandro, Chen,Shao-Tuan, Velasco-Bosom,Santiago, Malliaras,George G. & Barone,Damiano G. Biocompatibility and the Biotic/Abiotic Interface-An overview of the Challenges Presented When Interfacing Electronics with Biology and Strategies to Minimize Foreign Body Response. in *Introduction to Bioelectronics: Materials, Devices, and Applications* 2-6,chapter 2 ([AIP Publishing (online), Melville, New York, 2022]Eleni Stavrinidou and Christopher M. Proctor).

47. Scholten, K. & Meng, E. Materials for microfabricated implantable devices: a review. *Lab. Chip* **15**, 4256–4272 (2015).

48. Salatino, J. W., Ludwig, K. A., Kozai, T. D. Y. & Purcell, E. K. Glial responses to implanted electrodes in the brain. *Nat. Biomed. Eng.* **1**, 862–877 (2017).

49. Moshayedi, P. *et al.* The relationship between glial cell mechanosensitivity and foreign body reactions in the central nervous system. *Biomaterials* **35**, 3919–3925 (2014).

50. Vomero, M. *et al.* Flexible Bioelectronics: Flexible Bioelectronic Devices Based on Micropatterned Monolithic Carbon Fiber Mats (Adv. Mater. Technol. 2/2020). *Adv. Mater. Technol.* **5**, 2070009 (2020).

51. Vomero, M. *et al.* Conformable polyimide-based µECoGs: Bringing the electrodes closer to the signal source. *Biomaterials* **255**, 120178 (2020).

52. Khodagholy, D. *et al.* NeuroGrid: recording action potentials from the surface of the brain. *Nat. Neurosci.* **18**, 310–315 (2015).

53. Boehler, C., Carli, S., Fadiga, L., Stieglitz, T. & Asplund, M. Tutorial: guidelines for standardized performance tests for electrodes intended for neural interfaces and bioelectronics. *Nat. Protoc.* **15**, 3557–3578 (2020).

54. Prominski,Aleksander & Tian,Bozhi. Electrodes and Materials. in *Introduction to Bioelectronics: Materials, Devices, and Applications* 10, chapter 3 ([AIP Publishing (online), Melville, New York, 2022]Eleni Stavrinidou and Christopher M. Proctor).

55. Dickson R. Yao & Dion Khodagholy. Translational Neuroelectronics. in *ntroduction to Bioelectronics: Materials, Devices, and Applications* 7, chapter 7 ([AIP Publishing (online), Melville, New York, 2022]Eleni Stavrinidou and Christopher M. Proctor).

56. Jesudason, C. Broad Considerations Concerning Electrochemical Electrodes in Primarily Fluid Environments. *Int. J. Mol. Sci.* **10**, 2203–2251 (2009).

57. Woeppel, K., Yang, Q. & Cui, X. T. Recent advances in neural electrode–tissue interfaces. *Curr. Opin. Biomed. Eng.* **4**, 21–31 (2017).

58. Carli, S. *et al.* Single walled carbon nanohorns composite for neural sensing and stimulation. *Sens. Actuators B Chem.* **271**, 280–288 (2018).

59. Boehler, C., Stieglitz, T. & Asplund, M. Nanostructured platinum grass enables superior impedance reduction for neural microelectrodes. *Biomaterials* **67**, 346–353 (2015).

60. Boehler, C., Oberueber, F., Schlabach, S., Stieglitz, T. & Asplund, M. Long-Term Stable Adhesion for Conducting Polymers in Biomedical Applications: IrOx and Nanostructured Platinum Solve the Chronic Challenge. *ACS Appl. Mater. Interfaces* **9**, 189–197 (2017).

61. Wellman, S. M. *et al.* A Materials Roadmap to Functional Neural Interface Design. *Adv. Funct. Mater.* **28**, 1701269 (2018).

62. Szostak, K. M., Grand, L. & Constandinou, T. G. Neural Interfaces for Intracortical Recording: Requirements, Fabrication Methods, and Characteristics. *Front. Neurosci.* **11**, 665 (2017).

63. Shi, Y., Peng, L., Ding, Y., Zhao, Y. & Yu, G. Nanostructured conductive polymers for advanced energy storage. *Chem. Soc. Rev.* **44**, 6684–6696 (2015).

64. Schoetz, T. *et al.* Aluminium-poly(3,4-ethylenedioxythiophene) rechargeable battery with ionic liquid electrolyte. *J. Energy Storage* (2020) doi:10.1016/j.est.2019.101176.

65. Nguyen, D. N. & Yoon, H. Recent Advances in Nanostructured Conducting Polymers: from Synthesis to Practical Applications. *Polymers* **8**, 118 (2016).

66. Savva, A. *et al.* Balancing Ionic and Electronic Conduction for High-Performance Organic Electrochemical Transistors. *Adv. Funct. Mater.* **30**, (2020).

67. Yadav, P. & Patra, A. Recent advances in poly(3,4-ethylenedioxyselenophene) and related polymers. *Polym. Chem.* **11**, 7275–7292 (2020).

68. Tomczykowa, M. & Plonska-Brzezinska, M. Conducting Polymers, Hydrogels and Their Composites: Preparation, Properties and Bioapplications. *Polymers* **11**, 350 (2019).

69. Mantione, D., del Agua, I., Sanchez-Sanchez, A. & Mecerreyes, D. Poly(3,4-ethylenedioxythiophene) (PEDOT) derivatives: Innovative conductive polymers for bioelectronics. *Polymers* **9**, (2017).

70. Venkatraman, S. *et al.* In vitro and in vivo evaluation of PEDOT microelectrodes for neural stimulation and recording. *IEEE Trans. Neural Syst. Rehabil. Eng.* **19**, 307–316 (2011).

71. Obien, M. E. J., Deligkaris, K., Bullmann, T., Bakkum, D. J. & Frey, U. Revealing neuronal function through microelectrode array recordings. *Front. Neurosci.* **9**, 423 (2015).

72. Di Lauro, M. *et al.* A Novel Biasing Scheme of Electrolyte-Gated Organic Transistors for Safe In Vivo Amplification of Electrophysiological Signals. *Adv. Mater. Interfaces* **9**, 2101798 (2022).

73. Rivnay, J. *et al.* Structural control of mixed ionic and electronic transport in conducting polymers. *Nat. Commun.* **7**, (2016).

74. Paulsen, B. D., Tybrandt, K., Stavrinidou, E. & Rivnay, J. Organic mixed ionic–electronic conductors. *Nat. Mater.* **19**, 13–26 (2020).

75. Green, R. A. *et al.* Substrate dependent stability of conducting polymer coatings on medical electrodes. *Biomaterials* **33**, 5875–5886 (2012).

76. Cui, X. & Martin, D. C. Fuzzy gold electrodes for lowering impedance and improving adhesion with electrodeposited conducting polymer ®lms. (2003).

77. Boehler, C., Vieira, D. M., Egert, U. & Asplund, M. NanoPt-A Nanostructured Electrode Coating for Neural Recording and Microstimulation. *ACS Appl. Mater. Interfaces* **12**, 14855–14865 (2020).

78. Proctor, C. M. *et al.* An Electrocorticography Device with an Integrated Microfluidic Ion Pump for Simultaneous Neural Recording and Electrophoretic Drug Delivery In Vivo. *Adv. Biosyst.* **3**, 1800270 (2019).

79. Williamson, A. *et al.* Controlling epileptiform activity with organic electronic ion pumps. *Adv. Mater. Deerfield Beach Fla* **27**, 3138–3144 (2015).

80. Han, H. *et al.* Tunable Synaptic Plasticity in Crystallized Conjugated Polymer Nanowire Artificial Synapses. (2020) doi:10.1002/aisy.201900176.

81. Kim, Y. H. *et al.* Highly conductive PEDOT:PSS electrode with optimized solvent and thermal post-treatment for ITO-free organic solar cells. *Adv. Funct. Mater.* **21**, 1076–1081 (2011).

82. Di Lauro, M. *et al.* Exploiting interfacial phenomena in organic bioelectronics: Conformable devices for bidirectional communication with living systems. *Colloids Surf. B Biointerfaces* **168**, 143–147 (2018).

83. Volkov, A. V. *et al.* Understanding the Capacitance of PEDOT:PSS. *Adv. Funct. Mater.* **27**, 1–10 (2017).

84. Koutsouras, D. A. *et al.* Impedance Spectroscopy of Spin-Cast and Electrochemically Deposited PEDOT:PSS Films on Microfabricated Electrodes with Various Areas. *ChemElectroChem* **4**, 2321–2327 (2017).

85. Rivnay, J. *et al.* High-performance transistors for bioelectronics through tuning of channel thickness. *Sci. Adv.* **1**, e1400251 (2015).

86. Sanchez-Sanchez, A., del Agua, I., Malliaras, G. G. & Mecerreyes, D. Conductive Poly(3,4-Ethylenedioxythiophene) (PEDOT)-Based Polymers and Their Applications in Bioelectronics. in *Smart Polymers and their Applications* 191–218 (Elsevier, 2019). doi:10.1016/B978-0-08-102416-4.00006-5.

87. Lipomi, D. J. *et al.* Electronic Properties of Transparent Conductive Films of PEDOT:PSS on Stretchable Substrates. *Chem. Mater.* **24**, 373–382 (2012).

88. Jonas, F. & Morrison, J. T. 3,4-polyethylenedioxythiophene (PEDT): Conductive coatings technical applications and properties. *Synth. Met.* **85**, 1397–1398 (1997).

89. Cea, C. *et al.* Enhancement-mode ion-based transistor as a comprehensive interface and real-time processing unit for in vivo electrophysiology. *Nat. Mater.* **19**, 679–686 (2020).

90. Spyropoulos, G. D. *et al.* Organic and perovskite solar modules innovated by adhesive top electrode and depth-resolved laser patterning. *Energy Environ. Sci.* **9**, 2302–2313 (2016).

91. Kim, W. H. *et al.* Molecular organic light-emitting diodes using highly conducting polymers as anodes. *Appl. Phys. Lett.* **80**, 3844–3846 (2002).

92. Kim, N. *et al.* Highly Conductive PEDOT:PSS Nanofibrils Induced by Solution-Processed Crystallization. *Adv. Mater.* **26**, 2268–2272 (2014).

93. Jönsson, S. K. M. *et al.* The effects of solvents on the morphology and sheet resistance in poly(3,4-ethylenedioxythiophene)-polystyrenesulfonic acid (PEDOT-PSS) films. *Synth. Met.* **139**, 1–10 (2003).

94. Lee, S. H. *et al.* Modified physico-chemical properties and supercapacitive performance via DMSO inducement to PEDOT:PSS active layer. *Org. Electron.* **15**, 3423–3430 (2014).

95. Marquez, A. V., McEvoy, N. & Pakdel, A. Organic Electrochemical Transistors (OECTs) Toward Flexible and Wearable Bioelectronics. *Molecules* **25**, 5288 (2020).

96. Noback, C. R. *The human nervous system: structure and function*. (Humana Press, 2005).

97. Koester, J. & Siegelbaum, S. A. Propagated Signaling: The Action Potential.

98. Citri, A. & Malenka, R. C. Synaptic Plasticity: Multiple Forms, Functions, and Mechanisms. *Neuropsychopharmacology* **33**, 18–41 (2008).

99. Mongillo, G., Barak, O. & Tsodyks, M. Synaptic Theory of Working Memory. *Science* **319**, 1543–1546 (2008).

100. Tsodyks, M. V. & Markram, H. The neural code between neocortical pyramidal neurons depends on neurotransmitter release probability. *Proc. Natl. Acad. Sci.* **94**, 719–723 (1997).

101. Katz, B. & Miledi, R. The role of calcium in neuromuscular facilitation. *J. Physiol.* **195**, 481–492 (1968).

102. Zucker, R. S. & Regehr, W. G. Short-Term Synaptic Plasticity. *Annu. Rev. Physiol.* **64**, 355–405 (2002).

103. Dobrunz, L. E. & Stevens, C. F. Heterogeneity of Release Probability, Facilitation, and Depletion at Central Synapses. *Neuron* **18**, 995–1008 (1997).

104. Yang, Y. & Calakos, N. Presynaptic long-term plasticity. *Front. Synaptic Neurosci.* **5**, (2013).

105. Koutsouras, D. A., Prodromakis, T., Malliaras, G. G., Blom, P. W. M. & Gkoupidenis, P. Functional Connectivity of Organic Neuromorphic Devices by Global Voltage Oscillations. *Adv. Intell. Syst.* **1**, 1900013 (2019).

106. Sébastien Pecqueur, *et al.* Neuromorphic Time-Dependent Pattern Classification with Organic Electrochemical Transistor Arrays.

107. Desbief, S. *et al.* Electrolyte-gated organic synapse transistor interfaced with neurons. *Org. Electron.* **38**, 21–28 (2016).

108. Keene, S. T. *et al.* A biohybrid synapse with neurotransmitter-mediated plasticity. *Nat. Mater.* **19**, 969–973 (2020).

109. Harikesh, P. C. *et al.* Ion-tunable antiambipolarity in mixed ion–electron conducting polymers enables biorealistic organic electrochemical neurons. *Nat. Mater.* (2023) doi:10.1038/s41563-022-01450-8.

110. Trevelyan, A. J. The Direct Relationship between Inhibitory Currents and Local Field Potentials. *J. Neurosci.* **29**, 15299–15307 (2009).

111. Schiller, J., Schiller, Y., Stuart, G. & Sakmann, B. Calcium action potentials restricted to distal apical dendrites of rat neocortical pyramidal neurons. *J. Physiol.* **505**, 605–616 (1997).

112. Buzsáki, G. *et al.* Hippocampal network patterns of activity in the mouse. *Neuroscience* **116**, 201–211 (2003).

113. Biran, R., Martin, D. C. & Tresco, P. A. Neuronal cell loss accompanies the brain tissue response to chronically implanted silicon microelectrode arrays. *Exp. Neurol.* **195**, 115–126 (2005).

114. Bjornsson, C. S. *et al.* Effects of insertion conditions on tissue strain and vascular damage during neuroprosthetic device insertion. *J. Neural Eng.* **3**, 196–207 (2006).

115. Massey, T., Kuo, L., Fan, J. L. & Maharbiz, M. An actuated neural probe architecture for reducing gliosis-induced recording degradation. *bioRxiv* 380006 (2018) doi:10.1101/380006.

116. Seymour, J. P., Wu, F., Wise, K. D. & Yoon, E. State-of-the-art mems and microsystem tools for brain research. *Microsystems and Nanoengineering* vol. 3 (2017).

117. Khodagholy, D. *et al.* High speed and high density organic electrochemical transistor arrays. *Appl. Phys. Lett.* **99**, (2011).

118. Khodagholy, D. *et al.* Organic electronics for high-resolution electrocorticography of the human brain. *Sci. Adv.* **2**, e1601027 (2016).

119. Hassan, A. R. *et al.* Translational Organic Neural Interface Devices at Single Neuron Resolution. *Adv. Sci.* **9**, 2202306 (2022).

120. Donahue, M. J. *et al.* High-Performance Vertical Organic Electrochemical Transistors. *Adv. Mater.* **30**, 1–5 (2018).

121. Cramer, T. *et al.* Organic ultra-thin film transistors with a liquid gate for extracellular stimulation and recording of electric activity of stem cell-derived neuronal networks. *Phys. Chem. Chem. Phys.* **15**, 3897–3905 (2013).

122. Lee, W. *et al.* Transparent, conformable, active multielectrode array using organic electrochemical transistors. *Proc. Natl. Acad. Sci. U. S. A.* **114**, 10554–10559 (2017).

Chapter 2: Electrolyte-gated organic transistors

The theoretical and operational aspects of Electrolyte-Gated Organic Transistors are highlighted in this Chapter, beginning with a brief introduction to mathematical models for steady-state and transient behaviour, device characterization strategies, and the possibility of varying electrical properties by adjusting geometrical parameters. Finally, the neuromorphic behaviour and transduction mechanism are discussed.

The transistor, a semiconductor device that controls channel current using gate voltage, is the core element of contemporary electronics. John Bardeen, Walter Brattain, and William Shockley, three American physicists, developed it in 1947, winning the Nobel Prize in 1956 [1]. Starting from their seminal discoveries, transistor technology has nowadays branched to include an incredibly vast variety of architectures. Among these, the most relevant for organic electronics is the metal-oxide-semiconductor field-effect transistor (MOSFET), here considered as paradigmatic inorganic counterpart. Indeed, with minimal modification of the MOSFET architecture, it has been possible to develop the workhorse devices of organic electronics, namely organic field-effect transistor (OFET) and, upon a further developmental step, electrolyte-gated organic transistors (EGOT). **Figure 4** shows the analogies between top-gate bottom-contact MOSFET/OFET and EGOT.

Metal contacts, oxide insulator, and semiconducting channel are the three constitutional units that make up a MOSFET. Gate (G), drain (D), and source (S) are the electrode terminals that enable MOSFET driving and addressing. MOSFETs can be either n-type (with electrons acting as carriers) or p-type (with holes acting as carriers) depending on the characteristics of the semiconducting channel.

By applying a gate-source voltage, V_{GS}, the oxide insulator acts as a capacitor and causes charge accumulation in the semiconducting channel close to the semiconductor/insulator interface. These collected carriers can be moved from source to drain by applying an additional voltage between the drain and source, V_{DS}, which yields the drain-source current, I_{DS}. This type of transistor is known as a field-effect transistor because the applied electric field on the gate terminal modulates the charge carrier concentration and channel current [2].

By replacing the inorganic semiconductor with an organic one, the OFET is obtained. Compared with MOSFETs, OFETs can be fabricated at much lower temperature, which enable their application on flexible substrates [3]. By

substituting the oxide insulator with an electrolyte that is directly interfaced with the organic semiconductor is possible to obtain an EGOT device, which feature ultra-low operational voltages ($|V_{GS}| < 1V$) if compared to OFET ($20V < |V_{GS}| < 40V$). This dramatic performance improvement is due to the fact that the capacitance of the electrical double layer at the gate/electrolyte interface, responsible of charge (i.e., ions) accumulation near the channel in EGOTs($\approx 10^{-4}$-10^{-5} F cm^{-2}), is orders of magnitude higher than the one of silicon oxide commonly used as gate dielectric in OFETs ($\approx 10^{-8}$-10^{-9} F cm^{-2}).

As a direct consequence of their operational principle, EGOTs strongly rely on ion transport. It is not surprising hence, that organic mixed ionic-electronic (semi-)conductors are the materials of choice for EGOT fabrication. EGOTs are commonly referred to as electrolyte-gated organic field-effect transistors (EGOFETs), putting emphasis on the role of the electric field in the electrolyte in determining the channel conductance, or as OECTs, putting emphasis on the electro-chemical nature of the channel conductance modulation [4–6]. Both the terminologies can be regarded as correct, and or not the only ones used in the literature to describe such architectures, nonetheless in this thesis they will be collectively referred to as EGOTs.
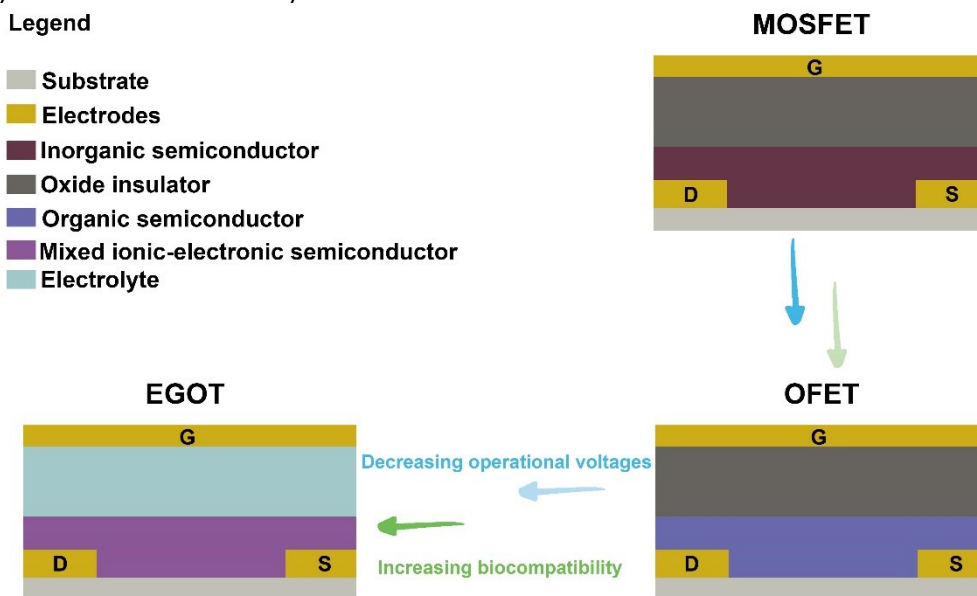
Figure 4. Conceptual transition from MOSFET to EGOT, by replacing the inorganic semiconductor and the oxide insulator with an organic semiconductor and an electrolyte, respectively, resulting in lower power consumption and improved biocompatibility.

2. Electrolyte-Gated Organic Transistors

Electrolyte-gated organic transistors are thin-film transistor that have shown great compliance to a wide range of applications including bio-sensing[7], logic circuits[8], signal transduction[9,10] and neuromorphic electronics [11,12]. EGOTs are mostly operated in the standard common-source/common-ground (CSCG) configuration, **Figure 5**. Briefly, the S electrode is grounded and connected with the D by means of a (semi-)conductive polymer film, which forms the 'channel'. The two driving voltages, V_{DS} and V_{GS}, are applied, with respect to the S, at the D and at the G, respectively. A current, I_{DS}, flows in the channel in response to V_{DS}. Magnitude of this current depends on the resistance of the channel which is a function of the ion concentration in close proximity to the channel. By arbitrarily modulating V_{GS} it is possible to set the electrochemical potential of the electrolyte, which governs the ionic density at the channel/electrolyte interface and, ultimately, the channel resistance. The dependence of I_{DS} on V_{GS} is called transconductance (g_m) and represents the ability of the device to amplify a voltage change at the gate electrode into a current variation in the channel [13]. N- or p-type organic semiconductors can be used in organic transistors, which can also operate in depletion or accumulation modes. In the first scenario, the transistor is in its ON-state in the absence of gate bias and V_{GS} is required to deplete the channel of charge carriers and switch the transistor to its OFF-state. In accumulation-mode EGOTs, the transistor is in its OFF-state in the absence of gating, and a gate bias is required to build up charge in the channel and turn the device ON.

PEDOT:PSS is used as the active material in all the device architectures described in this thesis. PEDOT:PSS-based EGOTs are depletion-mode devices. For increasingly positive values of V_{GS}, cations coming from the electrolyte are pushed towards the conductive film, compensating the charges of the SO_3^- ions (sulfonate ions) in the PSS chains. Sulfonate ions are responsible of coordinating holes in PEDOT:PSS and of enabling their transport(see section 1.1). As a consequence, cation coordination by

sulfonate residues causes drastic decrease in hole mobility, thus making the PEDOT:PSS polymer less conductive. This process is commonly referred to as "de-doping" or "depletion".

Device design routes to modulate EGOT performances involve multiple aspects, ranging from variation of the electrolyte concentration, modification of the device geometry (i.e., the ratio of channel width to channel length) and/or of the electrolyte/channel interface extension by acting on the polymeric film thickness [14,15].

Several models [5,16–22] have been implemented starting from the Bernards and Malliaras model describing electronic charge transport in EGOT channel with the same set of equation, Equation 1 and Equation 2, used to describe MOSFET with long channel. This is done by adding a thickness term in the geometric W/L factor of the Drude's model for MOSFETs and replacing the internal capacitance with an empirical parameter having the physical dimensions of a capacitance per unit volume, termed volumetric capacitance C*, to highlight that the physical thickness of the semiconductor channel importantly influence EGOT performances[23].

$$I_{DS} = \mu C^* \frac{Wd}{L}\left(V_{GS}-V_P-\frac{1}{2}V_{DS}\right)V_{DS} \quad \text{Linear region} \tag{1}$$

$$I_{DS} = \mu C^* \frac{Wd}{2L}(V_{GS}-V_P)^2 \qquad \text{Saturation region} \tag{2}$$

W and L are respectively the width and the length of the channel, V_P is the pinch-off, defined as the gate voltage at which the depletion region closes the channel and μ is the hole mobility. μC^*, measured in S V^{-1} cm^{-1}, is a hybrid parameter which accounts for describe mixed ionic- electronic semiconductors properties, defining a differential transconductance per unit thickness.

By deriving the I_{DS} current with respect to the gate voltage is possible to obtain analytical expressions for the transconductance, Equation 3 and Equation 4, describing how much an EGOT can amplify a voltage signal at the gate electrode.

$$g_m = -\mu C^* \frac{Wd}{L} V_{DS} \qquad \text{Linear region} \qquad (3)$$

$$g_m = \mu C^* \frac{Wd}{L} (V_{GS} - V_P) \qquad \text{Saturation region} \qquad (4)$$

Friedlein and co-workers expanded and integrated this model with the electrolyte capacitance intended as an equivalent capacitance made of two capacitors in series, one at the gate/electrolyte interface and one at the electrolyte/channel interface, showing that, the transconductance is proportional to the product of μ for the equivalent capacitance and the device response speed is inversely proportional to the product of the solution resistance for the equivalent capacitance [5,17]. Furthermore, they incorporated ionic mobility to the model, making it more dynamic than the prior model.
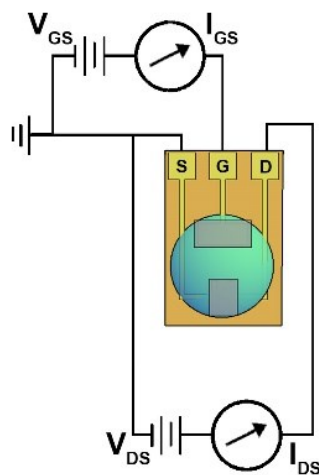
Figure 5. An electrolyte-gated organic transistor with a common source/common ground configuration. The drain-source voltage, V_{DS}, and the gate-source voltage, V_{GS}, are both applied. The drain-source current, I_{DS}, also known as the channel current, and the gate-source current, I_{GS}, are both collected.

Interestingly, analogous models have been proposed for other non PEDOT:PSS-based EGOT architectures. In particular, the sensing behaviour of pentacene EGOTs can be rationalized in terms of ratios between the two areal capacitances at the gate/electrolyte and electrolyte/channel interfaces [24,25].

This brief overview of the mathematical models used to describe the operation of EGOTs, which solely scratches the surface of an consistent literary production [26–30], shows how device performance is determined by parameters that can be designed a priori to maximize transconductance. Despite this, the interaction between active material and electrolyte, especially concerning transient responses, is difficult to be modelled unambiguously. As a result, whenever a novel device is designed and defined with new geometrical parameters or new materials, it becomes, in most situations, a case study per se. However, all the proposed models provide the scientific community with handy, although always partially imprecise, tools for juggling the improvement of these devices.

2.1 Tuning device electrical performances

Besides the possibility to tune device performances by just varying operational parameters acting on the doping/de-doping states of the device, or by varying the organic semiconductors exploited as active layer[31], it is possible modify device features through design parameters such as aspect ratio and channel thickness or varying the electrolyte chemistry [32–34]. This dependency on chemo-physical parameters of the electrolyte makes EGOTs the most investigated sensor architectures in organic electronics. EGOT-based Dopamine sensors[35,36], pH sensors[25], ion sensors[32], and transducers of biological signals in vivo and in vitro[9,37] have been

demonstrated, making advantage of prompt customizability in terms of size, design and surface chemical functionality.

Since transconductance is the key trait of these devices, designers often strive to maximize it, and numerous studies have tackled the influence of geometrical features on channel current [13,14,38]. As expected from equations 3 and 4, Rivnay and colleagues experimentally demonstrated a linear dependency of transconductance on channel width-to-length ratio(W/L) at constant thickness.

Besides the magnitude of the transconductance, also the gate voltage for which it exhibits a maximum, $V_{G(gm, max)}$, was shown to depend on W / L and on channel thickness. In particular, changing the aspect ratio while maintaining the channel thickness resulted in a greater maximum transconductance, albeit shifted at larger gate bias. However, in full accordance with the second Ohhm's law, both $g_{m, max}$ and $V_{G (gm, max)}$ increase by increasing channel film thickness [14,38]. In a nutshell, wider and thicker channels need more ions to be de-doped (greater $V_{G (gm, max)}$) and, in the same V_{GS} span, yield greater modulation upon de-doping with respect to narrower and thinner channels.

Liang and co-workers, however, demonstrated intrinsical limits to the strategy of increasing transconductance by increasing W/L, with a siystematic study on interdigitate S and D electrodes. Terming L_{ch} the channel length and W_f the width of electrodes fingers they have shown that, while the increase in the number of electrode fingers corresponds to an increase of W/L_{ch} ratios which causes improved device performances, the simultaneous increase of W_f and L_{ch} leads to a maximization of g_{max}, although the W/L_{ch} ratio decreases. The origin of this deviation from classical behaviour lies in the opposite effects of W_f and L_{ch} on the electrical performance of interdigitated EGOTs. L_{ch} directly determines the channel resistance R_{ch}, while W_f strongly affects the source–drain series resistance R_{sd}. The influence of W_f on maximum I_{DS} and g_{max} is stronger than that of L_{ch} since R_{sd} (elsewhere termed contact resistance) is limiting the performance of interdigitated EGOTs when

L_{ch} is lower than 15 μm. For longer channels, R_{ch} becomes dominant and the characteristics of interdigitated EGOTs converge toward those of linear EGOTs. They derived several design rules to tailor the performances of interdigitated EGOTs, suggesting a large number of electrode fingers as well as long and broad fingers to obtain large g_{max}, while keeping the channel length as short as possible to facilitate short response times[39].

Also, Tyrrell and colleagues presented a systematic investigation on interdigitation as a way to tune device performances, confirming the key role of thickness to achieve high transconductance. Furthermore, they showed that transistor miniaturization brings a parasitic capacitance into play that affects the device time response. With short channel lengths and high drain voltages they observed that the device response time was limited by the ion transport time, which is dependent on the electrolyte resistance and the capacitance of the system. As a result, it can be predicted that the response time dependence on channel dimensions scales as $\tau \sim d(WL)^{1/2}$. They showed also that this parasitic capacitive contribution significantly increased the response time of the larger interdigitated patterns such that their capability to measure high-frequency bioelectric events was greatly reduced.[40].

These examples demonstrate how even minor geometric alterations result in dramatic alteration of the so-called gain/transconductance trade-off. Thus, the channel's length and width, the active material's thickness, and the change in the electrolyte are only a few factors that intersect and interact to define each unique device, which must be designed and characterized individually in accordance with the peculiar needs of the intended application.

2.2 Characterization of transistors

To evaluate the electrical properties of transistors, standard electrical testing procedures must be used. The various testing protocols concurring to a full device characterization can be divided into two macro-categories: steady-state (i.e., direct current, DC) and transient (i.e., alternating current, AC) techniques. The former require the acquisition of the standard current-voltage (I-V) characteristics, while the latter include pulse response, bandwidth characterization, and electrochemical impedance spectroscopy for the assessment of gate and channel capacitance. The following discussion will cover some of the AC and DC characterization techniques routinely performed on EGOT devices.

2.2.1 DC characterization

Standard EGOT electrical characterization measurements are performed in common source/common ground configuration, as depicted in **Figure 5**. I-V characteristics are well known as output and transfer curves, according to which driving voltage is swept, and are the most common and informative tools to evaluate the device quasi-static behaviour and its amplification capability, as well as intrinsic properties of the channel.

Transfer characteristics show I_{DS} as a function of V_{GS}, at a fixed V_{DS} value. A negative V_{DS} is often used in transistors based on p-type semiconductors, whereas V_{GS} is linearly swept. The magnitude of V_{DS} and V_{GS} can vary depending on the nature of the dielectric layer and of the channel. Since EGOTs operate in aqueous environment, V_{GS} lower than ±1V can avoid electrolysis, which is critical for direct operation in biological environment. A typical transfer curve is shown in **Figure 6 a**. Transfers are multiparametric characteristics which enable direct extraction of a variety of information, such as the ON current (i.e., current at maximum doping level), the OFF

current (i.e., current at minimum doping level), their ratio, which accounts for the device amplification capability, and the possible hysteresis between forward and backward scans, which accounts for kinetic unbalance between doping and de-doping processes. Furthermore, the correlation between transconductance, **Figure 6 b**, and V_{GS} can be determined by a first order differentiation of I_{DS} with respect to V_{GS}. To maximize biological signal amplification performances in bioelectronic applications, the g_m vs V_{GS} profile is critical for choosing operational gate voltage in continuous device operation.
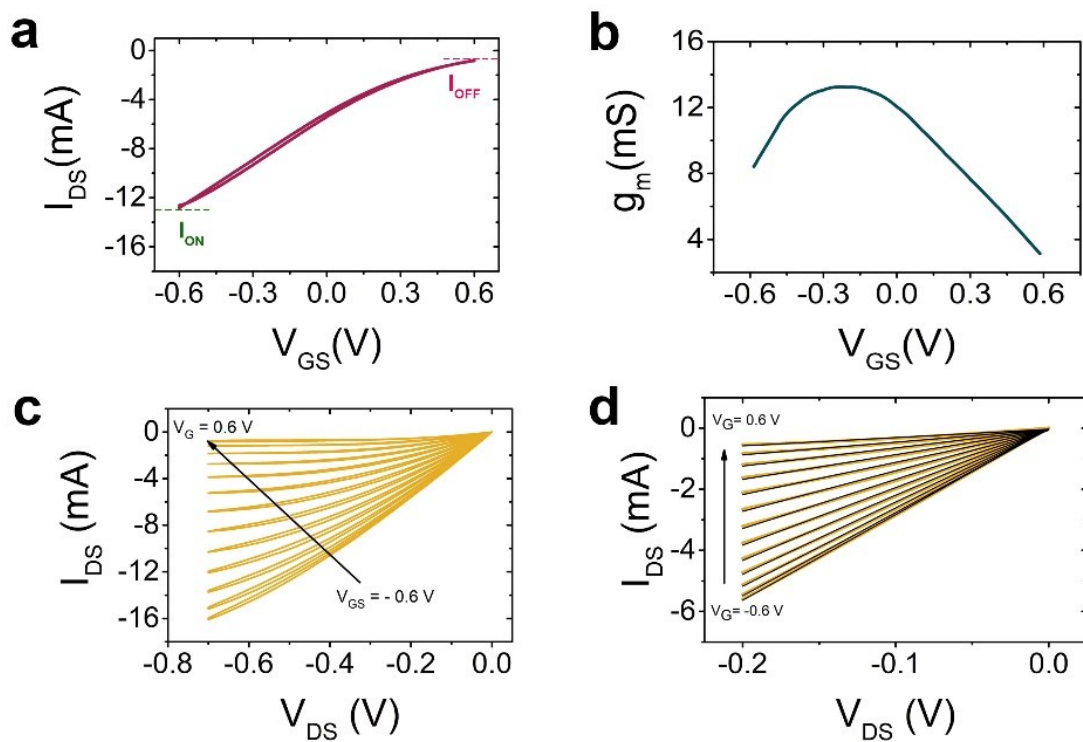
Figure 6. EGOT's current-voltage (I-V) characteristics: a) transfer characteristic, highlighting the ON and OFF state, b) transconductance vs V_{GS} trend, c) output characteristic at various V_{GS}, c) Extrapolation and superimposed linear fit of the forward scan output curve's linear region.

Besides the transfer curve, the output characteristic, **Figure 6 c**, is another important tool that can be used to describe transistor's operation. At fixed individual values of V_{GS}, the output curve correlates I_{DS} with V_{DS}. Referring our discussion to a p-type transistor, the output acquisition protocol requires a linear scan of V_{DS} between 0 V and at least -1 V for each value of applied V_{GS}. The I_{DS} current behaves differently for each V_{GS} applied and held

constant during the acquisition of each output curve. For increasingly positive V_{GS} values, I_{DS} approaches zero. As V_{GS} increases, the decrease in current is related with the decrease in charge carriers available in the conductive polymer film.

Output curves provide a wealth of information as well. They can be used to estimate the ON current for each pair of V_{GS} and V_{DS} applied. Furthermore in a small V_{DS} interval close to 0 V, **Figure 6 d**, the channel behaves as a purely ohmic conductor. By performing linear fits in this region, it is possible to extrapolate the channel conductance values (G=1/R) at each V_{GS} and to rule out any considerable effect of the contact resistance between the electrodes and the semi-conductive channel, indicating that the charge injection interface is effective and the passage of charge from the active layer to the electrode is not hampered. If this was not the case, we would see an inflection of the I_{DS} versus V_{DS} curve near these potential values [41].

2.2.2 AC characterization

When EGOTs are intended to be used as transducer of biological signals, it becomes of utmost importance to evaluate their temporal response, i.e., device characteristic time and bandwidth, since the signal source (ideally, the brain) contains information over a wide frequency window [39,42,43]. The time response evaluation is usually carried out by electrochemical impedance spectroscopy (EIS) measurement or by tracking the transient behaviour by application of square voltage pulses at different frequencies [2].

Usually, EIS measurements are performed in a two-terminal layout, using short circuited drain and source contacts bridged by the organic (semi-)conductor film as working electrode and a counter electrode of the same material as the gate electrode [14]. This approach, despite providing useful insights regarding the doping/de-doping processes occurring at the interface between organic semiconductor and electrolyte, fails in describing

the AC behaviour of the charge transport across the channel (i.e., the impedance between source and drain). To obtain information about charge transport across the channel, other protocols for EIS measurement can be envisioned, which require the application of a constant potential to the gate while the drain electrode acts as working electrodes, and the source acts as common ground and counter electrode[11]. In this configuration, the influence of V_{GS} on the frequency response of the channel current can be observed.

Transient behaviour measurements foresee the application of a square wave pulsed voltage to the gate, recording the I_{DS} current flowing in the channel, at fixed value of V_{DS} [44–47]. By fitting the I_{DS} vs time profile with an exponential fit is possible to extrapolate the characteristic time of the transient behaviour [2]. However, it is possible to analyse the transistor transient behaviour by using a square pulsed voltage as V_{DS} and a fixed V_{GS}, while recording I_{DS}. Since V_{GS} controls the electrochemical potential of the electrolyte, governing the ionic density at the channel/electrolyte interface, it is possible to extract the characteristic timescale related to the channel de-doping level from each transient behaviour by fitting the obtained I_{DS} curve with a stretched exponential model [11].

Aside from pulse response, bandwidth evaluation is crucial for EGOT translation in biological contexts. For the bandwidth evaluation, sinusoidal wave voltages are injected at the gate electrode, fixing a V_{DS}, and the output I_{DS} current is collected. Extrapolating the I_{DS} sine wave amplitude for each frequency (usually between 1 Hz and 1000Hz) the current versus frequency response is obtained. Computing, at each frequency, the amplitude ratio between I_{DS} and V_{GS}, the relationship between transconductance and frequency can be obtained, determining the transistor bandwidth profile [39].

2.3 Neuromorphic behaviour

Among dynamic EGOT applications, it is worth highlighting their employment as neuromorphic devices. In general, the capability of organic neuromorphic devices to emulate signal processing features of biological synapses stems from OMIECs intrinsic properties. OMIECs' time response is dictated by the dynamic interplay between ions (slow carriers) and electrons(fast carriers) as well as by the features of the input signals [18]. Several organic synaptic mechanisms have been reported when an electrical pulse is applied to a presynaptic electrode, inducing changes in the conductivity of the organic active layer and resulting in postsynaptic responses, such as STP or LTP behaviour [35,44,45,48], synaptic weight emulation [11,49] and paired-pulse plasticity [50]. All these features can be obtained with two- terminal or three terminal organic devices. However, the physical chemistry beyond these phenomena is still under investigation.

A useful model for neuromorphism in two-terminal PEDOT/PSS-based architectures was given by Calandra and co-workers, who showed that systematic variation of the presynaptic input frequency unveils a crossover from depressive (at high frequency input voltage pulses) to facilitative (at lower frequency input voltage pulses) STP responses. They proposed an equivalent circuit model by adding a pseudo-inductive component in parallel with the conventional RC circuit used for purely depressive STP. The introduction of a frequency-dependent inductive contribution explains the transition between and the coexistence of both depressive and facilitating behaviours and forecast device response as a function of the frequency used as a presynaptic trigger and of electrolyte parameters. STP at a specific frequency can be either depressive, facilitative, or a coexistence of the two regimes. The input frequency allows the operator to select which of the three regimes (steady-state current, depressive or facilitative current) shall be dominant, and the number of input voltage pulses dictates the sampling of only depressive, only facilitating, or both STP-responses [51].

As discussed, when it comes to three-terminal devices, lots of models describing transient response have been developed. In the simplest ones, which decompose the EGOT into an electrical and an ionic circuit, the transient response can be characterized primarily by two parameters: the electronic transit time and the characteristic time constant for ionic transport in the electrolyte. Their contribution is weighted by an empirical proportional constant f that accounts for the spatial non-uniformity of the de-doping process; it is dependent on both the applied voltages, V_D and V_G, and incorporates much of the temporal response's complexity [23].

In further developments, it has been proposed that the f factor should be considered constant and equal to 0.5. This means that, upon a gate voltage square pulse, the source and drain contributions to the channel current do not have equal amplitudes and defining a limit case: if the change in the channel current is exactly equal to half of the maximum gate current, the transient profile will not show observable exponential relaxation[5,17].

Tu et al. adopted the Ward-Dutton partition scheme to define f. In this scheme, one integrates over the mobile charge in the channel and assumes that a fraction x/L of the mobile charge at position x along the channel (L channel length) contributes to the current in the drain while the remaining fraction, (1- x/L), accounts from the current from the source. Under this assumption, one obtains a voltage-dependent value of f. Tu et al. show that this partitioning scheme leads to an analytical expression for both the drain and source current transients, and they show that their model qualitatively agrees with experimental data[18].

Paudel and co-workers proposed an even more complex model by modelling ionic currents, perpendicular and lateral to the channel, by a 2D drift-diffusion model showing that the transient response is marked by two distinct time constants, a short time constant describing the movement of ions perpendicular to the transistor channel and a second, longer one describing the lateral flow of ions currents along the channel to reach the equilibrium of the device. Measurements of the transient response of EGOTs

faster than the lateral time constant leads to a frequency, geometry, and drain potential dependent response, complicating the interpretation of transient EGOT measurements[22].

Thanks to the level of complexity required for modelling such an intertwined scientific problem, this is a fertile area for scientific investigation and discovery, with each model adding more information to the physics of EGOTs. Materials, electrolytes, device geometric factors, and operational conditions are only a few of the elements that interact to define the time constant and hence the transient response of EGOTs, and developing a consistent all-encompassing model remains still an open challenge.

2.4 Signal transduction in transistors-based technology

Recording, transduction, and processing of brain activity for the understanding of human disease, or its prevention, treatment or monitoring are still widely investigated in vision to develop more performing brain-interfaces suitable for this purposes [52]. Intra- or epi-cortical electrode devices are frequently employed for recording and monitoring brain bioelectronic activity[53–56]. Nonetheless, to achieve a high spatiotemporal resolution, downsizing is required, even though it leads to increased impedance and noise enhancement[57,58]. To address these issues, organic semiconductor technology has proven to be the most successful platform in neurophysiological applications [59].

Furthermore, new technologies can be used as novel read out strategies for brain signals to overcome the natural rise in noise caused by miniaturisation. Transistor-based architectures which provide in situ amplification of ECoG and μ-ECoG signals represent a promising new alternative [9,37,42]. When electrodes are used for in vivo recording, an ex-situ amplification is required, which also involves the line noise amplification. Downstream amplification thus results in increased line noise which affects the SNR. Instead, when

transistors are used, an in-situ amplification of the neurophysiological signal and biological noise is carried out. Line noise is not enhanced in this case but is just transmitted as it is, **Figure 7**. As a result, the SNR increases.

Importantly, it is worth noticing that this approach is pursued also by standard electrode-based systems for electrophysiology, which tend to bring the electronics for signal amplification and digitalization as close as possible to the biological signal source[60].

PEDOT:PSS EGOTs were used to transduce epileptiform activity in rats, providing increased SNR with respect to conventional surface microelectrodes[61,62], demonstrating the eligibility of EGOT technology for translation to neural recording application [63]. Despite these promising results, the use of EGOTs for electrophysiological applications is still limited by two factors: i) EGOTs are operated in the common-source/common-ground configuration, which implies the application of a bias in the brain; ii) EGOT working principle implies that higher amplification gain results in decreased bandwidth, and vice versa[14]. If the former issue can be circumvented by careful device design in order to achieve maximum gain at zero bias [64] or by implementing alternative connection schemes[37], the latter is ubiquitous in EGOTs and hard to avoid with materials currently in use. As aforementioned, these devices can also mimic the response of neuronal synapses, embodying some of the functions of neural circuitry in a single device, such as short-term plasticity, spike-timing-dependent plasticity, long-term potentiation, and long-term depression[11,36,65].

These properties are attractive for developing artificial synapses in neuromorphic circuits on the one hand, and prosthetic integration into the brain circuitry on the other hand[66]. Therefore, EGOT-based arrays could be designed with a variety of functionalities, allowing for the creation of adaptive multimodal neural interfaces capable of on-site amplification, signal analysis (including data filtering, pattern recognition, and artifact detection), drug release, and sensing of molecules/proteins of interest.
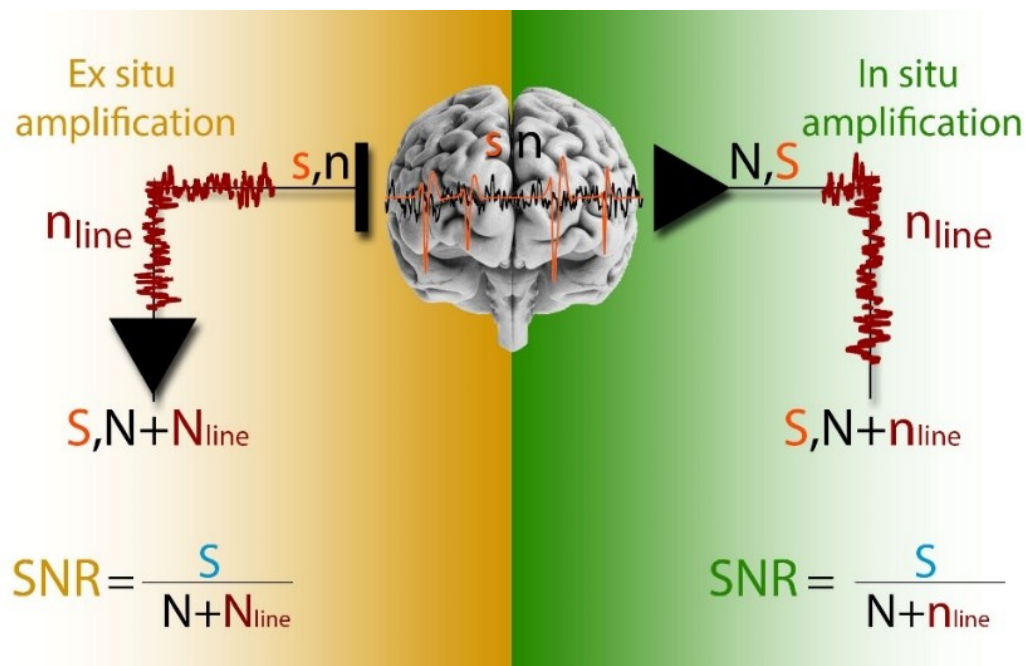
Figure 7. Why should an organic transistor be used for brain recording? In situ versus ex situ amplification by means of transistor-based neural interfaces. n is the biological noise, s is the neurophysiological signal, n-line is the line noise. Capital letters indicate the corresponding amplified signals. Reprinted with permission [55]. Copyright 2022, Advanced Science published by Wiley-VCH GmbH.

BIBLIOGRAPHY

1. Brinkman, W. F., Haggan, D. E. & Troutman, W. W. A history of the invention of the transistor and where it will lead us. *IEEE J. Solid-State Circuits* **32**, 1858–1865 (1997).

2. Xudong Ji & Jonathan Rivnay. Transistors in Bioelectronics. in *Introduction to Bioelectronics: Materials, Devices, and Applications* 1-4,Chapter 4 (edited by Eleni Stavrinidou and Christopher M. Proctor [AIP Publishing (online), Melville, New York, 2022]).

3. Peng, B. *et al.* High performance organic transistor active-matrix driver developed on paper substrate. *Sci. Rep.* **4**, 6430 (2014).

4. Rivnay, J. *et al.* Organic electrochemical transistors. *Nat. Rev. Mater.* **3**, 17086 (2018).

5. Friedlein, J. T., McLeod, R. R. & Rivnay, J. Device physics of organic electrochemical transistors. *Org. Electron.* **63**, 398–414 (2018).

6. Kergoat, L., Piro, B., Berggren, M., Horowitz, G. & Pham, M. C. Advances in organic transistor-based biosensors: From organic electrochemical transistors to electrolyte-gated organic field-effect transistors. *Anal. Bioanal. Chem.* **402**, 1813–1826 (2012).

7. Macchia, E. *et al.* About the amplification factors in organic bioelectronic sensors. *Mater. Horiz.* **7**, 999–1013 (2020).

8. Perez, J. C. & Shaheen, S. E. Neuromorphic-based Boolean and reversible logic circuits from organic electrochemical transistors. *MRS Bull.* **45**, 649–654 (2020).

9. Khodagholy, D. *et al.* Organic electronics for high-resolution electrocorticography of the human brain. *Sci. Adv.* **2**, e1601027 (2016).

10. Di Lauro, M. *et al.* A novel biasing scheme of Electrolyte-Gated Organic Transistors for safe in situ amplification of electrophysiological signals. *Adv. Mater. Interfaces - Rev.*

11. Di Lauro, M. *et al.* Tunable Short-Term Plasticity Response in Three-Terminal Organic Neuromorphic Devices. *ACS Appl. Electron. Mater.* **2**, 1849–1854 (2020).

12. Gkoupidenis, P., Koutsouras, D. A. & Malliaras, G. G. Neuromorphic device architectures with global connectivity through electrolyte gating. *Nat. Commun.* **8**, (2017).

13. Paudel, P. R., Kaphle, V., Dahal, D., Radha Krishnan, R. K. & Lüssem, B. Tuning the Transconductance of Organic Electrochemical Transistors. *Adv. Funct. Mater.* **31**, 1–12 (2021).

14. Rivnay, J. *et al.* High-performance transistors for bioelectronics through tuning of channel thickness. *Sci. Adv.* **1**, e1400251 (2015).

15. Cicoira, F. *et al.* Influence of device geometry on sensor characteristics of planar Organic electrochemical transistors. *Adv. Mater.* **22**, 1012–1016 (2010).

16. Tarabella, G. *et al.* Effect of the gate electrode on the response of organic electrochemical transistors. *Appl. Phys. Lett.* **97**, 123304 (2010).

17. Friedlein, J. T. *et al.* Influence of disorder on transfer characteristics of organic electrochemical transistors. *Appl. Phys. Lett.* **111**, 023301 (2017).

18. Tu, D. & Fabiano, S. Mixed ion-electron transport in organic electrochemical transistors. *Appl. Phys. Lett.* **117**, 080501 (2020).

19. Shirinskaya, A., Horowitz, G., Rivnay, J., Malliaras, G. & Bonnassieux, Y. Numerical Modeling of an Organic Electrochemical Transistor. *Biosensors* **8**, 103 (2018).

20. Faria, G. C., Duong, D. T. & Salleo, A. On the transient response of organic electrochemical transistors. *Org. Electron.* **45**, 215–221 (2017).

21. Colucci, R., Barbosa, H. F. D. P., Günther, F., Cavassin, P. & Faria, G. C. Recent advances in modeling organic electrochemical transistors. *Flex. Print. Electron.* **5**, (2020).

22. Paudel, P. R., Skowrons, M., Dahal, D., Radha Krishnan, R. K. & Lüssem, B. The Transient Response of Organic Electrochemical Transistors. *Adv. Theory Simul.* **5**, 2100563 (2022).

23. Bernards, D. A. & Malliaras, G. G. Steady-state and transient behavior of organic electrochemical transistors. *Adv. Funct. Mater.* (2007) doi:10.1002/adfm.200601239.

24. Casalini, S., Leonardi, F., Cramer, T. & Biscarini, F. Organic field-effect transistor for label-free dopamine sensing. *Org. Electron.* **14**, 156–163 (2013).

25. Di Lauro, M. *et al.* The Substrate is a pH-Controlled Second Gate of Electrolyte-Gated Organic Field-Effect Transistor. *ACS Appl. Mater. Interfaces* **8**, 31783–31790 (2016).

26. Larissa Huetter, Adrica Kyndiah & Gabriel Gomila. Analytical Physical Model for Organic Metal-Electrolyte-Semiconductor Capacitors. *Advanced Theory and Simulations* **6**, (2023).

27. Nissa, J., Janson, P., Simon, D. T. & Berggren, M. Expanding the understanding of organic electrochemical transistor function. *Appl. Phys. Lett.* **118**, (2021).

28. Tu, D. *et al.* A Static Model for Electrolyte-Gated Organic Field-Effect Transistors. *IEEE Trans. Electron Devices* **58**, 3574–3582 (2011).

29. Delavari, N. *et al.* Nernst–Planck–Poisson analysis of electrolyte-gated organic field-effect transistors. *J. Phys. Appl. Phys.* **54**, 415101 (2021).

30. Natali, D., Fumagalli, L. & Sampietro, M. Modeling of organic thin film transistors: Effect of contact resistances. *J. Appl. Phys.* **101**, 014501 (2007).

31. Carli, S. *et al.* Multifunctionally-doped PEDOT for organic electrochemical transistors. *Front. Mater.* **9**, 1063763 (2022).

32. Lin, P., Yan, F. & Chan, H. L. W. Ion-Sensitive Properties of Organic Electrochemical Transistors. *ACS Appl. Mater. Interfaces* **2**, 1637–1641 (2010).

33. Savva, A. *et al.* Influence of Water on the Performance of Organic Electrochemical Transistors. *Chem. Mater.* **31**, 927–937 (2019).

34. Ghittorelli, M. *et al.* High-sensitivity ion detection at low voltages with current-driven organic electrochemical transistors. *Nat. Commun.* **9**, 1441 (2018).

35. Giordani, M. *et al.* Specific Dopamine Sensing Based on Short-Term Plasticity Behavior of a Whole Organic Artificial Synapse. *ACS Sens.* **2**, 1756–1760 (2017).

36. Giordani, M. *et al.* Neuromorphic Organic Devices that Specifically Discriminate Dopamine from Its Metabolites by Nonspecific Interactions. *Adv. Funct. Mater.* **30**, (2020).

37. Di Lauro, M. *et al.* A Novel Biasing Scheme of Electrolyte-Gated Organic Transistors for Safe In Vivo Amplification of Electrophysiological Signals. *Adv. Mater. Interfaces* **9**, 2101798 (2022).

38. Rivnay, J. *et al.* Organic Electrochemical Transistors with Maximum Transconductance at Zero Gate Bias. *Adv. Mater.* **25**, 7010–7014 (2013).

39. Liang, Y. *et al.* Tuning Channel Architecture of Interdigitated Organic Electrochemical Transistors for Recording the Action Potentials of Electrogenic Cells. *Adv. Funct. Mater.* **29**, 1902085 (2019).

40. Tyrrell, J. E., Boutelle, M. G. & Campbell, A. J. Measurement of Electrophysiological Signals In Vitro Using High-Performance Organic Electrochemical Transistors. *Adv. Funct. Mater.* **31**, 2007086 (2021).

41. Kaphle, V., Liu, S., Al-Shadeedi, A., Keum, C. M. & Lüssem, B. Contact Resistance Effects in Highly Doped Organic Electrochemical Transistors. *Adv. Mater.* **28**, 8766–8770 (2016).

42. Tyrrell, J. E., Boutelle, M. G. & Campbell, A. J. Measurement of Electrophysiological Signals In Vitro Using High-Performance Organic Electrochemical Transistors. *Adv. Funct. Mater.* **31**, 1–12 (2021).

43. Buzsáki, G., Anastassiou, C. A. & Koch, C. The origin of extracellular fields and currents-EEG, ECoG, LFP and spikes. *Nat. Rev. Neurosci.* **13**, 407–420 (2012).

44. Gkoupidenis, P., Schaefer, N., Garlan, B. & Malliaras, G. G. Neuromorphic Functions in PEDOT:PSS Organic Electrochemical Transistors. *Adv. Mater.* **27**, 7176–7180 (2015).

45. Qian, C. *et al.* Artificial Synapses Based on in-Plane Gate Organic Electrochemical Transistors. *ACS Appl. Mater. Interfaces* **8**, 26169–26175 (2016).

46. Ling, H. *et al.* Electrolyte-gated transistors for synaptic electronics, neuromorphic computing, and adaptable biointerfacing. *Appl. Phys. Rev.* **7**, 011307 (2020).

47. Hu, Y. *et al.* Diverse Synaptic Plasticity Induced by the Interplay of Ionic Polarization and Doping at Salt-Doped Electrolyte/Semiconducting Polymer Interface. *ACS Omega* **2**, 746–754 (2017).

48. Grubb, M. S. *et al.* Short- and Long-Term Plasticity at the Axon Initial Segment. *J. Neurosci.* **31**, 16049–16055 (2011).

49. Gkoupidenis, P., Koutsouras, D. A. & Malliaras, G. G. Neuromorphic device architectures with global connectivity through electrolyte gating. *Nat. Commun.* **8**, 15448 (2017).

50. Rondelli, F. *et al.* Pre-synaptic DC bias controls the plasticity and dynamics of three-terminal neuromorphic electrolyte-gated organic transistors. *Neuromorphic Comput. Eng.* (2023) doi:10.1088/2634-4386/acb37f.

51. Calandra Sebastianella, G. *et al.* Implantable Organic Artificial Synapses Exhibiting Crossover between Depressive and Facilitative Plasticity Response. *Adv. Electron. Mater.* **7**, 2100755 (2021).

52. Nicolelis, M. A. L. & Lebedev, M. A. Principles of neural ensemble physiology underlying the operation of brain–machine interfaces. *Nat. Rev. Neurosci.* **10**, 530–540 (2009).

53. Seymour, J. P., Wu, F., Wise, K. D. & Yoon, E. State-of-the-art mems and microsystem tools for brain research. *Microsystems and Nanoengineering* vol. 3 (2017).

54. Hermiz, J. *et al.* Stimulus Driven Single Unit Activity From Micro-Electrocorticography. *Frontiers in Neuroscience* vol. 14 (2020).

55. Vomero, M. *et al.* Conformable polyimide-based µECoGs: Bringing the electrodes closer to the signal source. *Biomaterials* **255**, 120178 (2020).

56. Fernández, E. *et al.* Acute human brain responses to intracortical microelectrode arrays: Challenges and future prospects. *Front. Neuroengineering* **7**, (2014).

57. Schuettler, M., Ulloa, M., Ordonez, J. S. & Stieglitz, T. Laser-fabrication of neural electrode arrays with sputtered iridium oxide film. in *2013 6th International IEEE/EMBS Conference on Neural Engineering (NER)* 1171–1173 (2013). doi:10.1109/NER.2013.6696147.

58. Zhao, Z., Gong, R., Zheng, L. & Wang, J. In Vivo Neural Recording and Electrochemical Performance of Microelectrode Arrays Modified by Rough-Surfaced AuPt Alloy Nanoparticles with Nanoporosity. *Sensors* **16**, 1851 (2016).

59. Bianchi, M. *et al.* Poly(3,4-ethylenedioxythiophene)-Based Neural Interfaces for Recording and Stimulation: Fundamental Aspects and In Vivo Applications. *Adv. Sci.* **9**, 2104701 (2022).

60. Delfino, E. *et al.* Prediction of Speech Onset by Micro-Electrocorticography of the Human Brain. *Int. J. Neural Syst.* **31**, 2150025 (2021).

61. Khodagholy, D. *et al.* In vivo recordings of brain activity using organic transistors. *Nat. Commun.* **4**, 1575 (2013).

62. Cea, C. *et al.* Enhancement-mode ion-based transistor as a comprehensive interface and real-time processing unit for in vivo electrophysiology. *Nat. Mater.* **19**, 679–686 (2020).

63. Simon, D. T., Gabrielsson, E. O., Tybrandt, K. & Berggren, M. Organic Bioelectronics: Bridging the Signaling Gap between Biology and Technology. *Chem. Rev.* **116**, 13009–13041 (2016).

64. Rivnay, J. *et al.* Organic Electrochemical Transistors with Maximum Transconductance at Zero Gate Bias. *Adv. Mater.* **25**, 7010–7014 (2013).

65. Gerasimov, J. Y. *et al.* An Evolvable Organic Electrochemical Transistor for Neuromorphic Applications. *Adv. Sci.* **6**, 1801339 (2019).

66. Harikesh, P. C. *et al.* Ion-tunable antiambipolarity in mixed ion–electron conducting polymers enables biorealistic organic electrochemical neurons. *Nat. Mater.* (2023) doi:10.1038/s41563-022-01450-8.

3. *Aim and approach*

This dissertation focuses on electrolyte-gated organic transistors and their applications in translational neuroscience. The goal of this thesis is to present a variety of possible EGOT-based architectures implemented as neuromorphic organic units, as well as recording sites for electrophysiological activities, with the purpose of improving recording and processing of complex signals, such as brain signals, envisioning EGOT-based arrays endowed with different functionalities, allowing the design of adaptive multimodal neural interfaces capable of on-site amplification, data filtering, and sorting.

To pursue this aim, three key issues must be addressed:

1) EGOTs are active devices that require two driving voltages to be operated. It is critical to implement safe strategy of biasing for EGOTs when devising their use in brain interfaces, since undesired faradic reactions may lead to critical tissue and/or device damage, as well as improving their structural biocompatibility;

2) Fundamental knowledge of the frequency response (i.e., AC response) of EGOT devices, which is the main functional feature for neuromorphism, must be extended and related to operational scenarios;

3) Typically, the transduced (and optionally amplified) biological signal is sent directly to ex-situ processing units, which are tasked with doing off-line data analysis, such as selecting pathophysiologically important spectral regions, detecting, and eliminating artifacts, and recognizing diagnostic patterns. This signal treatment is frequently performed manually by operators, and it is both time-consuming and power-

intensive, hampering the integration of closed-loop operator-independent theranostic brain machine interfaces (BMIs).

This thesis intends to provide possible solutions to these shortcomings by individually addressing them. It discusses in detail the proposition of a novel biasing scheme for EGOT-based in vivo amplifiers, targeted at avoiding the application of a bias in the brain, and presents its assessment in vitro and in vivo, with a focus on the retention of the amplification features of EGOTs.

Structural biocompatibility of EGOT-based neural interfaces is improved by developing and presenting strategies for the integration of EGOT units in state-of-the-art ultra-conformable substrates by means of standard clean room procedures. To ensure prompt translation, the workflow for the achievement of such arrays is inspired directly from that of golden standard micro-epicortical (μ-ECoG) arrays.

The advantages of a three-terminal architecture for neuromorphic devices are demonstrated, including reversible fine-tuning of the STP, single pulse, and paired-pulse plasticity responses, generating a multilevel memory operation by working on the gate potential.

Finally, an organic flexible architecture for real-time signal sorting is proposed, which is based on whole organic low- and high-pass passive filters suitable to downsizing and integration in BMIs while being specifically designed to be coupled to EGOT-based in situ amplifiers. Its signal sorting capabilities, as well as EGOT's intrinsic filtering properties, are demonstrated and benchmarked against digitally synthetized model signals of increasing complexity.

Chapter 4: Materials and methods

This section presents all the materials, the devices fabrication and characterization protocol, as well as instruments and data analysis procedures used to evaluate our devices and to validate our results.

4.1 Materials

Formulations of PEDOT:PSS for drop-casting have been achieved by adding 5% v/v dimethylsulfoxide (DMSO, Merck) and 0.2% (3-glycidyloxypropyl)trimethoxysilane (GOPS, Merck) to commercial Clevios PH1000 (Heraeus). Different dilutions of this formulation have been deposited, according to the desired application.

Sodium poly-styrene sulfonate (NaPSS, Merck) and 3,4-ethylenedioxythiophene (EDOT, Merck) are used for electrodeposition of PEDOT/PSS.

Kapton-supported gold electrodes were achieved by metallization (10nm Nickel Chromium adhesive layer, 70 nm Au, Creavac - Creative Vakuumbeschichtung GmbH) of 50µm thick Kapton (polyimide) sheets.

Test patterns for EGOT fabrication were custom-designed and purchased from Phoenix PCB.

Phosphate-buffered saline solution 1M (P36191GA, Merck) has been used as electrolyte.

Polyimide (U-Varnish-S, UBE Industries, Ltd, Japan), AZ 5214 E (Micro-Chemicals GmbH, Germany), AZ® 125 nXT (Micro-Chemicals GmbH, Germany) and Kapton tape (tesa® 51408) were used for multi-species transistor arrays fabrication.

4.2 Electrode Test Pattern

The electrode arrays used for transistor fabrication are custom designed by the Italian Institute of Technology and purchased from Phoenix PCB (https://www.phoenixpcb.it/). Arrays have a multilayer structure in which polyimide layers alternate with adhesive layers, and the center polyimide layer has copper electrodes plated in gold, **Figure 8 a**. Each matrix has nine

pairs of electrodes, each of which defines a source-drain couple; an upper polyimide layer covers the tracks and exposes just the terminal portion of the electrodes, shown in detail in **Figure 8 c** and **d**. The source-drain couples are spaced apart by 2 mm. For each individual device on the array, we have the following geometric parameters: the single device active area equals 0.72 mm^2; the width of the channel, W, is 400 μm; while the length of the
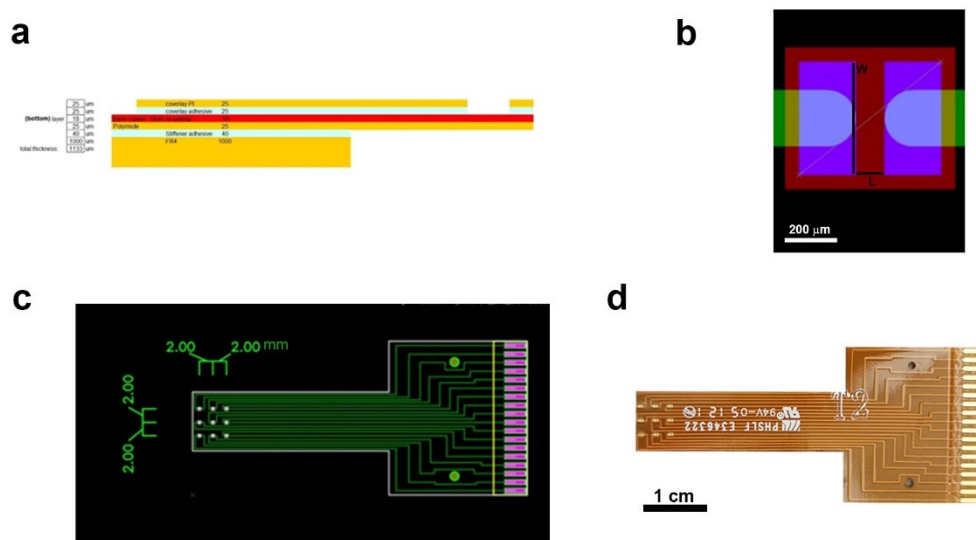
Figure 8. a) Matrix cross-section, b) Two electrodes (in purple) with W, width of the channel, and L, length of the channel (left),c) array architecture showing electrode tracks (in green) and the connection pads (in pink) (right), c) Final array picture.

channel between the two electrodes, L, is 100 μm, **Figure 8 b**. Each electrode is connected through a track (green lines) to the connectors (pink squares) at the base of the structure, **Figure 8 b**. Connections are made using a probe station equipped with three spring contact probes and micrometric screws for precise x-y-z alignment or by soldering specific connectors to the pads.

4.3 Organic passive circuit elements

To obtain resistors, the PEDOT:PSS formulation is diluted 1:2 with MilliQ H$_2$O and drop-cast between two Au electrodes of the EGOT test patterns (0.5 μL on a 0.72 mm^2 area). The average resistance is 2.9±0.2 Ω.

The fabrication of electrolyte-organic capacitors starts by covering two Au electrodes supported on Kapton (active area of each electrode = 0.3 cm^2) with PEDOT/PSS via potentiostatic electrodeposition (5s 0.2V, then 0.8V in charge limit control, up to the desired charge density) in an aqueous electrolyte containing 10 mM EDOT and 5 mg mL^{-1} NaPSS. The investigated charge densities are 83 mC cm^{-2} and 166 mC cm^{-2}, resulting in equivalent capacitance values of 220±10 μF and 295±18 μF at 100 Hz when exposed to PBS electrolyte (measured by a precision LCR bridge, Thurbly Thandar Instruments).

4.4 Electrolyte-Gated Organic Transistor fabrication

To establish EGOT channels and co-planar gate electrodes, the PEDOT:PSS formulation (section 4.1) was filtered to remove aggregates then diluted 1:10 with MilliQ water. This diluted formulation is then stirred for one minute before being dropped cast (0.5 μL on a 0.72 mm^2 area) onto the previously specified test matrix and thermally cured for 30 minutes in a thermostatic oven at 120°C. Average thickness is 1 μm, as measured by atomic-force microscopy (XE7 AFM Park System, tapping mode).

4.5 Multi-species transistor array – MuSTA

Thin-film devices were fabricated using standard microlithography techniques in the clean-room facility (ISO 5, according to ISO 14644–1) at the Department of Microsystem Engineering (IMTEK) of the University of Freiburg. The fabrication process starts with the spin-coating of polyimide (U-Varnish-S, UBE Industries, Ltd, Japan) on a bare silicon wafer at a speed of 3000 rpm to achieve the desired film thickness equals to 5 μm and curing at 450 °C. The high precision image-reversal photoresist AZ 5214 E (Micro-Chemicals GmbH, Germany) is used as sacrificial layer for the patterning of the metallization layer, which includes electrodes, tracks, and pads. An oxygen

plasma surface activation is performed (80 W, Plasma System 300-E, PVA TePla, Germany) to promote adhesion prior to the sputtering of a 100 nm-thick gold layer (Uni-vex 500 Sputter Device, Leybold GmbH, Germany). The metal is structured in a lift-off step consisting of three acetone baths and one isopropanol bath. Subsequently, the wafers are generously washed and placed on a QDR machine to rinse their surface and finally dried. After another oxygen plasma activation, a second polyimide layer is spun and cured. To pattern the openings and outlines, a thick layer of negative photoresist AZ® 125 nXT (Micro-Chemicals GmbH, Germany) is used as masking layer. The structuring is done by reactive-ion-etching (RIE) (STS Multiplex ICP, SPTS Technologies, United Kingdom) in a two-step process, the first at 200 W. In the second step, the electrodes and pads areas are covered with Kapton tape (tesa® 51408) prior to a 100 W RIE treatment. The remaining resist is then stripped in acetone.

4.6 Electrodeposition protocols

All the electrodeposition protocols are carried out with a Gamry Reference 600 in potentiostatic mode, by applying 0.2 V for 5 s, then 0.8 V in charge limit control, up to the desired charge density.

4.6.1 MuSTA electrodeposition protocols

The values of charge density, J, are estimated after evaluating the area occupied by electrodes. In terms of J, the identical technique is used for the two distinct electrode geometries. Starting with the solution presented in sections 4.3, PEDOT/PSS is electrodeposited. A pair of adjacent electrodes is short circuited and serves as the working electrode, a Pt mesh electrode serves as the counter electrode, and a calomel electrode serves as the reference electrode. Electrodeposition is carried out using J values of 400 mC cm^{-2}, 500 mC cm^{-2}, 250 mC cm^{-2}, and 200 mC cm^{-2}.

4.7 DC characterization

The electrical measurements on our devices are conducted using dual-channel Source/Measure Units (SMU) (Keysight B2912A or B2902A). Each channel allows voltage sourcing and current measurement between its two terminals (high- and low- force). To support the SMU, a Custom Designed Control Software Suite (Smucs15b) is used to control, program and display data, in real-time, during measurement acquisition. Through Smucs15b GUI, it is possible to control the applied voltages at high-force terminals and record the respective currents or to source currents and measure the respective voltage drops between high and low terminals.

I–V characteristics are acquired in common source/common ground configuration, using 1M Phosphate Buffered Saline (PBS) solution at pH=7.4 (P36191GA, Merck) as an electrolyte. I–V transfer characteristics are acquired sweeping V_{GS} from – 0.8 to 0.8V by steps of 2mV (scan rate=100mV s^{-1}), while keeping V_{DS} equals to -0.7 V. I–V output characteristics are acquired by cycling V_{DS} from 0.0V to -0.7V, changing the fixed V_{GS} value at each cycle from -0.8V to 0.8V with steps of 0.2 V.

For MuSTA, I-V characteristics have been acquired in the usual common source/common ground configuration, using 1M Phosphate Buffered Saline (PBS) solution at pH=7.4 (P36191GA, Merck) as an electrolyte. I–V transfer characteristics are acquired sweeping V_{GS} from – 0.8 to 0.8V by steps of 8mV (scan rate=200mV s^{-1}), while keeping V_{DS} equals to -0.8 V. I–V output characteristics are acquired by cycling V_{DS} from 0.0V to -0.8V, changing the fixed V_{GS} value at each cycle from -0.8V to 0.8V with steps of 0.2 V.

4.8 AC characterization

An Agilent33220A arbitrary waveform generator is used as source of model signals, for organic filters, sorting platform and EGOT bandwidth evaluation.

Source/Measure Unit (SMU) (Keysight B2912A) was exploited as source of square wave pulsed voltage for neuromorphic applications. In particular, for neuromorphic tunable behaviour the relative neuromorphic response has been obtained fixing drain potential equal to -0.3 V and 0 V and by adding to the drain electrode a square pulse train of varying frequencies and amplitude equals to -0.5 V with one channel of the SMU, using the other channel to provide a DC bias at the gate electrode from -0.6 V to 0.6 V, recording I_{DS} versus time responses. Influence of DC offset bias at the gate electrode in determining the neuromorphic response of EGOTs is investigated by varying the V_{GS} DC -offset ranging from -0.7V to 0.7V with steps of 0.2 V and adding a programming step of the AC pre-synaptic V_{GS} voltage by means of Smucs15b software, acquiring the postsynaptic current I_{DS} vs time.

Responses to single pulses are investigated by administering V_{GS} square pulses (amplitude = -0.5V, duration = 20s); paired-pulse plasticity is assessed with 2 subsequent V_{GS} square pulses (amplitude = -0.5V, duration = 10s), varying the inter-pulse interval from 20ms to 200s.

EGOT bandwidth is evaluated in common source/common ground configuration by sourcing the gate potential with sinusoidal waves with amplitude equal to 200 mV$_{pp}$ and frequency ranging from 1 Hz to 1000 Hz, recording I_{DS} values in time. For MuSTA, the bandwidth is estimated by using a bath electrode connected to the Agilent33220A arbitrary waveform generator as signal source in PBS 1M. Keeping V_{GS} = 0 V and V_{DS} = -0.7 V, the current I_{DS} and I_{GS} were measured with the Source/Measure Unit (SMU) (Keysight B2912A).

Organic filters and sorting platform frequency-dependent profiles are characterized by applying at the V_{IN} sinusoidal waves with amplitude equal to 200 mV$_{pp}$ and frequency ranging from 1 Hz to 1000 Hz, recording the voltage output and the current output with a Source/Measure Unit (SMU) (Keysight B2912A) in current mode and voltage mode, respectively. Pre-recorded somatosensory evoked potential is digitalized and stored in a

77

Agilent33220A arbitrary waveform generator. This signal and a sweep signal with frequency ranging from 1 Hz to 200 Hz are exploited as model signals to characterize the sorting platform filtering properties. Both signals are used as V_{in} with a final amplitude equal to 200 mV_{pp} and the current output is recorded with a Source/Measure Unit (SMU) (Keysight B2912A).

Three-terminal impedance spectroscopy was carried out by coupling Source/Measure Unit and Gamry reference 600 in order to collect impedance between source and drain at various fixed gate voltages. The gate electrode is connected to the high-force terminal of one of the SMU channels, with a constant bias applied, the drain electrode is connected to the working electrode terminal in the Gamry reference 600. A sinusoidal potential is applied to this electrode and impedance is recorded by measuring the current response and the phase shift between applied voltage and measured current. The source electrode acts as common ground, being connected both to the SMU's low-force terminal and to the counter electrode terminal of the Gamry reference 600. The reference electrode terminal is short-circuited with the counter electrode one, as it is commonly done for two-terminal EIS recording. The amplitude of the sinusoidal wave applied at the drain electrode (working electrode) equals 100 mV, its frequency spans five orders of magnitude ranging from 1 Hz to 100000 Hz, meanwhile the voltage applied to the gate ranging from -0.6 V to 0.2 V.

4.9 Audio track acquisition and rescaling

For audio filtering experiments with whole organic filters, audio track is acquired as voltage versus time by directly connecting the TS mini-jack output of a laptop soundboard to the input of an Agilent Technologies DSO6012A oscilloscope 100MHz 2GSa/s, sampling at 50 kHz. The collected track is reproduced using Matlab Audio Toolbox at a 25-times lower speed and used as V_{IN} for the coupled organic filters. The output voltages are

collected with a Source/Measure Unit (SMU) (Keysight B2912A) in current-control mode at a sampling frequency equal to 500Hz. The two filtered output voltages are played back at normal speed using Matlab Audio Toolbox.

4.10 *In vivo* recordings on rats

Experiments were performed in compliance with the guidelines established by the European Communities Council (Directive 2010/63/EU, Italian Legislative Decree n. 26, 4/3/2014) and the protocol was approved by the Ethics Committee for animal research of the University of Ferrara and by the Italian Ministry of Health (permission n. 989/2020-PR). EGOTs were evaluated in vivo in the primary somatosensory cortex (barrel field), S1BF, in four adult Long Evans rats (males, 400-500 g)[1]. Briefly, the animals were anesthetized with a mixture of Zoletil (Virbac, France; 30 mg kg^{-1}) and Xylazine (Bayer, Germany; 5 mg kg^{-1}) administered intraperitoneally. For the entire duration of the procedure, the depth of anaesthesia was monitored by testing the absence of hind limb withdrawal reflex and was maintained by additional intramuscular doses of aesthetic.

The anesthetized animals were then placed in a stereotaxic apparatus (David Kopf Instruments, USA) equipped with ear bars (Model 957 for small animals) and a ≈ 2 cm long incision was made along the midline of the cranium. The underlying muscle and connective tissue were pulled to expose the skull, and a craniotomy (≈ 6x6 mm^2) in the parietal bone was performed to expose the somatosensory cortex, which was identified using vascular landmarks and stereotaxic coordinates[1]. To avoid local heating and to maintain the bone surface clean, a sterile saline solution was applied while drilling.

A stainless steel bone screw was put in the contralateral parietal bone to serve as a ground/reference point as needed. Finally, each device was

epidurally put over the barrel cortex[1]. A vibrating system was employed to induce a multiwhiskers deflection along the horizontal plane in order to elicit the neuronal response of the rat barrel cortex, somatosensory evoked potential (SEP). Rat whiskers were shortened and inserted in a Velcro strip linked to a rod moved by a shaker (Bruel & Kjaer, Denmark, Type 4810 tiny shaker) controlled by a National Instruments board (Austin, USA).

The deflection stimulus, a sine waveform with a period of 12 ms and an amplitude corresponding with whisker deflection of 500 µm, was repeated 100 times. Neural data were collected at 2000 samples per second using a Keysight B2912A Source-Measure Unit in common drain/grounded source configuration. The recorded animals were housed in a Faraday cage to decrease electromagnetic noise. Maximum transconductance was achieved by applying $V_{GD} = -0.7$ V and $V_{DS} = 0.7$ V, in a common drain/grounded source configuration, resulting in net zero bias in the brain, as it will be discussed in detail in Chapter 6.

When aiming to collect somatosensory evoked responses (1 position over the cortex of Rat 1, 2 positions over the cortex of Rat 2 and 1 position over the cortex of Rat 3), 1 s trials (n = 100), triggered by the start of the whiskers stimulation, were collected. Differently, as a further assessment of the recording capability of EGOT (Rat 4), 5 s recording sessions were collected during stochastic mechanical stimulation of the rat whiskers, during spontaneous neural activity without stimulation, and after sacrificing the animals with an intracardiac injection of Tanax (0.3 mL kg^{-1}).

Voltage recordings of SEPs employing the gate EGOT terminal as a passive electrode were performed using a Tucker Davis Technologies multichannel recording system 3 (Tucker Davis Technologies, USA) including: a ZIF-Clip headstage with unity (1X) gain, a RZ2 real-time processor, and a PZ2-256 battery-powered preamplifier. Data were digitized at a sample rate of 12207 s^{-1} and transferred from the RZ2 processor to a computer by fast fiber optic connection. As required by the single-ended headstage configuration,

reference and ground pins of the headstage were tied together and connected to the skull screw.

4.11 Data analysis

Data analysis and graphing has been performed with Origin 2016 and Matlab (version 9.10, Mathworks, Natick, MA, USA) for all the experiments in this thesis. Here below are detailed all the data analysis procedures.

4.11.1 Organic filters and sorting platform

Organic filters and sorting platform frequency-dependent profiles are evaluated by extracting the voltage output and current output amplitudes, respectively and calculating the filters gain as 20 x log10 (V_{out}/V_{IN}), meanwhile the sorting platform frequency profile by extracting the peak-to-peak current output signal amplitude, dividing the latter respect the input voltage, obtaining the classical transconductance versus frequency response. To evaluate the data in the time-frequency domain, the Matlab function *spectrogram* was used, with a window length of 100 samples and a window overlap of 90%. The power percentage was calculated by filtering the data in four frequency bands with the Matlab function *designfilt*. For each filtered signal and for the broadband signal the power was estimated with Matlab function *bandpower* and the power of each band-filtered dataset was divided by its brodband signal power. Sorting factor was estimated by exploiting Matlab function *bandpower* after dividing the signals in 13 frequency band and subsequently calculating their ratio. Spectral analysis of the audio signals has been performed with Steinberg Cubase 5.0.

4.11.2 In *vivo* data analysis

Neural data analysis was carried out using Matlab (version 9.10, Mathworks, Natick, MA, USA). All the recorded signals were band-pass filtered (15–150 Hz, by the Matlab function *filtfilt*, 4th order Butterworth). Additionally, AC line noise was removed with a 50 Hz notch filter (4th order Butterworth). Voltage traces (sampling frequency = 12 207 samples s^{-1}) were undersampled at 2000 samples s^{-1} prior to filtering, for comparison purposes with the current traces. Neural activity in both time and time-frequency domains evoked by whiskers stimulation was compared to spontaneous activity in the absence of stimulation and to the noise level of the system (i.e., current acquired after sacrificing the animals). Specifically, to examine the data in the time-frequency domain, the Matlab function *spectrogram* was used setting a window length of 100 samples and 90% of window overlap. The power of the signals recorded in the three different conditions was estimated as the square of the RMS level using the Matlab function *bandpower* in the 15–150 Hz frequency range. To investigate the somatosensory evoked responses recorded with EGOTs and passive electrodes, data were segmented (500 ms window, centered on stimulus onset). The mean over trials was computed in the time domain and the average spectrogram was calculated as aforementioned (window length of 100 samples, 90% overlap). The SNR was calculated as the ratio between the power of the event (i.e., the power in the 75 ms time window after the start of the stimulation) and the power of an equally wide time window of prestimulus spontaneous activity, as previously reported for the analysis of event related potentials (ERP)[2–4]. The correlation between either I_{DS} or V_{EI} averaged over 100 randomly selected trial groups and the average over all trials was computed to determine the minimum number of trials required to obtain a robust estimate of the somatosensory evoked response. Correlation coefficients were computed using the Matlab function *corrcoef* in a time window of 75 ms after the stimulation onset. The procedure was repeated increasing group numerosity by steps of 1 until reaching the total amount of collected trials (n = 100). A

correlation of 90% was set as threshold to determine the number of trials required to obtain a reliable estimation of the somatosensory evoked response[3].

BIBLIOGRAPHY

1. George Paxinos & Charles Watson. *The Rat Brainin Stereotaxic Coordinates*. (Academic Press, 2008).

2. Vomero, M. *et al.* Highly Stable Glassy Carbon Interfaces for Long-Term Neural Stimulation and Low-Noise Recording of Brain Activity. *Sci. Rep.* **7**, 40332 (2017).

3. Cohen, M. X. Analyzing neural time series data: Theory and practice. (2014) doi:10.7551/mitpress/9609.001.0001.

4. Suarez-Perez, A. *et al.* Quantification of Signal-to-Noise Ratio in Cerebral Cortex Recordings Using Flexible MEAs With Co-localized Platinum Black, Carbon Nanotubes, and Gold Electrodes. *Front. Neurosci.* **12**, 862 (2018).

Chapter 5: Controlling neuromorphic behaviour

Two neuromorphic responses are presented using the same test pattern: short-term and paired-pulse plasticity. The ability to elicit various neuromorphic behaviour by modifying the stimulation paradigm with a single architecture is highlighted.

As already mentioned, organic neuromorphic devices are particularly successful in mimicking basic brain functionalities, such as STP or LTP, including important spiking phenomena. This combination of biocompatible hardware and biomimicking behaviour results in organic neuromorphic electonics, a novel hybrid technologic fields which concerns, on the one hand, the development of increasingly complex organic neuromorphic units and circuits and, on the other hand, their interfacing with the bio-world. Different neuromorphic features are demonstrated in this chapter using the same device architecture. The ability to adjust neuromorphic behaviour by simply changing the stimulation paradigm or other operational conditions is demonstrated as a useful route for the implementation of tunable and dynamic neuromorphic circuits.

5.1 Tunable Short-Term Plasticity Response

As discussed in Chapter 1, simulation of synaptic behaviour is of tremendous interest in a variety of fields of research. Several inorganic, organic, or hybrid electronic devices have been used for this purpose, ranging from memristive circuits [1,2], in which the resistance state of a semiconductive material (dependent on the material's past history) is used as synaptic weight in artificial neural networks, to asynchronous spiking neural networks, in which information is encoded as spiking time and frequency [3]. The organic electronics technological platform, which is based on naturally low-power devices that can be integrated over a vast area and work in a liquid environment [4–6], offers unparalleled possibilities in this regard. Organic neuromorphic devices have been successfully demonstrated for a wide spectrum of applications [7], ranging from Pavlovian learning to selective neurotransmitter sensing [8], because they can reproduce and benefit from the two main mechanisms characterizing physiological synapses, namely short-term plasticity STP and long-term potentiation LTP [9]. Furthermore, unlike their inorganic counterparts, organic neuromorphic devices can quickly

interface with living matter, particularly neuronal cells [10], making them appealing technologies for autonomous brain implants and neuroprosthetics.

This thesis fits into the theoretical and practical context of neural emulation with organic transistor devices, with a focus on the mimicking of Short-Term Plasticity response and an attempt to add an unprecedented level of tunability. When organic transistor architectures are operated to produce a neuromorphic response, two of the three terminals are typically short-circuited together, resulting in a *de facto* two-terminal architecture [11] with a time/frequency response that mirrors the circuit's effective RC time constant. This time constant is affected by geometrical factors such as channel thickness [12], by the careful integration of shallow traps, such as those created with Au nanoparticles [10], by the composition of the electrolyte, or by the presence of molecules that interact strongly with the active layer. The latter situation, in particular, allowed the use of STP timescale as a sensing parameter toward analytes in the electrolyte demonstrating strong, albeit nonspecific, interactions with the active material [8]. In all these strategies, depressive STP is generated when the voltage spike train has a frequency greater than the inverse of the device response characteristic time scale.

In other three-terminal approaches[13–16],STP has been achieved in poly(3,4-ethylenedioxythiophene) :polystyrenesulfonate (PEDOT:PSS)-based or poly(3-hexylthiophene) (P3HT)-based EGOTs by continuously recording I_{DS} while applying pulses at the gate electrode and exploiting the rather slow bulk de-doping/doping of semiconductive channels to achieve nonlinearity of the I_{Ds} response according to the stimulation frequency. LTP, on the other hand, has been generated by faradaic processes such as lithium intercalation in graphene field effect transistor channels [17].

By modifying the typical connection paradigm of two-terminal devices, an artificial three-electrode synapse is provided in this work, **Figure 9 a** and **b**, in which the doping state of the channel is kept constant throughout the whole stimulation protocol by administering a constant V_{GS}. V_{DS} square pulsing

induces a STP depressing response in I_{DS}, allowing for selective and reversible modulation of STP behaviour via V_{GS}-mediated regulation of channel doping. STP responses are obtained by applying two stimulation paradigms: the first makes advantage of train pulse stimulation at various frequencies, **Figure 9 c**, while the second evaluates the STP response at a single frequency pulsed-train, **Figure 9 d**. Notably, the gate voltage causes no redox reaction in the active layer.

The rationale is that, by eliciting STP modulation of I_{DS} through square pulse V_{DS} stimulation, it is conceivable to use V_{GS} as an additional tuning parameter for controlling charge carrier density in the semiconductive channel, thereby regulating both the STP amplitude and STP time constant simultaneously. The gate also permits to set the baseline current before and after the STP response, providing an additional element for memory writing.

In **Figure 9 a** and **b**, the device layout and connection scheme are reported. A Pt gate electrode with controlled area allows the application of a continuous voltage with respect to the common ground. For the neuromorphic varying frequency characterisation, i.e., using the stimulation paradigm in **Figure 9 c**, the amplitude of the input square wave is 0.5 V, and each spike lasts 1 ms; square-wave frequency is varied each 100 ms. The drain is kept at a rest potential of -0.3 V to provide a continuous driving force for holes moving in the channel. For each stimulation train the gate bias is kept constant. Neuromorphism has been recorded at different doping levels, by varying V_{GS} from -0.6 V (fully doped channel) to 0.6 V (fully de-doped channel) by steps of 0.2 V. The pulse train simulates the spiking activity of a presynaptic neuron which causes, as a response, the release of ions and neurotransmitters towards the postsynaptic one.

In biological synapses, the response may be depressive or facilitative according to the stimulation frequency. The vision of this work is to exploit V_{GS} as a frequency-independent tuning parameter, eventually simulating the synaptic weight. The I_{DS} versus V_{GS} current response of an EGOT after train pulse stimulation at different frequencies is shown in **Figure 10 a**. It is feasible

to identify distinct current behaviour, both in time response and magnitude of the elicited response, depending as expected on the frequency of stimulation and, interestingly, on the applied gate bias. Baseline variations induced by gate voltage input are evident in the stimulation-free time span of the post-synaptic current trace (from 0ms to 100ms). Amplitude response to the first stimulation train (v=50 Hz) sows linear behaviour, with each current spike having the same intensity as the previous one.
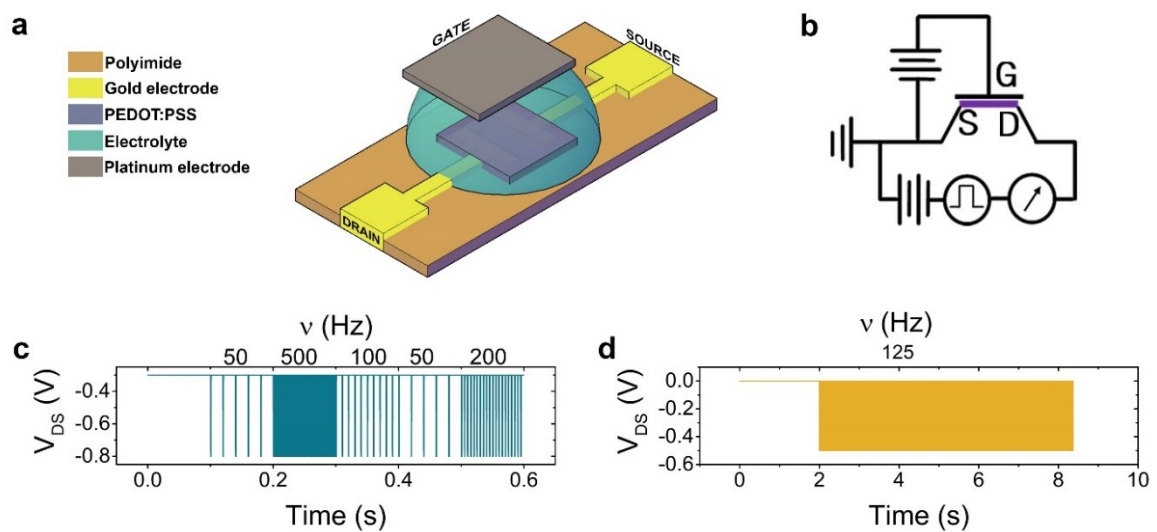
Figure 9. a) EGOT illustration featuring a platinum gate, b) Connection layout for neuromorphic device characterization, c) Multi-frequency stimulation paradigm entails using a square pulsed voltage train with an amplitude of -0.5 V and a DC-offset of -0.3V between drain and source, d) Single frequency stimulation paradigm requires a square pulsed voltage train with an amplitude of -0.5 V and a null DC-offset between drain and source electrodes.

Increasing the stimulation frequency to 500 Hz causes depressive behaviour, which implies that the n-th spike is more intense than the (n+1)-th, and so on, with a peculiar decreasing trend that will be addressed in detail later. Reducing the stimulation frequency to 100 Hz leads to facilitative behaviour, with the system progressively returning to its pristine state. This is followed by another 50 Hz stimulation to determine full recovery and another high-frequency stimulation to achieve less depressive behaviour (v=200 Hz). The typical response of neuromorphic two-terminal devices is qualitatively preserved [5,7]; namely, a linear response at low frequencies, a depressing
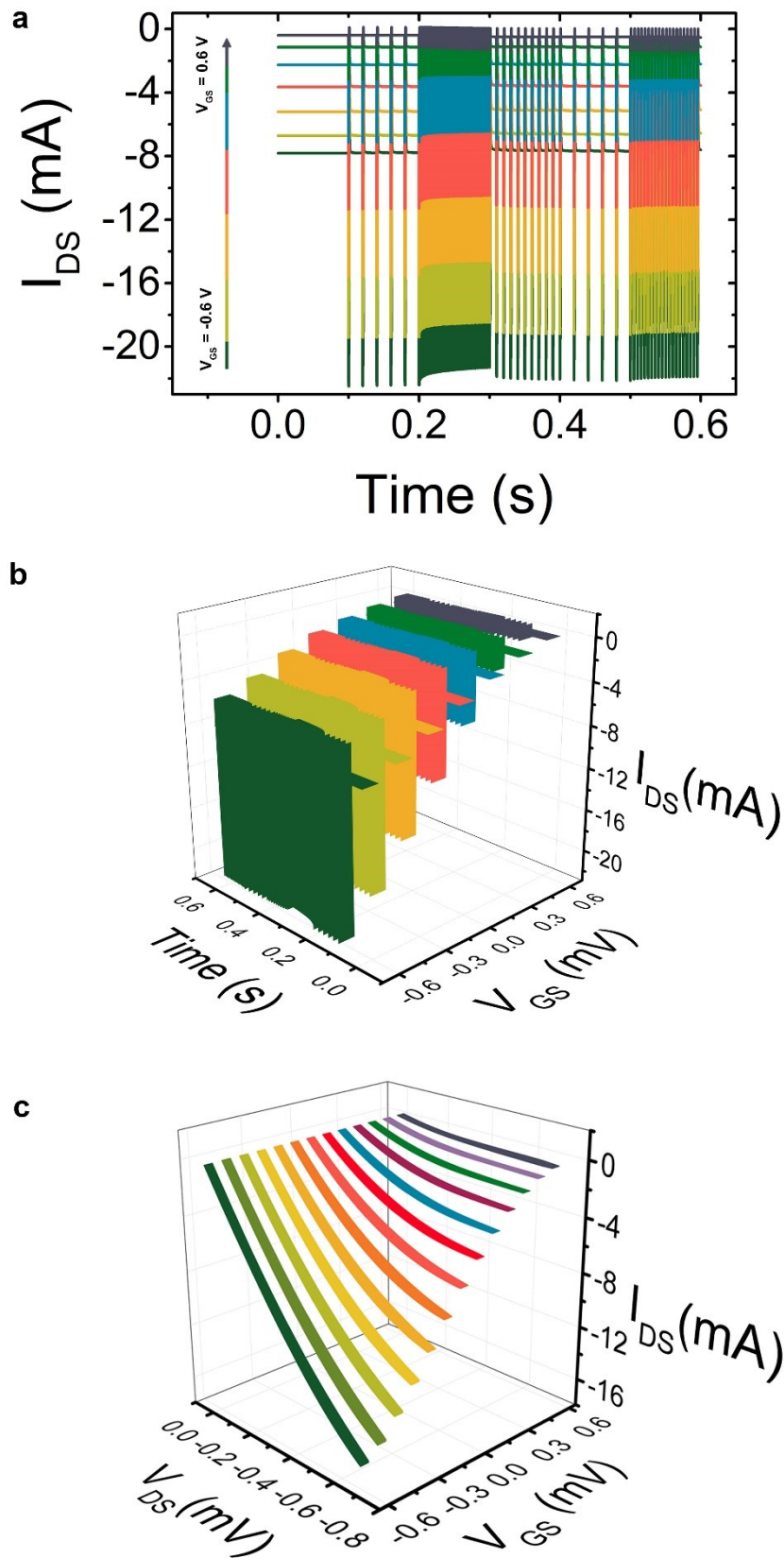
Figure 10. a) EGOT response to a V_{DS} multi-frequency pulse train ($V_{DS,DC\ OFFSET}$ = −0.3 V; ΔV_{DS} = −0.5 V) at different V_{GS} values, b) 3-D plot time vs V_{GS} vs I_{DS} highlighting amplitude scaling with V_{GS}, c) 3-D output curve V_{DS} vs V_{GS} vs I_{DS} showing the current amplitude attenuation in steady-state EGOT characterisation, mirroring current amplitude scaling in STP response.

response at high frequencies, and a facilitating response (i.e., increasing current spike amplitude) when moving from high to low frequencies can be observed. Nonetheless, it is conceivable to regulate this behaviour in a three-terminal architecture, eventually suppressing the neuromorphic response for totally de-doped channels (i.e., V_{GS} =0.6V).

This behaviour is caused by the different types of charge transport phenomena that contribute to I_{DS} in response to V_{DS} pulses: the variable-range hopping of holes in the semiconductive channel (slow phenomenon) and the displacement of ions in the electrolyte in response to square waver (fast phenomenon).
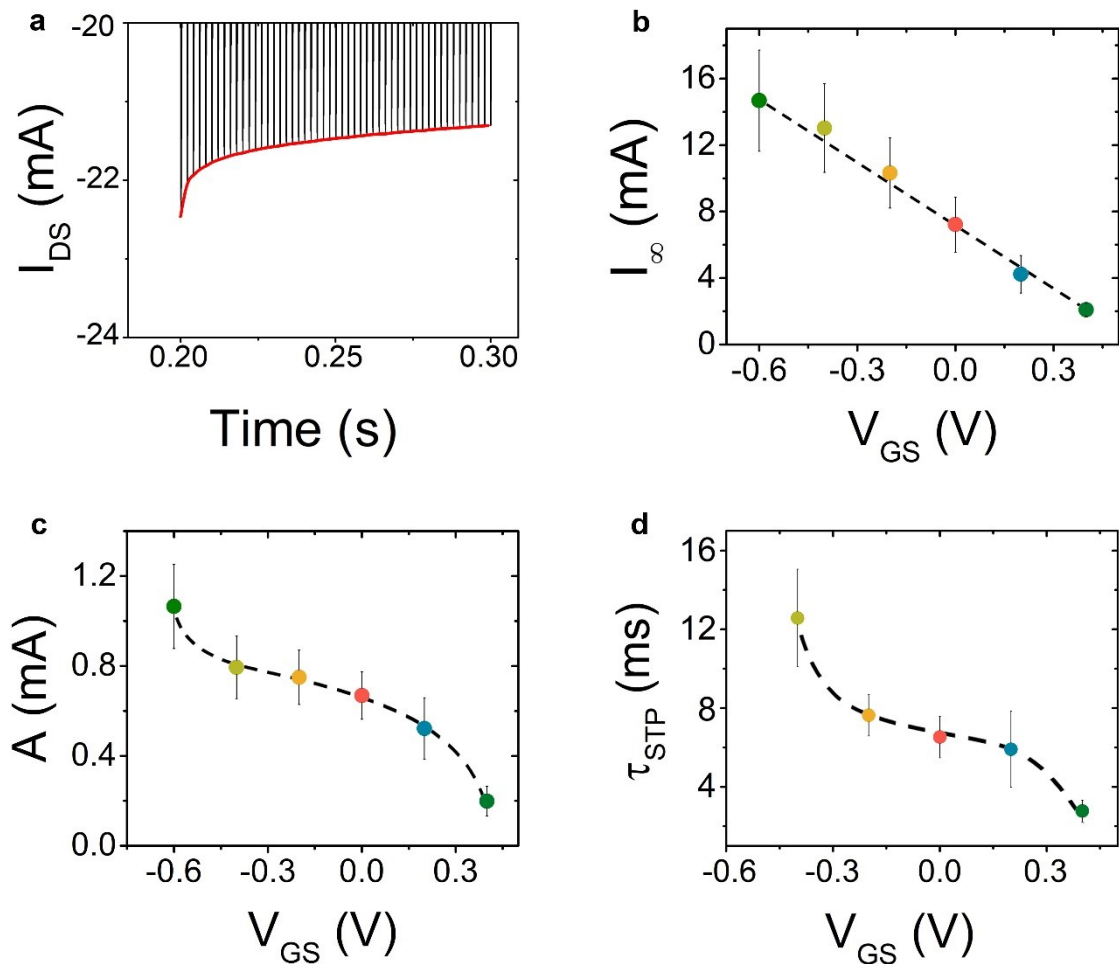
Figure 11. a) Zoom on the depressive STP responses at 500 Hz (black line) and STP envelopes (red line) for depletion device, b) Dependency of current plateau, I∞, on V_{GS}, c) dependency of current amplitude, A, on V_{GS}, d) Dependency of the STP characteristic time on V_{GS}. The error bars in b), c), and d) represent the standard deviation over three samples. Dashed lines are guide for the eyes.

When the channel is fully doped and I_{DS} is mainly contributed by holes, the slower timescale of charge transport in the channel dominates, and high stimulation frequencies cause depressive response due to slow recovery timescale. On the other hand, when the channel is totally de-doped, holes become trapped and I_{DS} occurs solely because of ion displacement, resulting in reduced current intensity albeit with faster relaxation time. In this case, even high stimulation frequencies are insufficient to cause depression, and the device response is linear (although weak).

The influence of gate potential on the magnitude of the current response is depicted clearly in **Figure 10 b**. In terms of current magnitude, the gate-mediated current response follows the same trend as the steady-state curves. **Figure 10 c** depicts a 3D-visualization of the output characteristics, collected by linearly scanning the V_{DS} potential between 0 and -0.7 V and changing V_{GS} by 0.1 V steps between -0.6 and 0.6 V. Examining the y-z plane (I_{DS} vs V_{GS}) in **Figure 10 b** and **c**, it is clear that when V_{GS} approaches positive values, the current response at the drain diminishes, implying that the mobile charge carrier density drops. As a result, the V_{GS} potential acts as a synaptic weight, creating a varied response depending on the "amount of available neurotransmitters", which are represented in our case by charge carriers (holes or ions) between source and drain. The addition of V_{GS} as an independent variable increases the degree of freedom in establishing the system's resting state, in terms of doping state and, thus, of channel conductivity.

Focusing on the STP depressive response at 500 Hz, it is possible to evaluate plateaux, current amplitude, and time response trends. For this phenomenological analysis the current envelope in response to 500 Hz stimulation is extracted and modelled with a stretched exponential, **Figure 11 a**, equation 5:

$$I(t) = I_\infty + A \cdot \exp\left[-\left(\frac{\Delta t}{\tau_{STP}}\right)^\beta\right] \tag{5}$$

where I_∞ is the current plateau related to the reached equilibrium upon continuous depressive stimulation, $A = I_0 - I_\infty$ is the difference between the first spike, I_0, and I_∞, t_0 is the time of the first spike, $\Delta t = t - t_0$ is the time (locked to the start of the stimulation), τ_{STP} is the STP time scale, and the exponent, β, quantifies the deviation from a purely exponential trend (which is instead usually observed in two-terminal devices) [18,19].

I_∞ and A as a function of V_{GS} are reported in **Figure 11 b** and **c**, confirming the previously discussed trend: increasing V_{GS} towards more positive values, both the current plateau and the amplitude of the neuromorphic response decrease, together with the channel conductivity. **Figure 11 d** shows that the characteristic timescale of the induced neuromorphic response decreases as V_{GS} increases. If we look at the characteristic time of the circuit, collected with electrochemical impedance spectroscopy (Appendix A), namely τ_{EIS}, **Figure 13 h**, we can see that devices with faster relaxation times (i.e., smaller τ_{EIS}) have a longer τ_{STP}. This is hardly surprising given that STP results from the system's incomplete relaxation after persistent spiking.

At a given stimulation frequency, in a system with a smaller τ_{EIS}, the magnitude of the second spike will be closer to that of the first spike, resulting in the requirement for more spikes (i.e., longer periods) to attain a steady state, leading to a longer τ_{STP}. V_{GS} allows to switch, hence, from to a slower to a faster system.

Furthermore, by zooming in on the "depressive range," **Figure 12 a**, it is verifiable that all these phenomena are retained at the single spike level. Aside from the aforementioned drop in intensity, significant evolution of the system's relaxation timescales may be observed when pulses are applied and removed. Interestingly, if no DC drain bias is applied (i.e., if $V_{DS,0} = 0$ V), these two processes (pulse application and pulse removal) can be decoupled, as illustrated in **Figure 12 b**.

To specify the operating parameters required for predicting and modifying the STP response in a three-terminal device, a quantitative toolset that
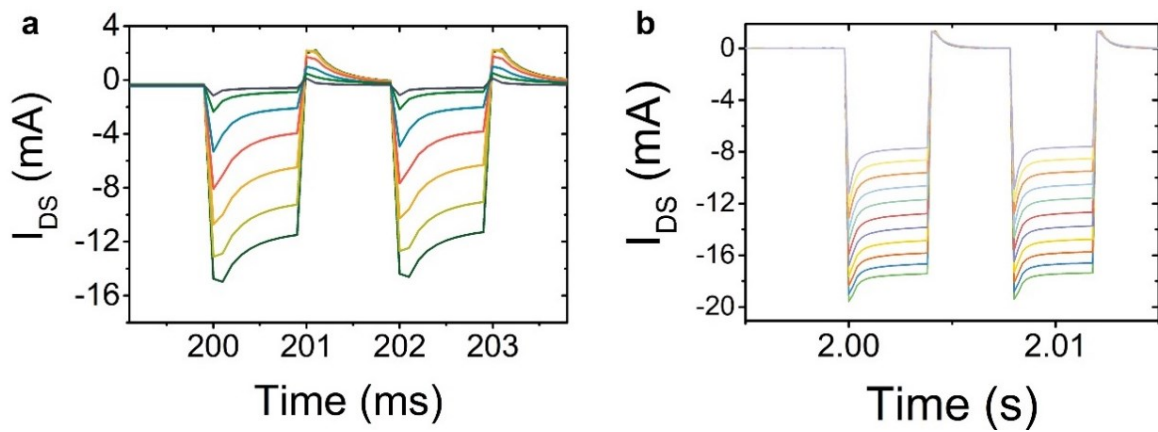
Figure 12. a) Detail of I_{DS} variations in the depressive region at 500 Hz, highlighting the dependency of both spike amplitude and relaxation time scales on V_{GS}; b) system response to depressive stimulation frequency (125 Hz) for $V_{DS,DC\ OFFSET} = 0$ V, for $-0.5 < V_{GS} < 0$V.

rationalizes these phenomena is required. This is accomplished in this work by concentrating on the STP depressive response at 125 Hz at $V_{DS,0} = 0$ V, for V_{GS} values ranging from 0 V to 0.5 V, thereby using the stimulation paradigm depicted in **Figure1d**. This potential window was chosen because it allows for modulation of the conductivity of most p-type organic semiconductors while ruling out any faradaic contribution to the observed currents [20]. The STP depressive response, characterized by a decreasing envelope of the current maxima in response to subsequent voltage spikes shown in **Figure 13 a**, follows the stretched exponential trend of equation 5. **Figure 13 b** and **c**, illustrate the I_∞ and A vs V_{GS} trends for depletion EGOTs. In depletion devices, the increasing trend of I∞ for higher channel doping (i.e., more negative VGS and higher negative I∞) is reflected by a decrease in STP amplitude, A. This is due to the fact that, for negative V_{GS}, conduction in PEDOT:PSS approaches metallic conduction, resulting in a partial loss of tunability. The stretching exponent β, plot vs V_{GS} in **Figure 13 d**, is a measure of how far the STP decay deviates from the exponential ideality. β < 1, in the three-terminal architecture, produces a less steep decay. This suggests energy disorder and drift velocity dispersion in semiconductive channels, and it differs from displacement-based STP in two-terminal structures, where β = 1. Therefore, β increases with channel doping and approaches unity, resulting in steeper decays. Since the sampled time for a train of voltage pulses may be shorter

than the STP time scale (in some instances, this falls outside the range of experimental time, implying that the STP plateau is not fully achieved for the duration of the pulse train), the estimated errors on the fitting parameters are large, necessitating a step-and-hold fitting procedure for convergence. As a consequence, it is useful to recast equation 5 and execute a Taylor expansion into a power law, equation 6, which may then be linearized as equation 7.

$$I(t) \approx I_0 + I_\infty \cdot \left(\frac{\Delta t}{\tau_{STP}} \right)^\beta \tag{6}$$

$$\ln \left[\frac{I(t) - I_0}{1A} \right] = \left[\ln \left(\frac{I_\infty}{1A} \right) - \beta \cdot \ln \left(\frac{\tau_{STP}}{1s} \right) \right] + \beta \cdot \ln \left(\frac{\Delta t}{1s} \right) = \alpha + \beta \cdot \ln \left(\frac{\Delta t}{1s} \right) \tag{7}$$

The fit with equation 7 is numerically robust, although the physical meaning of the parameters of equation 6 is not explicit, as the parameters are now entangled into the parameter α, which is plot vs V_{GS} in **Figure 13 f**. As demonstrated in **Figure 13 g**, the linearization procedure results in a modest underestimation of β values.

As already discussed, both α and β can be tuned by controlling V_{GS}. The parameter α, namely the value of $\ln[(I(t) - I_0)/1A]$ after 1 s of continuous depressive stimulation, is a generic indicator of the efficiency of the STP depression. In depletion devices, α peaks near 0 V, indicating that the channel is in its most energetically disordered condition. As a result, β shows a minimum in this potential window.

As already mentioned, also in this case τ_{STP}, **Figure 13 e**, shows inverse dependency on V_{GS} with respect to the circuit RC time constant τ_{EIS}, extracted from impedance spectroscopy and shown in **Figure 13 h**

In conclusion, a novel neuromorphic architecture based on electrolyte-gated organic transistors was developed and verified, allowing reversible control of the neuromorphic depressive response's amplitude, rate, and current plateau in response to V_{GS} modulation.
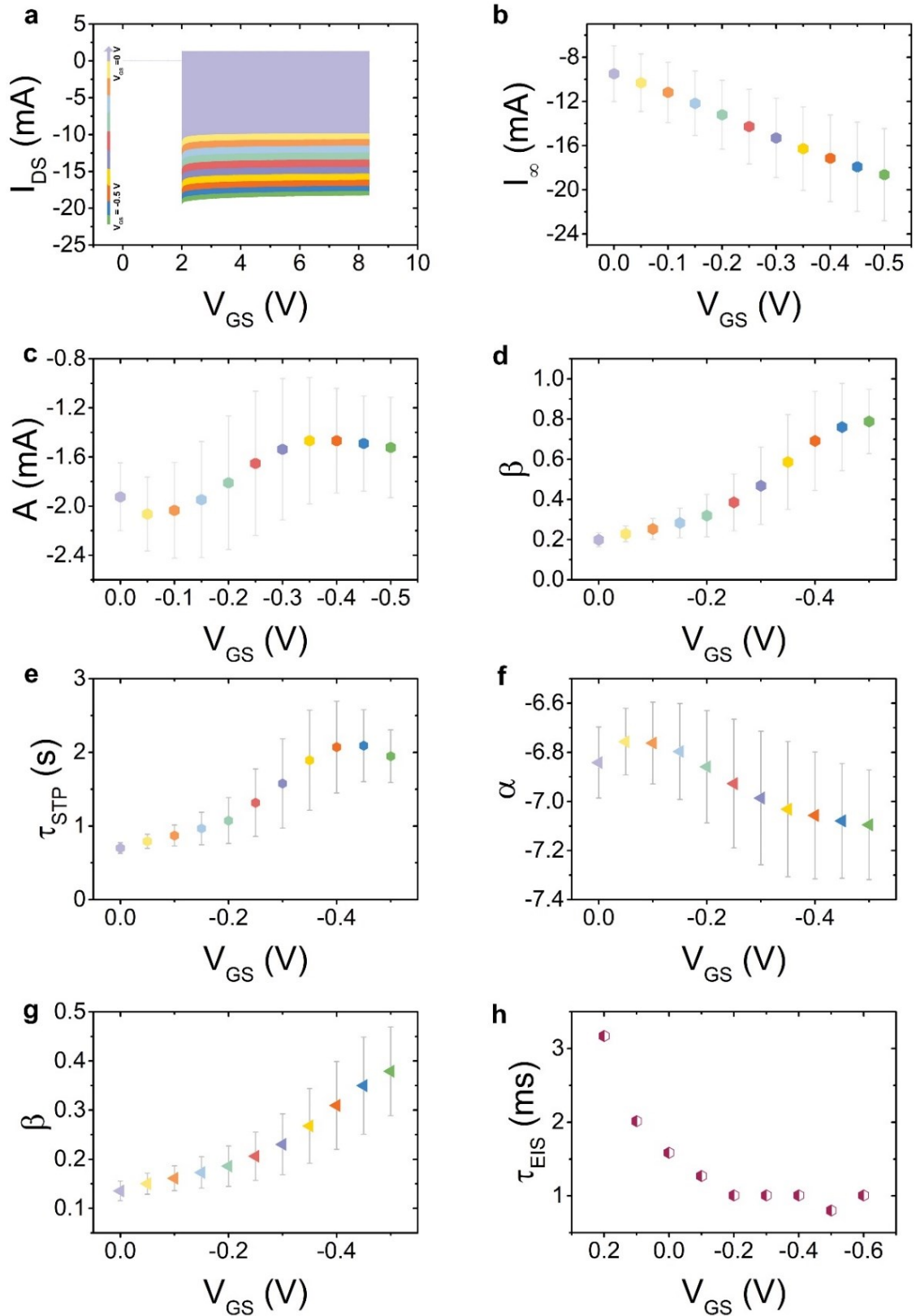
Figure 13. EGOT responses to a V$_{DS}$ single-frequency pulse train (V$_{DS,DC OFFSET}$ = 0 V; ΔV$_{DS}$ = −0.5 V) at different V$_{GS}$ values, b) Dependency of current plateau, I$_\infty$, on V$_{GS}$, c) dependency of current amplitude, A, on V$_{GS}$, d) Dependency of the stretching exponent at different V$_{GS}$ values, e) Dependency of the STP characteristic time on V$_{GS}$, f) Dependency of the α parameter on gate potential bias, g) Dependency of β parameter from linearization on gate-source potential, h) EGOT characteristic time trend, from electrochemical impedance spectroscopy measurement , respect to V$_{GS}$ values. The error bars in b), c), d), f), and g) represent the standard deviation over three samples.

It is possible to shift the baseline current, amplitude, and steepness of neuromorphic behaviour in the channel of organic electronic EGOT-based neuromorphic devices by properly controlling V_{GS}, including multilevel memory writing and frequency dependent controllable decisional nodes in more complex neuromorphic organic circuitry [21–23], as well as tailorable sensitivity in STP-based sensors [8,19,23].

Interestingly, the same tailoring approach is suitable for tuning the neuromorphic response of accumulation EGOTs, albeit with mirroring the figures of merit [24].

5.2 Single pulse response and paired-pulse plasticity

The interaction of gate, electrolyte, and channel, as well as their mutual reliance on operating factors such as gate-source and drain-source voltages, makes EGOTs a versatile tool for dynamic systems such as neuromorphic electronics. Dynamic phenomena following the out-of-equilibrium displacement (through an input signal) of the active material (the organic (semi-)conductor) initially at equilibrium with the operational electrolyte cause the neuromorphic response of organic electronic devices [19]. Since all the species dissolved in the solution affect the equilibrium, the artificial synapses will behave differently to varied solution compositions. When some solute species interact strongly with the material, the dynamics of recovering the equilibrium condition after the input signal is withdrawn can be extremely slow.

Artificial synapse architecture successfully detects moieties in solution that cause strong, albeit non-specific, interactions. Indeed, administering square voltage pulses at a fixed frequency (as an input signal) results in a kinetic imbalance between the processes of adsorption/retention and desorption/expulsion in/out of the organic active material for species with strong interactions [8,23,25]. Each input voltage pulse causes the organic (semi)

conductor to enter a "metastable" state with a different conductance level than the previous one (the baseline). A ladder of current spikes of varying intensities responds to the sequence of input voltage pulses, either lowering (depressive short-term plasticity - STP - response) or increasing (facilitating STP response).

Once in the final metastable state, the conductance/current relaxes to the initial baseline value with a timescale characteristic of the composition of the solution, of the baseline and of the features (amplitude, frequency, and number of spikes) of the input signal. This indicates that the initial and final conductance states of artificial synapses in response to a certain input signal are linked via a specific pathway. The behaviour of artificial synapse is clearly caused by the interaction of active material conductance and ion density in close proximity to the material itself, for this reason OMIECs [26] are often used in neuromorphic electronics.

If this is true in the steady-state, it becomes even more significant when dealing with transient phenomena, in which the substantial disparity between ion dynamics and charge transport dynamics causes a complicated out-of-equilibrium behaviour that is thought to be the source of the neuromorphic response. The Gibbs free energy plays an important role in determining the kinetics and magnitude of doping/de-doping processes in OMIECs, particularly the most common PEDOT:PSS, which has been demonstrated and exploited in the development of binding-energy-specific neuromorphic sensors. Recently, it was conclusively proven that OMIEC conductance in EGOTs is a cumulative observable that gives a thorough understanding of the electrolyte/OMIEC system's thermodynamic and kinetic conditions[27][28–30]. As previously discussed, this indicates that the gate electrode has a direct effect on the system's Gibbs free-energy and, as a result, on its response kinetics when used as an artificial synapse.

In this section the hypothesis of the previous one is further expanded and validated, demonstrating that a modulation of the DC offset at the gate electrode - usually referred to as the pre-synaptic terminal in neuromorphic

architectures - implies not only a modulation of steady-state observables like channel (trans-)conductance but also a difference in transient aspects like the temporal evolution of the "post-synaptic" channel current, even when neuromorphism is not elicited by another pulsed voltage, such as in section 5.1.

Such effect of DC offset at the gate on neuromorphic phenomena can be rationalized in terms of exchanged charge upon programming. Consequently, it is necessary to extensively characterize the channel response upon the application of square pulses. In particular, the DC gate effect will be quantified upon single pulse and paired-pulse stimulation protocol.

A single square voltage pulse, both negative and positive is applied at the gate electrode, namely pre-synaptic electrode, while measuring the elicited current in the post-synaptic channel between source and drain electrodes, **Figure 14 a**. Stimulation protocol is depicted in **Figure 14 b** and **c** (top panel) for negative and positive square pulsed voltage respectively. The measured post-synaptic I_{DS}, **Figure 14 b** and **c** (central panels) is then integrated in time to obtain chronocoulograms (Q vs t), here reported in terms of charge variation (ΔQ) with respect to the charge value before pulse administration **Figure 14 b** and **c** (bottom panels). This protocol is repeated for various DC $V_{GS,Offset}$ values, ranging from -0.7V to 0.7V.

Regarding the single negative pulse, **Figure 14 d**, it is possible to see how there is a linear temporal profile of Q during the pulse, whose slope (i.e. magnitude for constant pulse duration) relies on the applied $V_{GS,Offset}$.

In response to positive single pulses, phenomenologically comparable behavior can be observed, albeit with an opposite sign and magnitude, **Figure 14 e**.

Figure 14 f and **g** demonstrate the magnitude of the exchanged charge in the channel after pulse administration as a function of $V_{GS,pulse}$ for negative
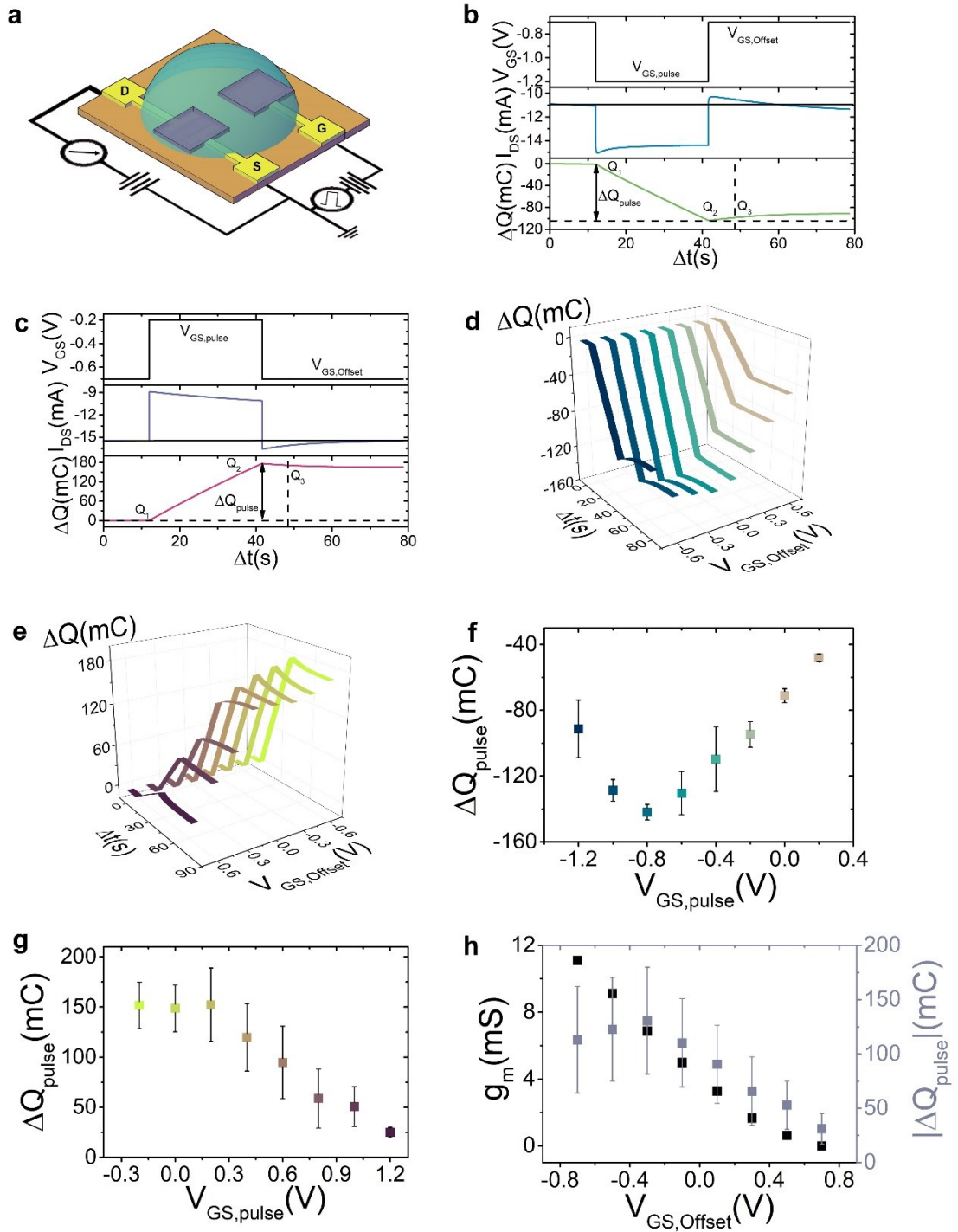
Figure 14. a) Connection layout for neuromorphic device characterization, b) Single negative square pulse panel. Cronovoltammogram (black solid line) applied at the pre-synaptic electrode, Cronoamperogram (light blue line) measured at the post-synaptic channel and Cronoculogram (green line) for a negative single pulse, c) Single positive square pulse panel. Cronovoltammogram (black solid line) applied at the pre-synaptic electrode, Cronoamperogram (light purple line) measured at the post-synaptic channel and Cronoculogram (pink line) for a positive single pulse, d) and e) 3D-plot,Δt vs V_{GS} vs ΔQ, of the exchanged ΔQ during the negative (d) or positive (e) square pulse protocol, f) and g) Exchanged channel charge during the negative (f) and positive (g) pulse at different $V_{GS,pulse}$ (n=4, standard deviations as error bars); (g) Transconductance and absolute value of the average Δ_{Qpulse} (n=4, propagated standard deviations as error bars) vs $V_{GS,Offset}$.

and positive voltage pulses, respectively. Here $V_{GS,pulse} = V_{GS,Offset} - 0.5V$ for negative pulses and $V_{GS,pulse} = V_{GS,Offset} + 0.5V$ for positive ones. The non-linear patterns in **Figures 14 f** and **g** can be explained by assuming that the charge exchanged in the channel during a single pulse is affected by channel doping prior to pulse administration as well as its proneness to change, as measured by transconductance. Indeed, both are set by $V_{GS,Offset}$. **Figure 14 h** illustrates an overlay between the trends of transconductance, gm, and the absolute value of charge exchanged in the channel during pulse administration, $|Q_{pulse}|$, vs $V_{GS,Offset}$. When transconductance reaches its maximum, the charge variation saturates, as a consequence of the energy disorder of the channel expressed by the previously introduced parameter β.

As seen in **Figures 14 d** and **e**, ΔQ does not always remain constant when the pulse is removed. However, it may exhibit distinct relaxation kinetics that vary with $V_{GS,Offset}$, and hence with g_m before attaining a steady-state value. For high transconductances, the system exhibits overcharging - or overdepletion for positive pulses - upon pulse administration, which must be recovered in time following the kinetics of the appropriate displaced charged species (i.e., anions or cations) in the electrolyte at the channel interface. In low transconductance regimes, however, pulse removal causes entire cessation of charge exchange in the channel in the case of negative pulses and sluggish charge accumulation in the case of positive pulses. This significant discrepancy can be attributed to the varied sign and hydrodynamic volume of the ions that enter the channel based on the pulse sign, as well as the "accessible" coordination sites for ions present in the channel, as determined by $V_{GS,Offset}$.

In this view, kinetic processes closely resemble transconductance behaviour and, as a result, transconductance nonlinearity is at the root of neuromorphic tunability in EGOTs. A paired-pulse experiment is carried out to validate these concepts, investigating depressive and facilitating phenomena on square paired-pulses, with an amplitude of -0.5 V, at the pre-

synaptic electrode, while varying the interstimulation interval (ISI) from 20 ms up to 200 s switching $V_{GS,offset}$ from -0.7 V to 0.7 V. **Figure 14 a** depicts the connection layout, while **Figure 15 a** depicts the operating paradigm. A quantitative depiction of the entity of depression/facilitation can be provided by defining a paired-pulse plasticity index – PPP_i, equation 8:

$$PPP_i = 1 - \frac{A_2}{A_1} \qquad\qquad (8)$$

Where, A_1 and A_2 are the differences between post-synaptic current peaks (in response to the first and the second pre-synaptic pulse, respectively) and the baseline current value before pulse administration, as shown in representative traces in **Figure 15 a**. Positive values of PPP_i indicate a depressive response while negative values testify a facilitative behaviour; in both cases, $|PPP_i|$ measures the entity of the phenomenon. Furthermore, **Figure 15 b** shows a comprehensive evaluation of PPP_i's dependence on V_{GS} and ISI, allowing us to discriminate between four key scenarios. In particular:

- when ISI is short and the semiconductive channel is turned on (i.e. at negative $V_{GS,offset}$ values), a depressive response with $PPP_i > 0$ is observed;
- when ISI is short and the semiconductive channel is turned off (i.e. at positive $V_{GS,offset}$ values), the system responds linearly with $PPP_i \approx 0$;
- when ISI is high and the channel is active, the system produces a depressive reaction, albeit of lesser size (i.e., smaller positive PPP_i values);
- when ISI is lengthy and the channel is turned off, consistent potentiation of the post-synaptic current (i.e., $PPP_i < 0$) is achievable.

A different set of intermediate conditions can be achieved by moving between these four extremes, allowing users to arbitrarily select PPP_i by properly tweaking ISI and $V_{GS,offset}$.

In a synthetic resume, when the interstimulation interval is lengthy and the channel is kept unaltered for a long period of time while being subjected to a constant $V_{GS,offset}$ value, its conductivity tends to rise and its neuromorphic

behaviour is modulated as a consequence. This is interesting because, in principle, a constant $V_{GS,offset}$ should imply a constant ionic environment close to the channel, resulting in a single conductivity value in EGOTs. The fact that this effect is stronger in the case of positive $V_{GS,offset}$, when cations are forced at the interface with the PEDOT:PSS channel, suggests the

presence of slow rearrangement phenomena that allow the system to "cope" with the presence of cations and partially restore its conductivity over time. This explanation, which ultimately implies the presence of kynetically
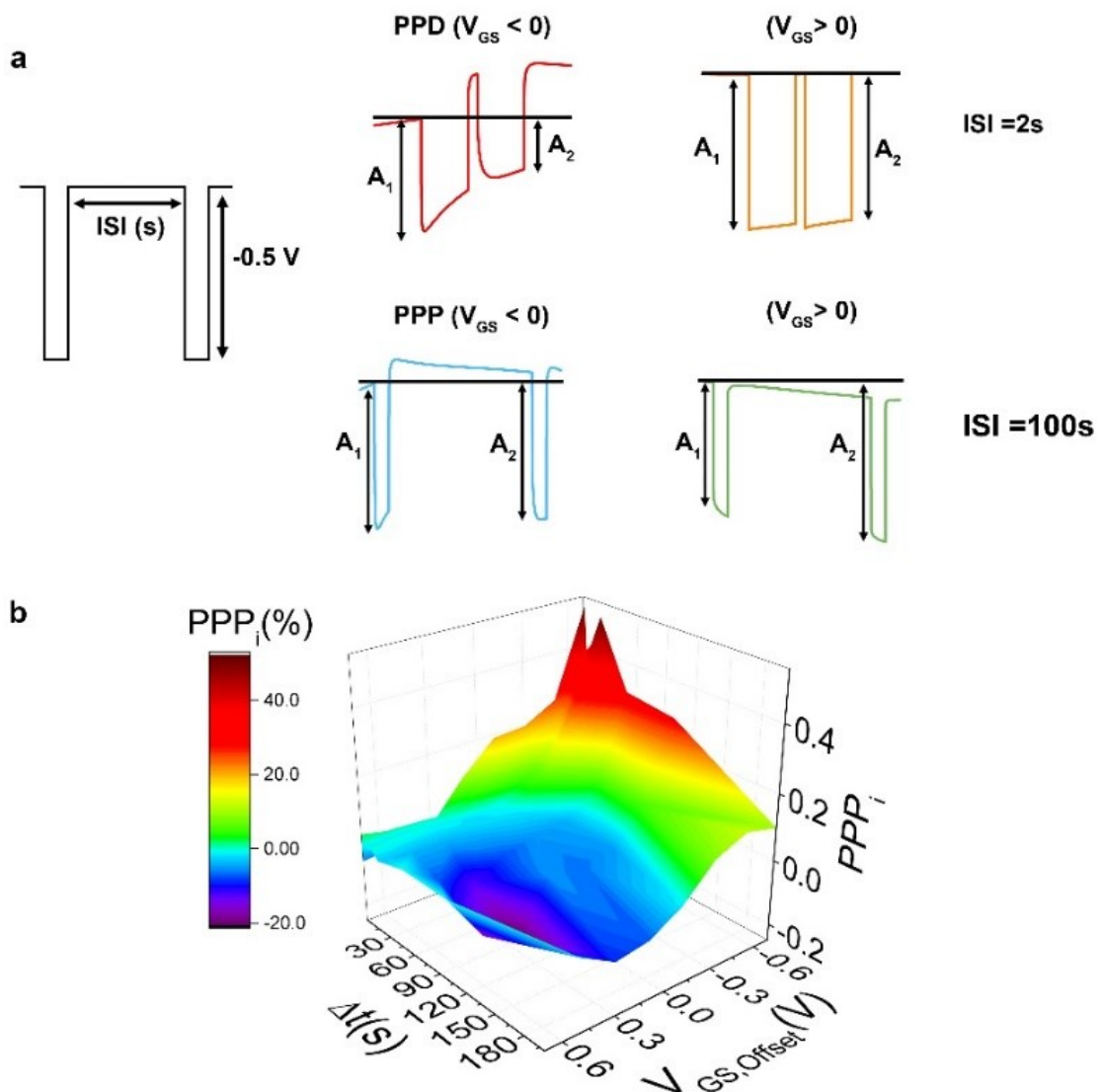
Figure 15. a) For varying ISI lengths, a schematic representation of pre-synaptic voltage paired pulses (on the left) and recorded post-synaptic currents (on the right) highlighting the depressing and facilitative behaviour induced by the application of $V_{GS,Offset}$ at the presynaptic terminal, b) To quantify plasticity phenomena, a 3D surface is created that links the applied DC $V_{GS,Offset}$ with the ISI in seconds and an averaged paired pulse plasticity index (PPP$_i$, n=4).

stored electrostatic energy in PEDOT:PSS films at the electrolyte interface, is consistent with previous reports of the presence of electrochemical pseudo-inductive contributions to such interfaces[25], which give rise to facilitative plasticity responses at long ISI and broadens the applicability context of neuromorphic EGOTs.

BIBLIOGRAPHY

1. Chua, L. Memristor-The missing circuit element. *IEEE Trans. Circuit Theory* **18**, 507–519 (1971).

2. Strukov, D. B., Snider, G. S., Stewart, D. R. & Williams, R. S. The missing memristor found. *Nature* **453**, 80–83 (2008).

3. Burr, G. W. *et al.* Neuromorphic computing using non-volatile memory. *Adv. Phys. X* **2**, 89–124 (2017).

4. Rivnay, J., Owens, R. M. & Malliaras, G. G. The rise of organic bioelectronics. *Chem. Mater.* **26**, 679–685 (2014).

5. Keene, S. T., Gkoupidenis, P. & Burgt, Y. van de. Neuromorphic computing systems based on flexible organic electronics. in *Organic Flexible Electronics* 531–574 (Elsevier, 2021). doi:10.1016/B978-0-12-818890-3.00018-7.

6. Simon, D. T., Gabrielsson, E. O., Tybrandt, K. & Berggren, M. Organic Bioelectronics: Bridging the Signaling Gap between Biology and Technology. *Chem. Rev.* **116**, 13009–13041 (2016).

7. van de Burgt, Y., Melianas, A., Keene, S. T., Malliaras, G. & Salleo, A. Organic electronics for neuromorphic computing. *Nat. Electron.* **1**, 386–397 (2018).

8. Giordani, M. *et al.* Specific Dopamine Sensing Based on Short-Term Plasticity Behavior of a Whole Organic Artificial Synapse. *ACS Sens.* **2**, 1756–1760 (2017).

9. Martin, S. J., Grimwood, P. D. & Morris, R. G. M. Synaptic Plasticity and Memory: An Evaluation of the Hypothesis. *Annu. Rev. Neurosci.* **23**, 649–711 (2000).

10. Desbief, S. *et al.* Electrolyte-gated organic synapse transistor interfaced with neurons. *Org. Electron.* **38**, 21–28 (2016).

11. Alibart, F. *et al.* An Organic Nanoparticle Transistor Behaving as a Biological Spiking Synapse. *Adv. Funct. Mater.* **20**, 330–337 (2010).

12. Gerasimov, J. Y. *et al.* An Evolvable Organic Electrochemical Transistor for Neuromorphic Applications. *Adv. Sci.* **6**, 1801339 (2019).

13. Gkoupidenis, P., Schaefer, N., Garlan, B. & Malliaras, G. G. Neuromorphic Functions in PEDOT:PSS Organic Electrochemical Transistors. *Adv. Mater.* **27**, 7176–7180 (2015).

14. Qian, C. *et al.* Artificial Synapses Based on in-Plane Gate Organic Electrochemical Transistors. *ACS Appl. Mater. Interfaces* **8**, 26169–26175 (2016).

15. Ling, H. *et al.* Electrolyte-gated transistors for synaptic electronics, neuromorphic computing, and adaptable biointerfacing. *Appl. Phys. Rev.* **7**, 011307 (2020).

16. Hu, Y. *et al.* Diverse Synaptic Plasticity Induced by the Interplay of Ionic Polarization and Doping at Salt-Doped Electrolyte/Semiconducting Polymer Interface. *ACS Omega* **2**, 746–754 (2017).

17. Sharbati, M. T. *et al.* Low-Power, Electrochemically Tunable Graphene Synapses for Neuromorphic Computing. *Adv. Mater.* **30**, 1802353 (2018).

18. Friedlein, J. T., McLeod, R. R. & Rivnay, J. Device physics of organic electrochemical transistors. *Org. Electron.* **63**, 398–414 (2018).

19. Giordani, M. *et al.* Neuromorphic Organic Devices that Specifically Discriminate Dopamine from Its Metabolites by Nonspecific Interactions. *Adv. Funct. Mater.* **30**, (2020).

20. Cramer, T. *et al.* Water-gated organic field effect transistors-opportunities for biochemical sensing and extracellular signal transduction. *J. Mater. Chem. B* **1**, 3728–3741 (2013).

21. Harikesh, P. C. *et al.* Organic electrochemical neurons and synapses with ion mediated spiking. *Nat. Commun.* **13**, 901 (2022).

22. Harikesh, P. C. *et al.* Ion-tunable antiambipolarity in mixed ion–electron conducting polymers enables biorealistic organic electrochemical neurons. *Nat. Mater.* (2023) doi:10.1038/s41563-022-01450-8.

23. Sarkar, T. *et al.* An organic artificial spiking neuron for in situ neuromorphic sensing and biointerfacing. *Nat. Electron.* **5**, 774–783 (2022).

24. Di Lauro, M. *et al.* Tunable Short-Term Plasticity Response in Three-Terminal Organic Neuromorphic Devices. *ACS Appl. Electron. Mater.* **2**, 1849–1854 (2020).

25. Calandra Sebastianella, G. *et al.* Implantable Organic Artificial Synapses Exhibiting Crossover between Depressive and Facilitative Plasticity Response. *Adv. Electron. Mater.* **7**, 2100755 (2021).

26. Paulsen, B. D., Tybrandt, K., Stavrinidou, E. & Rivnay, J. Organic mixed ionic–electronic conductors. *Nat. Mater.* **19**, 13–26 (2020).

27. Rebetez, G., Bardagot, O., Affolter, J., Réhault, J. & Banerji, N. What Drives the Kinetics and Doping Level in the Electrochemical Reactions of PEDOT:PSS? *Adv. Funct. Mater.* **32**, 2105821 (2022).

28. Rivnay, J. *et al.* Organic Electrochemical Transistors with Maximum Transconductance at Zero Gate Bias. *Adv. Mater.* **25**, 7010–7014 (2013).

29. Tarabella, G. *et al.* Effect of the gate electrode on the response of organic electrochemical transistors. *Appl. Phys. Lett.* **97**, 123304 (2010).

30. Tan, S. T. M. *et al.* High-Gain Chemically Gated Organic Electrochemical Transistor. *Adv. Funct. Mater.* **31**, 1–9 (2021).

Chapter 6:Translational neuroelectronics

This Chapter focusing on EGOTs translational aspects in electrophysiology. A novel connection layout to operate organic transistor in a harmless way is demonstrated in vitro and in vivo. Conformable epicortical array featuring EGOTs as recording sites are designed and validated in vitro. Finally, an organic circuit for real-time signal sorting is introduced.

6. Transistor-based Neuroelectronics and organic circuitry

In vision to develop more performing brain-machine interfaces (BMIs) [1–3], electrolyte – gated organic transistors (EGOTs) which can provide *in situ* amplification of the neurophysiological signal, can be implemented. When EGOTs are translated in a neurophysiological scenario, device performance can be assessed according to three criteria: safety, transconductance and cut-off frequency (bandwidth). However, translational application of EGOT technology generally suffers from poor resolution since transistor miniaturization is still challenging.

Transconductance is a blessing and a curse for the implementation of miniaturized organic transistor in micro-epicortical arrays. According to the Friedlein model, the channel current depends on Wd/L meanwhile the cut-off frequency of the device is proportional to $d(wl)^{-(1/2)}$, where W is the channel width, L is the channel length and d is the thickness of the polymeric film [4,5]. This different dependence on geometrical parameters establishes a trade-off between these two features: device with high transconductance usually show low cut-off frequency and vice versa [4].

However, In the latest years, several authors have investigated this braided behaviour between gm and cut-off frequency, enabling the design of new EGOTs architecture by tuning W/L ratio and/or d. Nevertheless, many new EGOT architectures have been only characterised in vitro with gate electrodes that cannot be translated in a physiological environment (e.g., Ag/AgCl electrode) [6–9].

Notably, even if optimization of their transducing and amplification performances is a widely investigated research which led to periodizing advancements, the same cannot be said for signal treatment and sorting strategies. To date the transduced (and possibly amplified) signal is transferred without any further treatment to *ex situ* computing units, which are deputed to perform off-line data analysis, selecting the pathophysiologically relevant spectral ranges, detecting and removing

artefacts and identifying diagnostic patterns. This signal treatment is often manually driven by operators, and it is time- and power-consuming, thereby strongly hampering the implementation of closed-loop operator-independent theranostic BMIs.

It is true that such properties are inherent to silicon transistor-based technology which incorporates hardware for amplifying, multiplexing, and processing into integrated circuits. However, mechanical and electrical properties of traditional electronics are, as already mentioned, not ideal for long-term implantation inside the body. Improvements to the materials forming all components of neuroelectronics devices are key to increasing the biocompatibility and long-term efficiency of such devices in physiological environments [10].

As in a painting, where every touch of colour leads to the completion of the final work, this chapter will introduce some novelties which tackle this entangled scientific problem from variegate perspectives, in particular presenting:

- a novel biasing scheme for organic transistors to avoid the application of a bias in the brain;
- the fabrication with standard clean-room procedures and the validation at the bench side of flexible epicortical probes featuring miniaturized organic transistors as recording sites;
- an organic flexible architecture for real-time signal sorting, prone to miniaturization and integration in BMIs, specifically designed to be coupled to EGOT-based in situ amplifiers.

6.1 A novel biasing scheme of electrolyte-gated transistor for neuroelectronics

The recording of bioelectrical activity from the brain is widely used for fundamental physiological research, such as the codification of superior

functionalities including speech perception and production [11-14], as well as clinical applications such as intraoperative monitoring of neural activity during tumour resection neurosurgery[15,16], identification of epileptic *foci* in chronic implants [17-19], and neuroprosthetics [20-22]. As previously stated, in order to reduce invasiveness while preserving significant task-related information, electrocorticographic (ECoG) and micro-electrocorticographic (ECoG) techniques underwent extensive research [23-26], resulting in noise enhancement due to electrode miniaturization and subsequent increased impedance [27-29].

In this circumstance, brain recordings would clearly benefit from an *in situ* first-stage signal amplification approach. Although inorganic field-effect transistors have been effectively proven as bioelectrical activity transducers in vitro [30], their applicability in vivo is hampered by the chemical and mechanical properties of inorganic semiconductors, particularly when exposed to wet environment [31]. As a result, inorganic transistors have been confined to the duty of integrated multiplexers for microelectrodes operating in encapsulated compartments not exposed to the brain [32]. Conversely, EGOTs are successfully demonstrated as transducers in vivo [4,9,33,34]. Section 2 has covered the architecture and operation of EGOTs. However, PEDOT:PSS-based EGOTs are typically operated in a common-source/common-ground (CSCG) configuration, and electrophysiological applications are no exception [9,34].

This means that the drain electrode is negatively biased with respect to the source, as imposed by the positive sign of the charge carriers, whereas the gate electrode can be either negatively or positively biased with respect to the same terminal, depending on the channel's desired doping state. The resulting net potential between gate and drain, which roughly corresponds to V_{GS}-V_{DS}, significantly exceeds the electrochemical stability window of water, thereby activating unwanted faradic processes in the electrolyte. If this phenomenon is a relatively minor issue (and possibly an advantage) in sensing applications [35], it is a major disadvantage in translational

electrophysiology since the generation of chlorine and hydrogen at the electrodes may induce critical tissue damage.

To overcome this issue, a novel operation mode for EGOTs is proposed and demonstrated in this thesis, intended to avoid the application of a DC-bias to the brain during electrophysiological acquisition, while keeping the device amplification features. The new mode of operation is straightforward and makes advantage of the finest operation peculiarities of source-measure units: the traditional common-source/common-ground configuration is reversed to achieve a common-drain/grounded-source (CDGS) configuration. A positive V_{DS} applied at the drain with regard to the grounded source produces a hole current in the p-type conductor from the drain to the source across the channel (i.e. a positive I_{DS} collected at the drain). The potential of the gate electrode regulating the electrochemical potential of the electrolyte and, subsequently, the channel doping level, is referenced to the drain, V_{GD}. In this way, the drain acts as a common terminal for both measuring and referencing, while the "source" electrode acts solely as ground terminal. Maximum transconductance in EGOTs can be achieved in this configuration by providing equal and opposite voltages to the drain (positive bias) and the gate (negative bias), resulting in net zero bias in the cerebro-spinal fluid with respect to the ground. The new CDGS configuration is evaluated and compared to the traditional CSCG configuration, first at the benchside then in vivo.

6.1.1 *In vitro* comparison between standard and proposed biasing schemes

EGOTs are fabricated as described in Section 4.2 and 4.4, and assayed at the benchside in 1M phosphate buffer saline (PBS) in both configurations, CSCG and CDGS. **Figure 16** depicts the connecting schemes of both layouts, **Figure 16 a** and **c**. The goal of this work is to define an operational condition

ensuring that electrophysiological activity is transduced with EGOTs operated in their maximum transconductance regime while, at the same time, avoiding the application of a bias in the operational electrolyte (i.e., PBS *in vitro* and cerebrospinal fluid *in vivo*). Using a bath electrode, **Figure 16 c** and **d**, the potential established in the electrolyte, V_{bulk}, can be probed while driving the transistor with a constant V_{DS} at various V_{GS} values (for CSCG) or V_{GD} values (for CDGS), as shown in **Figure 16 e** and **f**. In both cases, V_{bulk} exhibit linear trends vs the gate voltage, offset by a V_{DS}-dependent value. **Figure 16 e** and **f**. By fitting each data set to a linear regression, equations 9 and 10, it is possible to extract the slope and the intercept.

$$V_{bulk}=\Gamma+M^* \, V_{GS} \qquad\qquad \text{CSCG} \qquad\qquad (9)$$

$$V_{bulk}=\Phi+\Lambda^* \, V_{DS} \qquad\qquad \text{CDGS} \qquad\qquad (10)$$

In both cases, the slopes M and Λ equal 0.5 and, as a consequence, equations 9 and 10 can be recast as equations 11 and 12.

$$V_{bulk}=\Gamma+\frac{1}{2} \, V_{GS} \qquad\qquad \text{CSCG} \qquad\qquad (11)$$

$$V_{bulk}=\Phi+\frac{1}{2} \, V_{GD} \qquad\qquad \text{CDGS} \qquad\qquad (12)$$

By explicitating the dependency of Γ and Φ on V_{DS} it is possible to develop a full-consistent empirical model for the devices used in this work. As shown in Appendix B, Figure 1, Γ and Φ are linear functions of V_{DS}, with slopes equal to 0.25 and 0.75, respectively and empirically determined intercepts γ and ϕ. Rearrangement of equations 11 and 12 hence leads to a predictive model for V_{bulk} in both configurations: CSCG, equation 13, and CDGS, equation 14.

$$V_{bulk} = \gamma+ \frac{1}{4} \, V_{DS}+ \frac{1}{2} \, V_{GS} \qquad\qquad \text{CSCG} \qquad\qquad (13)$$

$$V_{bulk} = \phi+ \frac{3}{4} \, V_{DS}+ \frac{1}{2} \, V_{GD} \qquad\qquad \text{CDGS} \qquad\qquad (14)$$
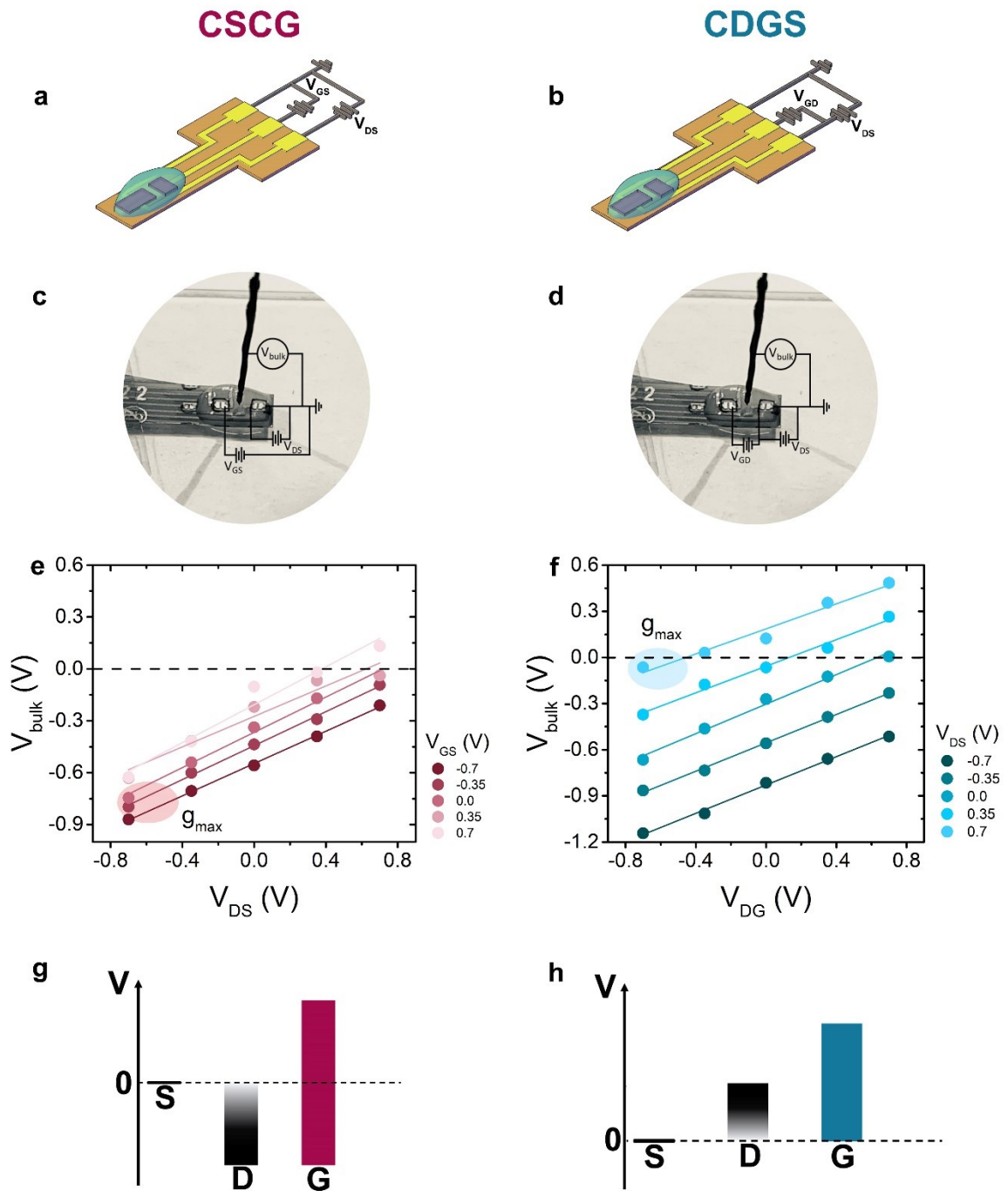
Figure 16. a) Connection layout of the common-source/common-ground (CSCG) EGOT, b) Connection layout of the common-drain/grounded source (CDGS) EGOT, c) Photograph and circuit schematics of the V_{bulk} recording setup for CSCG EGOT, d) Photograph and circuit schematics of the V_{bulk} recording setup for CDGS EGOT, e) Scatter plot showing the dependence of V_{bulk} on V_{GS} in CSCG configuration, with highlighted maximum transconductance regime, showing strong negative V_{bulk} values at maximum transconductance, f) Scatter plot showing the dependence of V_{bulk} on V_{GD} in CDGS configuration, with highlighted maximum transconductance regime, showing null V_{bulk} at maximum transconductance, g) Schematic representation of the spans of the driving voltages in CSCG configuration, h) Schematic representation of the spans of the driving voltages in CDGS configuration.
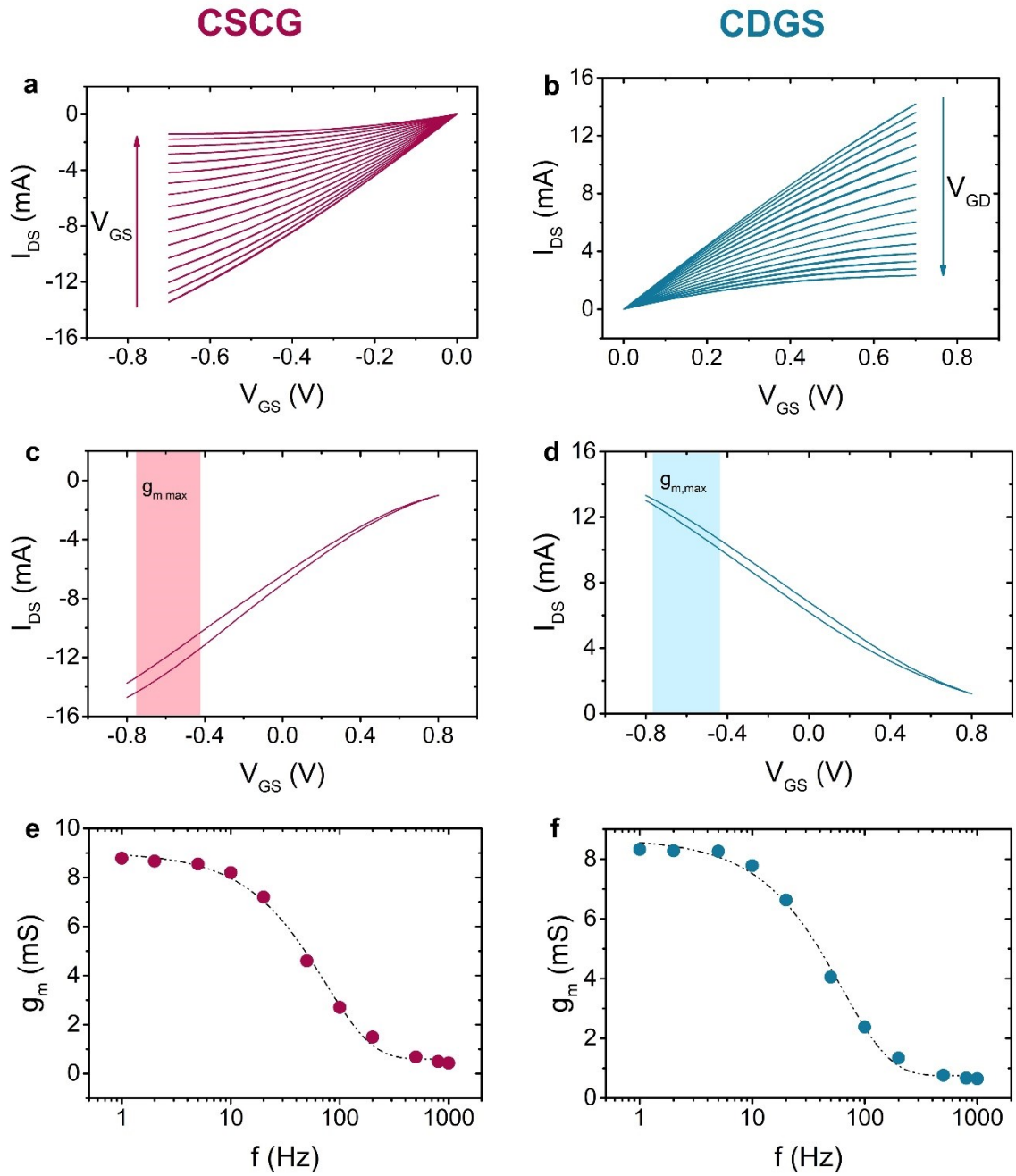
CSCG

CDGS

Figure 17. a) Output characteristics recorded in CSCG configuration scanning V_{DS} from −0.7 to 0.0 V at fixed V_{GS} values ranging from −0.8 to 0.8 V. Arrow indicates increasing V_{GS}, b) Output characteristics recorded in CDGS configuration scanning V_{DS} from 0.0 to 0.7 V at fixed V_{GD} values ranging from −0.8 to 0.8 V. Arrow indicates increasing V_{GD} , c) Transfer characteristic recorded in CSCG configuration scanning V_{GS} from −0.8 to 0.8 V at V_{DS} = −0.7 V. The maximum transconductance regime is highlighted, d) Transfer characteristic recorded in CDGS configuration scanning V_{GD} from −0.8 to 0.8 V at V_{DS} = 0.7 V. The maximum transconductance regime is highlighted, e) g_m versus frequency profile in CSCG configuration recorded by applying a sinusoidal wave to the gate electrode with amplitude equal to 200 mV_{pp} by keeping V_{DS} equal to -0.7 V, f) g_m versus frequency profile in CDGS configuration recorded by applying a sinusoidal wave to the gate electrode with amplitude equal to 200 mV_{pp} by keeping V_{DS} equal to 0.7 V.

As said, γ and φ are peculiar to the chosen device architecture and connection layout and are equal to 368 mV ± 4mV and -312 mV ± 8 mV respectively. Accordingly, when our devices are operated in CSCG configuration, V_{bulk} = 0 when $1/4V_{DS}$ +$1/2$ V_{GS}= -γ, i.e., at positive V_{GS} values, which means that the channel is completely dedoped and the transconductance reaches its minimum value. Conversely, in CDGS configuration it is possible to achieve V_{bulk} = 0 when $3/4V_{DS}$ +$1/2$ V_{GD}= -φ, i.e., when V_{GD} is negative, the channel is in its partially doped state and the transistor transconductance is maximum, as shown in **Figure 16 e** and **f**.

In **Figure 16 g** and **h** the schematic representation of voltages spans is depicted. The CDGS configuration proved to be a suitable structure for establishing a reliable environment for electrophysiological measurements. In both configurations, standard transistor characterisation is performed by collecting I-V characteristics and determining the bandwidth profile, **Figure 17**. In particular, it is worth noticing how, in terms of absolute values, both output **Figure 17 a** and **b**, and transfer, **Figure 17 c** and **d**, characteristics are substantially independent of the adopted connection scheme. Nevertheless, in the proposed CDGS configuration, the I–V curves span the first and second quadrants (I_{DS} > 0 A) of the I versus V Cartesian plane, **Figure 17 b** and **d**. Conversely, in the usual CSCG configuration, they span the third and fourth quadrants (I_{DS} < 0 A), **Figure 17 a** and **c**. As expected for PEDOT:PSS channels, transfer characteristics exhibit depletion behaviour and nonlinear dependence of transconductance, g_m, on gate voltage, with g_m saturating to its maximum value at negative V_{GS} or V_{GD}, for CSCG or CDGS, respectively.

The maximum gm regime is highlighted in **Figure 17 c** and **d**. Importantly, in order to be able to transduce and amplify the same frequency-dependent electrophysiological event, the bandwidth profile is estimated. It is worth noticing that the connection layout does not affect the frequency response of the devices, as shown in **Figure 17 e** and **f**.

6.1.2 In vivo comparison of EGOT configurations

EGOTs were acutely implanted in the barrel cortex of rats, **Figure 18 a**, and performances of both architectures were assessed in vivo, **Figure 18 b,** as described in Section 4.10. Anesthetized rats were positioned in a stereotaxic apparatus and their sensorimotor cortex (barrel cortex representation of whiskers) was exposed by traditional neurosurgery procedure. **Figure 18 c** reports an overlay of typical *in vivo* transfer characteristics, showing excellent agreement with the respective benchside I–V responses, cf., **Figure 17 c** and **d**. In order to compare their recording capabilities, the two configurations were benchmarked against a well-defined potential modulation in the barrel cortex, the so-called somatosensory evoked potential (SEP) [36,37]. Such modulations were elicited by single-pulse mechanical stimulation of the rat whiskers and *in situ* amplified electrophysiological activity was acquired as I_{DS} versus time. Evidence of highly comparable in vivo performances of the two configurations is shown as mean I_{DS} profiles, **Figure 18 d**, and quantified in terms of SNR, **Figure 18 e**.

For all the tested frequency bands, the ratio between the SNR of the CSCG EGOT and the SNR of the CDGS EGOT lays around value 1, hinting at identical amplification capabilities. The only noticeable difference is represented by the fact that the phases of the two I_{DS} responses to the same electric field modulation are reversed, **Figure 18 d**, as implied by the opposite V_{DS} sign. Focusing on the features of the neural activity collected with CDGS EGOTs, **Figure 19** reports an overview of the evoked signal acquired with the proposed architecture. As shown in **Figure 19 a**, the mean I_{DS} profile depletes in roughly 75 ms after the stimulation onset and is characterized by two major peaks (a first negative peak and an almost equal amplitude positive peak), followed by a negative rebound.

By looking at the I_{DS} spectrogram averaged over trials, **Figure 19 b**, it is possible to appreciate the frequency content of such oscillation which exhibits relevant power up to 100 Hz. The features defining the event related
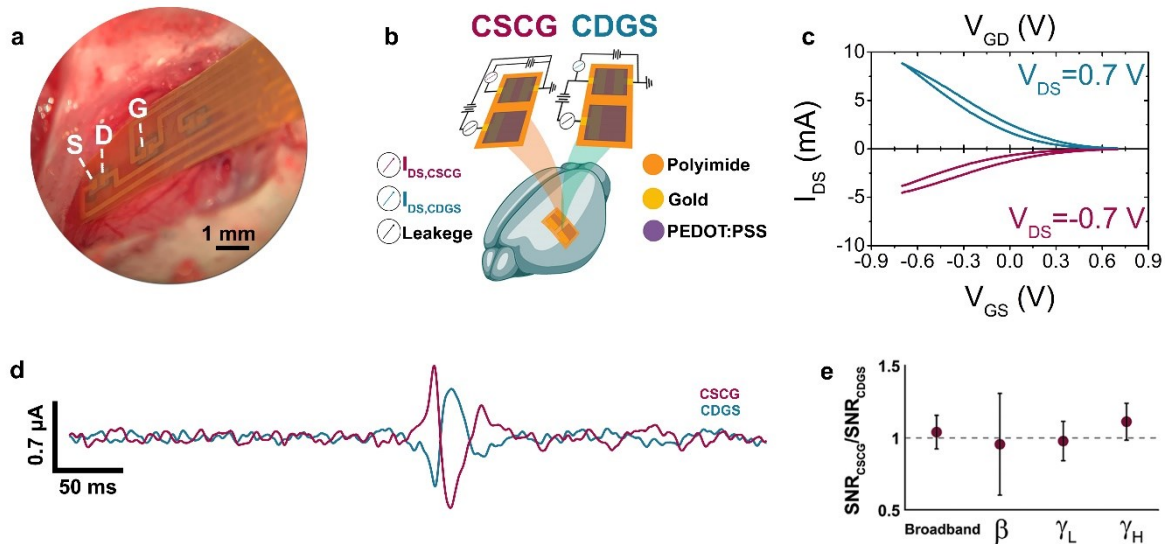
Figure 18. a) Photographic image of the device implanted over the rat barrel cortex. Labels identify source (S), drain (D), and gate (G) electrodes, b) Connection layouts of CSCG and CDGS EGOT configurations for in vivo recordings, c) In vivo transfer characteristics of both EGOT architectures (CSCG in dark pink and CDGS in green water), d) Averaged trials (n = 100) of the somatosensory evoked response collected with the two different configurations from the same cortical position (Rat 1). Data are time locked to the start of the whisker stimulation (t = 0 s) and band-pass filtered between 15 and 150 Hz. e) Scatter plot of the ratio between the SNR of the CSCG EGOT and the SNR of the CDGS EGOT (mean ± propagated SEM) calculated in all frequency bands (broadband 15–150 Hz; beta β 15–30 Hz; low-gamma γL 30–80 Hz; high-gamma γH 80–150 Hz).
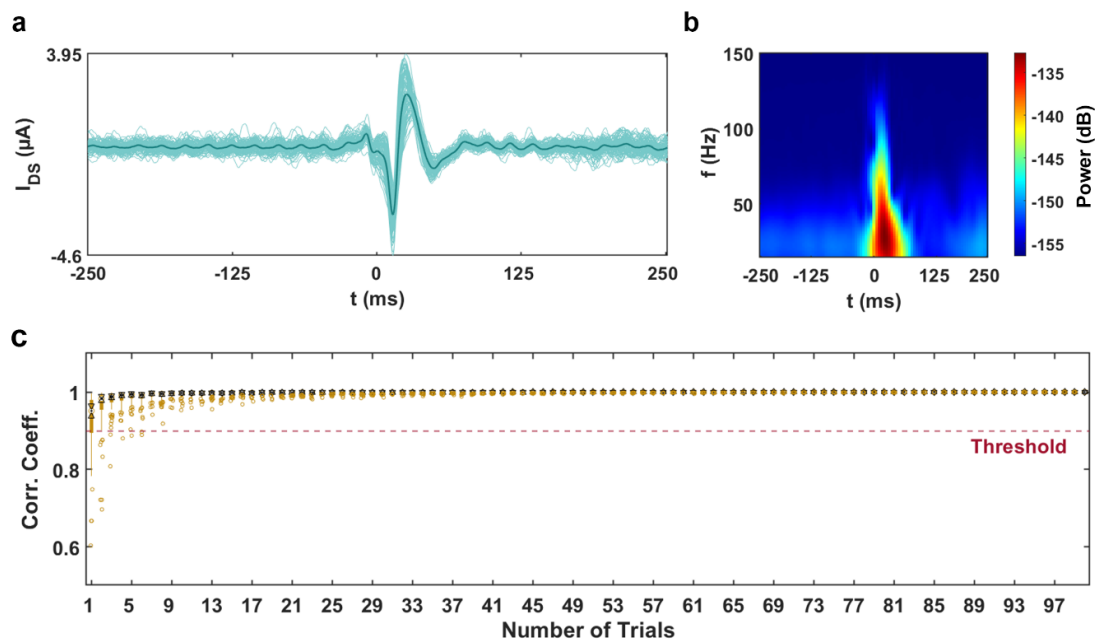
Figure 19. a) Average (dark green, n = 100, Rat 2, Position 2) and single trials (light green) of the somatosensory evoked responses, time locked to the start of the whisker stimulation (t = 0 s) measured as I_{DS} versus time. Data are band-pass filtered between 15 and 150 Hz. b) Average (n = 100, Rat 2, Position 2) spectrogram of I_{DS}. c) Box-plots (in yellow) of the correlation coefficient values computed between I_{DS} averaged over 100 randomly selected trial groups and I_{DS} averaged over all trials (n = 100), iterated increasing group numerosity by steps of 1, reported versus group numerosity. Dashed red line indicates the selected threshold to achieve a reliable estimation of the somatosensory evoked response. Here minimum trial number to obtain a correlation higher than 90% is 1.
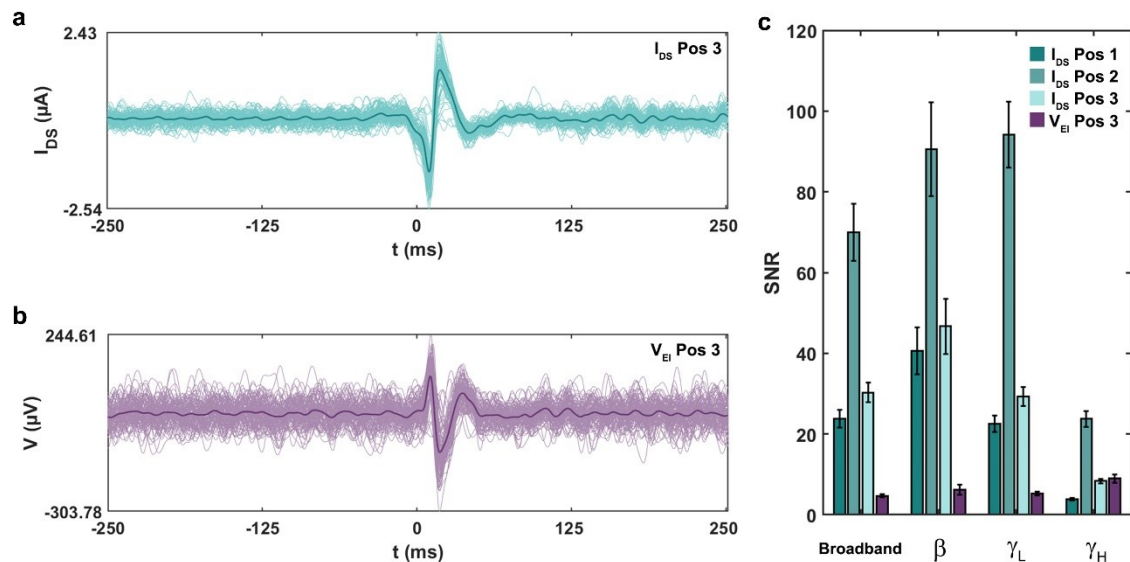
Figure 20. a) Average (dark green, n = 100, Rat 3, Position 3) and single trials (light green) of the somatosensory evoked responses, time locked to the start of the whisker stimulation (t = 0 s) measured as I_{DS} versus time. Data are band-pass filtered between 15 and 150 Hz. b) Average (dark purple, n = 100, Rat 2, Position 3) and single trials (light purple) of the somatosensory evoked responses, time locked to the start of the whisker stimulation (t = 0 s) measured as voltage versus time. Data are band-pass filtered between 15 and 150 Hz. c) Bar plot of the SNR values (mean ± SEM) calculated in all frequency bands (broadband 15–150 Hz; beta β 15–30 Hz; low-gamma γL 30–80 Hz; high-gamma γH 80–150 Hz) for all the recording sessions.

current oscillations are extremely consistent in different positions over the rat cortex as well as in different animals. This consistency is quantitatively investigated by computing the correlation between the average of trial subsets and the average of all trials. The aim is the determination of the minimum number of trials required to obtain a robust estimate of the somatosensory evoked response, **Figure 19**. Using CDGS EGOTs, a single trial is sufficient to obtain a reliable representation (i.e., a correlation greater than 90%) of the average evoked response. The in vivo amplification capability of the proposed architecture was assessed by comparing the recorded I_{DS} traces with voltage traces, V_{EI}, collected with a standard electrophysiological apparatus. In the latter configuration, the gate terminal is used as a passive recording electrode, which collects SEPs as voltage fluctuations with respect to a reference point (a grounded small screw placed on the skull). **Figure 20 a** and **b**, shows current and voltage traces for the same rat in the same position. Noticeably, a phase reversal is observed between voltage and current traces. In particular, the two peaks (first

positive, then negative) of the potential of the gate electrode, when used as a passive recording site, **Figure 20 b**, and the two opposite peaks in EGOT I_{DS}, **Figure 20 a**, is due to the fact that a positive shift of the gate voltage with respect to the ground (i.e., the source) results in a less negative V_{GD}. In our configuration, less negative V_{GD} corresponds to a lower doping level, providing a lower positive current, **Figure 17 b** and **Figure 18 c**, and, hence, a negative I_{DS} peak. This phase reversal is not observed in CSCG configuration, **Figure18 d**, where a lower doping level corresponds to a lower negative current, **Figure 17 c** and **Figure 18 c**, and to a positive I_{DS} peak. The amplitude of EGOT-transduced signals is consistent with the EGOT working principle, since a voltage variation of 100 µV gives rise to a current variation of 1 µA, coherently with the g_m values in the 10 mS range, as in the I–V characteristics of such devices.

A direct comparison between the performances of electrode (i.e., voltage) and CDGS EGOT (i.e., current) recordings is given in terms of the SNR, as described in Section 4. **Figure 20 c**, shows SNRs of I_{DS} and V_{EI} recordings for the whole investigated bandwidth (15–150 Hz) and for individual frequency bands (β 15–30 Hz, γ_{Low} 30–80 Hz and γ_{High} 80–150 Hz). It is evident the marked gain in SNR yielded by the CDGS EGOT architecture compared to the passive electrode. Due to the well-known gain/bandwidth trade-off of EGOTs[8], this gain scales inversely with the increase of frequency. From the correlation analysis of the voltage traces it is possible to notice that the minimum trial number to obtain a reliable estimate of the SEP increases to 3 when recording with passive electrodes (Appendix B, Figure 2).

This last finding confirms that, to make full use of the advantages provided by EGOTs as electrophysiological transducers, one should adopt recording methods that directly use channel current as readout rather than forcing EGOT architectures into classical electrophysiology systems at the price of losing part of their benefits. The herein presented common-drain/grounded-source EGOT overcomes a critical problem of translational organic bioelectronics, namely the application of a potentially harmful bias to tissues

and bodily fluids. Earlier attempts to overcome this issue in the classical common-source/common-ground configuration focused on achieving maximum transconductance at $V_{GS} = 0$ V, thereby posing strict fabrication constraints[38]. In the common drain/grounded-source layout, driving voltages can be adjusted to achieve maximum transconductance in order to cope with various device geometries and application scenarios, without compromising the safety of EGOT operation in the brain and its recording capabilities. Furthermore, high SNR and event recognition at the single-trial level to clinical scenarios are emphasized, both of which are critical features in the effective deployment of brain-machine interfaces (BMIs), which are exposed to a continuous flow of different neural information that must be resolved in real time.

6.2 The MuSTA: Multi-Species Transistor Array

The MuSTA (Multi-Species Transistor Array) is a polyimide-based thin-film grid for electrocorticography intended for translation from murine models to humans. The polyimide-based thin-film integrates a 100 nm-thick gold metallization layer featuring three main blocks: a recording area featuring organic transistor, a long neck of running tracks and two different connection pads the zero-insertion-force (ZIF) pads and the soldering pads, **Figure 21**.
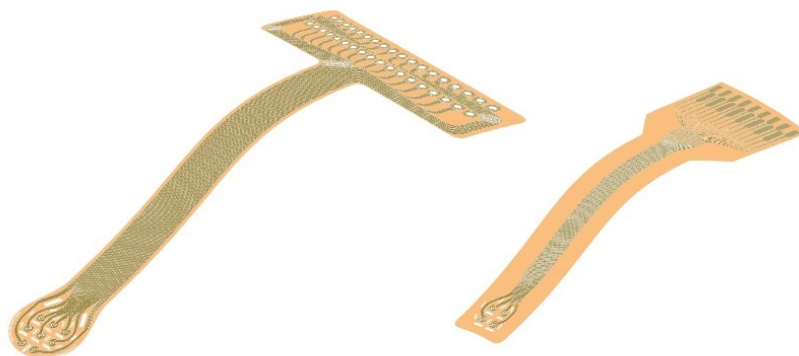
Figure 21. Schematics of the MuSTA device. On the left MuSTA device featuring soldering pads, on the right MuSTA featuring ZIF connectors pads.

MuSTAs are inspired by the necessity to bring electrolyte-gated organic transistor technology on par with electrode-based micro-electrocorticography arrays. Section 6.1.2 emphasizes the significant benefits that EGOT-based technology can provide to neuroelectronics, namely greater SNR and event detection at the single trail level, and the requirement to record current rather than voltage to fully exploit all the benefits offered by EGOTs after careful optimization of all the determining factors for gain and bandwidth [7,9,38,39].

MuSTAs are built with the concept of monitoring brain activity with improved spatial and spectral resolution, **Figure 22.** To ensure prompt translatability to humans in clinical scenarios, they are fabricated with standard clean room fabrication processing in collaboration with the Department of Microsystem Engineering (IMTEK) of the University of Freiburg, as described in Section 4.5. Bridging MEMS processing with the field of neural interfaces has drastically altered people's perceptions of brain implants. The ability to print with extremely fine resolutions - down to a few micrometers or even nanometers - utilizing micromachining processes enables a huge improvement in recording density.
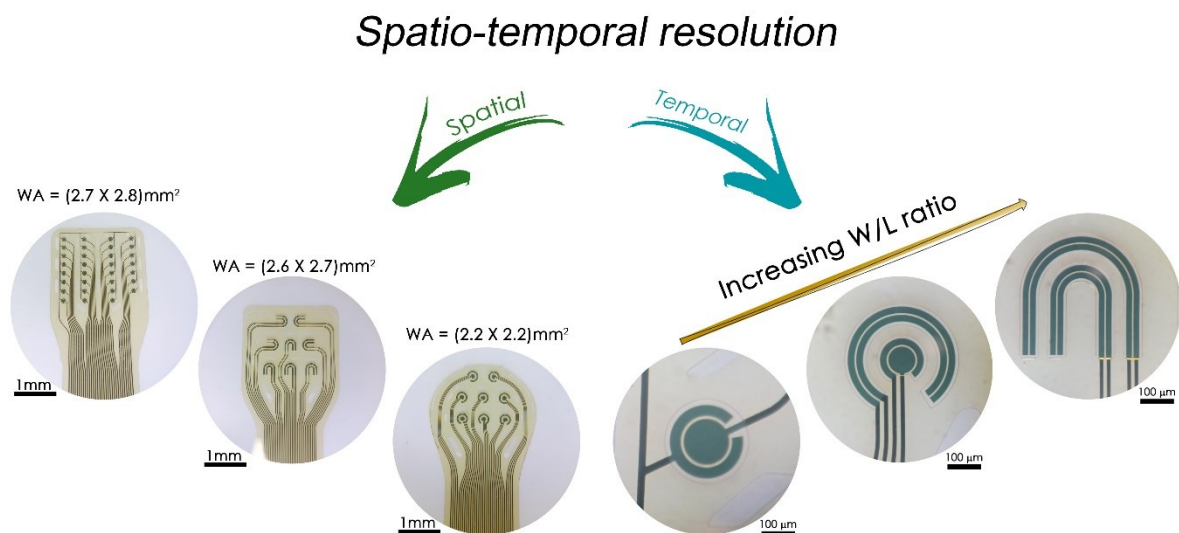
Figure 22. Spatio-temporal resolution with MuSTA. The spatial resolution is gained by increasing the number of organic transistors on the array; in the picture, starting from the left top position, from 31 to 16 transistors can be implemented on a single epicortical probe. Changing the device geometrical parameters to ensure distinct frequency behaviour can improve temporal resolution.

Electrodes have downsized (to as small as 5 μm in diameter), and the pitch between them has shrunk, resulting in high-density microelectrode arrays (MEAs). High-density interfaces are critical for advancement in fundamental and translational neuroscientific research, as well as in the field of brain-machine interfaces (BMIs), because they allow for cell-size resolution in sampling neuronal volumes [40,41]. In terms of spatial resolution, the arrays are designed with working areas (WAs), i.e., the area covered by all the electrodes on the array, ranging from 1.3 x 1.3 mm^2 to 2.7x2.8 mm^2 as the number of electrodes pair increases, from 8 to 31 electrodes couple.

Meanwhile, in terms of spectral or temporal resolution, the electrode pairs are designed with increasing aspect ratios (W/L), with channel length remaining constant at 5 μm for all designs, and with different recording site areas, i.e., the effective area occupied by a single organic transistor.
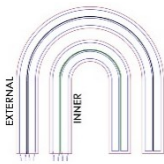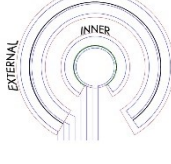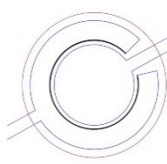
Table 1 shows the recording site area, W/L, and channel width for each electrode geometry, namely circular, u-shape, and concentric. In Appendix C all the specs of the designed arrays are depicted. Shortly, in u-shape and concentric arrays electrode trace width is equal to 25 μm, meanwhile for circular arrays the external electrode trace is 25 μm and inner electrode has a diameter of 100 μm. The distance between two pair of electrodes, in u-shape and concentric arrays, is 60 μm, and the center-to-center distance is 750 μm. For the circular geometry the center-to-center distance is equal to 315 μm.

For all the designed arrays, the connecting tracks have an initial width of 15 μm and clearance of 15 μm close to the electrodes which gradually broaden to a width of 30 μm and clearance of 35 μm along the neck. The pad area is composed of two rows of ZIF pads spaced by 280 μm along the row and soldering pads spaced by 100 μm along the row and 600 μm between rows. Since the first demonstrations of NeuroGrid and Multy-Species Array [42–44], conformability has been linked to the ability to record spike activity from the surface of the brain due to superior electrochemical coupling between electrode and tissue, fundamentally changing research's

view on electrocorticography. For this reason, polyimde is chosen as support layer for our devices, with a total thickness of 10 μm to ensure conformability to the brain[43]. Moreover the array WAs are engineered on highly fenestrated substrates which allows to strongly decrease their bending stiffness, effectively ensuring their compliance to the brain tissue [43,45,46]. Unlike conventional organic transistor fabrication, in which the mixed ionic-electronic semiconductor is deposited between the drain and source via spin coating and then patterned via photolithography [7,38,39,47–49], this approach calls for the use of electrodeposition to bridge the drain and source with an organic semiconductive layer, in this case PEDOT/PSS.

This decision is the product of a broader vision. To guarantee electrodeposition for channel closure while fixing a small L, a large W must

Table 1. Electrodes geometrical parameters

Geometry	U-shape	Concentric	Circular
Recording site area	255 μm	410 μm	90 μm
Inner channel width	820 μm	300 μm	300 μm
External channel width	1180 μm	877 μm	-
Inner W/L	164	60	60
External W/L	236	175	-

keep the W/L ratio as high as feasible in order to boost and counterbalance the influence of thickness on electrical properties. As a result, while maintaining a high W/L ratio, d becomes an EGOTs tuning parameter to achieve variable cut-off frequencies and electrical performances. Bearing this in mind, the goal is to create various arrays with systematically varying

shape, to produce devices that operate in different frequency domains on the same matrix.

In an electrophysiological setting, this means that it would be possible to gather a complex signal from a physiological event and to factorize it *in situ* by differential amplification of its constitutive frequency component, basing on individual transistor figures of merit. This could also be advantageous for post-processing raw signals, i.e., if a specific event is locked at certain frequency band , it would be possible to process only the data from that specific interval and from a specific device without analysing a broadband signal.

6.2.1 Defining the electrodeposition protocol

All electrodepositions in this section are performed and collected with MuSTA arrays featuring u-shape and concentric geometry using a zero-insertion force (ZIF) Hirose DF30 connector mounted on a printed circuit board (PCB) including the ZIF-Clip® headstage. In order to define a standard electrodeposition protocol, the minimum charge density (J) for ensuring semiconductive channel closure, by bridging drain and source electrodes with a PEDOT/PSS film, must first be defined.

The area covered by each pair of electrodes is estimated according to the design made in AutoCAD® (Autodesk, California, USA) to compute the amount of charge that must be exchanged for PEDOT/PSS electrodeposition. Starting with a fixed J, $J = q \cdot A^{-1}$, where q is the exchanged charge and A is the electrodeposited area, and an aqueous solution containing 10 mM EDOT and 5 mg mL^{-1} NaPSS in potentiostatic mode, as indicated in Section 4.6.1, $J = 100$ mC cm^{-2} has been the first attempted electrodeposition condition to close the channel, meanwhile $J = 400$ mC cm$^-$

[2] is employed to electrodeposit PEDOT/PSS on the gate electrode, aiming at high gate interfacial capacitance.

Collection of I-V characteristics revealed the absence of current in such channels, indicating that the selected charge density was insufficient to bridge drain and source. After systematic investigation of J values, it has been possible to estimate that the exchange of J = 200 mC cm^{-2} yields coatings of the source and drain electrodes which are thick enough to touch each other across the 5 µm channel. This J value was fixed as the minimum requirement to obtain the semiconductive channel in the designed architectures. This is true both for u-saped and concentric arrays.

Section 4.6.1 describes fine details on the investigate charge densities and on the electrodeposition setup.

6.2.2 MuSTA in vitro characterisation

Organic transistor electrical performances are assessed *in vitro* in PBS 1 M, with MuSTA arrays featuring u-shape and concentric geometry using the same connector used for electrodeposition. I-V acquisition protocol is reported in detail in Section 4.7. Briefly, transfer characteristics are acquired sweeping V_{GS} from – 0.8 to 0.8V by steps of 8mV (scan rate=200mV s^{-1}), while keeping V_{DS} equals to -0.8 V. Output characteristics are acquired by cycling V_{DS} from 0.0V to -0.8V, changing the fixed V_{GS} value at each cycle from -0.8V to 0.8V with steps of 0.2 V.

After electrodeposition the arrays were soaked overnight in MilliQ water to promote PEDOT/PSS water uptake and to eject ions in excess from the electrodeposited film. To the best of our knowledge, the electrodeposition of PEDOT/PSS for channel formation in EGOTs is a novelty, if compared to standard spin-coating and/or printing of PEDOT:PSS formulations [7,8,39]. Given that the deposition technique affects the properties of polymeric
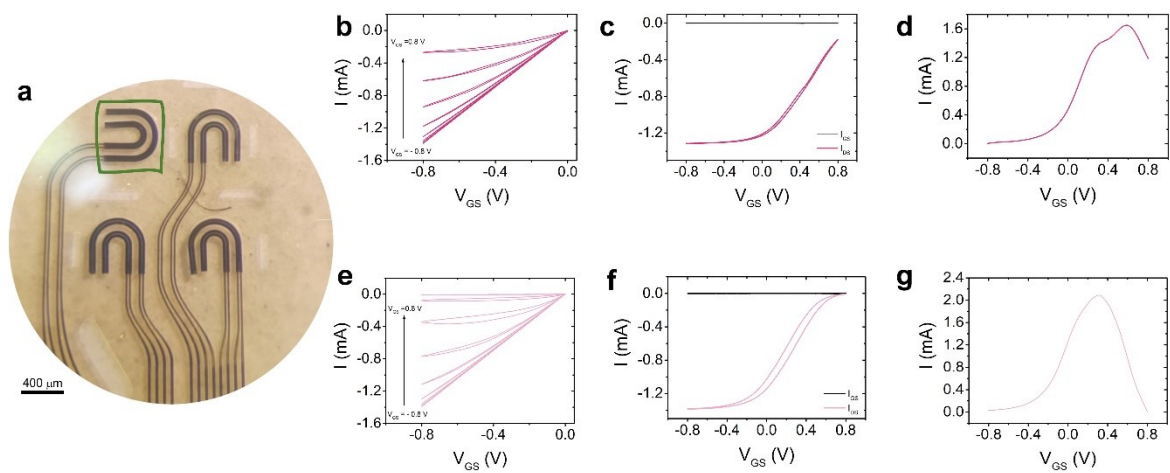
Figure 23. a) Optical microscope image depicting electrodes covered with PEDOT:PSS, green box highlight the four short-circuited electrodes exploited as gate, b) Output characteristics recorded with big channel scanning V_{DS} from −0.8 to 0.0 V at fixed V_{GS} values ranging from −0.8 to 0.8 V, c) Transfer characteristic recorded with big channel scanning V_{GS} from −0.8 to 0.8 V at V_{DS} = −0.8 V, in black is reported I_{GS}, d) g_m versus V_{GS} profile for large u-shape transistor, e) Output characteristics recorded with small channel scanning V_{DS} from 0.0 to 0.8 V at fixed V_{GS} values ranging from −0.8 to 0.8 V, f) Transfer characteristic recorded with small channel scanning V_{GS} from −0.8 to 0.8 V at V_{DS} = −0.8 V, in black is reported I_{GS}, g) g_m versus V_{GS} profile for small u-shape transistor.
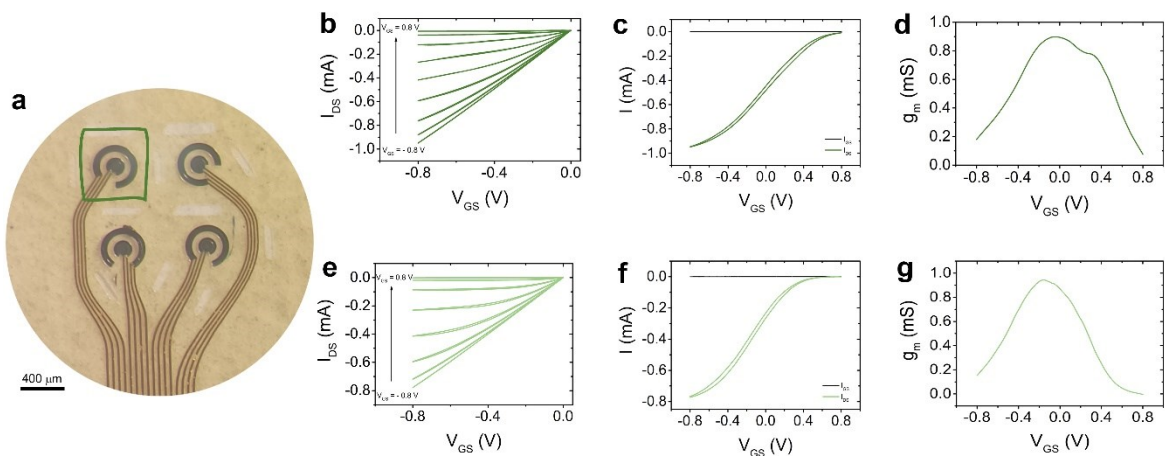
Figure 24. a) Optical microscope image depicting electrodes covered with PEDOT:PSS, green box highlight the four short-circuited electrodes exploited as gate, b) Output characteristics recorded with big channel scanning V_{DS} from −0.8 to 0.0 V at fixed V_{GS} values ranging from −0.8 to 0.8 V, c) Transfer characteristic recorded with big channel scanning V_{GS} from −0.8 to 0.8 V at V_{DS} = −0.8 V, in black is reported I_{GS}, d) g_m versus V_{GS} profile for large concentric transistor, e) Output characteristics recorded with small channel scanning V_{DS} from 0.0 to 0.8 V at fixed V_{GS} values ranging from −0.8 to 0.8 V, f) Transfer characteristic recorded with small channel scanning V_{GS} from −0.8 to 0.8 V at V_{DS} = −0.8 V, in black is reported I_{GS}, g) g_m versus V_{GS} profile for small concentric transistor.

126

semiconductive films and the device performances, as well as the properties of the gate electrode, this section presents the first prototypes of fully-translatable electrodeposited PEDOT/PSS channels and gates on organic transistor arrays fabricated by MEMs techniques.

Figure 23 depicts the U-shape I-V characteristics. Adjacent pairs of short-circuited big (outer) and small (inner) electrodes are used as working electrodes during electrodeposition, achieving two channels for each recording site. I-V curves are collected in such channels using the short-circuited four electrodes in the top left position, in **Figure 23 a**, as the surface-supported co-planar gate electrode.

Figure 23 b and **e** report the output curves of the big (dark pink) and the small (light pink) channel, respectively. With the smallest organic transistor is possible to obtain a full de-doped channel, as mirrored by the transfer curve, **Figure 23 f**. Conversely, the big channel is only partially de-doped at positive V_{GS}, as shown in **Figure 23 c** and **d**.

Interestingly, is possible to obtain higher transconductance value with the smallest drain-source channel if compared to the large one, as reported in **Figure 23 d** and **g**, due to the aforementioned non-linear contribution of W/L to transconductance demonstrated in interdigitated layouts with small channels [7].

The very same experimental approach has been used for the characterization of the concentric arrays, whose I-V characteristics are reported in **Figure 24**. In this case, the short-circuited four electrodes of top left position, **Figure 24 a**, have been used as gate.

In this configuration, it is possible to achieve complete de-doping for both small and big channels, **Figure 24 b**,**c**,**e**, and **f**, although the larger ones (dark green) can achieve a slightly greater ON/OFF ratio, as a consequence of the lower resistance in the fully doped state.

Transconductances, **Figure 24 d** and **g**, reach same values albeit at different $V_{GS,gm\ max}$. In particular, $V_{GS,gm\ max} = -160$ mV for the small couple and -50 mV for the bigger one.

A direct comparison between u-shaped and concentric geometry explicitates the impact of W/L on EGOT performances, both on transfer characteristics **Figure 25 a** and **c**, and on transconductance profiles, **Figure 25 b** and **d**.
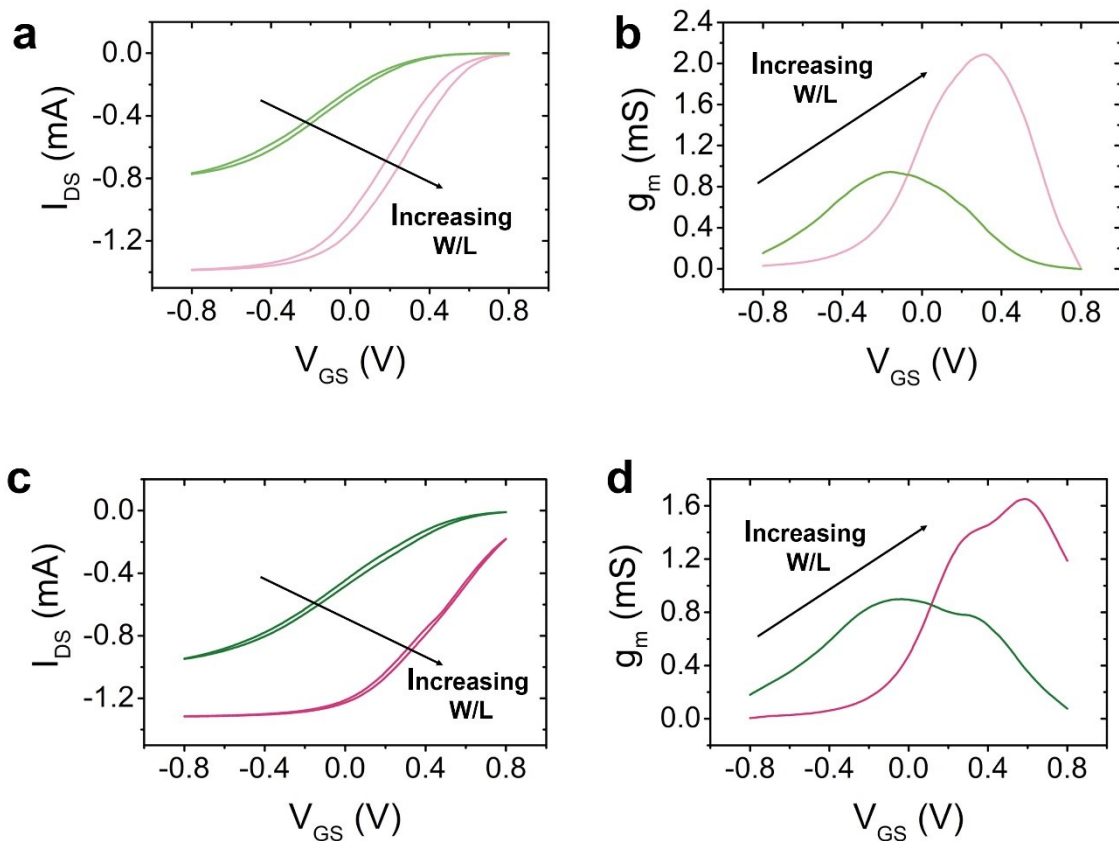
Figure 25. a) I-V transfer curve acquired with small channels, u-shape (light pink line), concentric (light green line). Arrow indicating the direction of increasing aspect ratio, b) g_m versus V_{GS} profile for small transistor, u-shape (light pink line), concentric, (light green line). Arrow indicating the direction of increasing aspect ratio, c) I-V transfer curve acquired with big channels, u-shape (dark pink line), concentric, (dark green line). Arrow indicating the direction of increasing aspect ratio, d) g_m versus V_{GS} profile for large transistor, u-shape (dark pink line), concentric, (dark green line). Arrow indicating the direction of increasing aspect ratio.

The current modulation and the maximum transconductance value are higher in u-shaped arrays with respect to concentric ones. This is not surprising [4,50,51], since channels in u-shaped arrays (both small and big) exhibit higher W/L values with respect to their concentric counterparts.
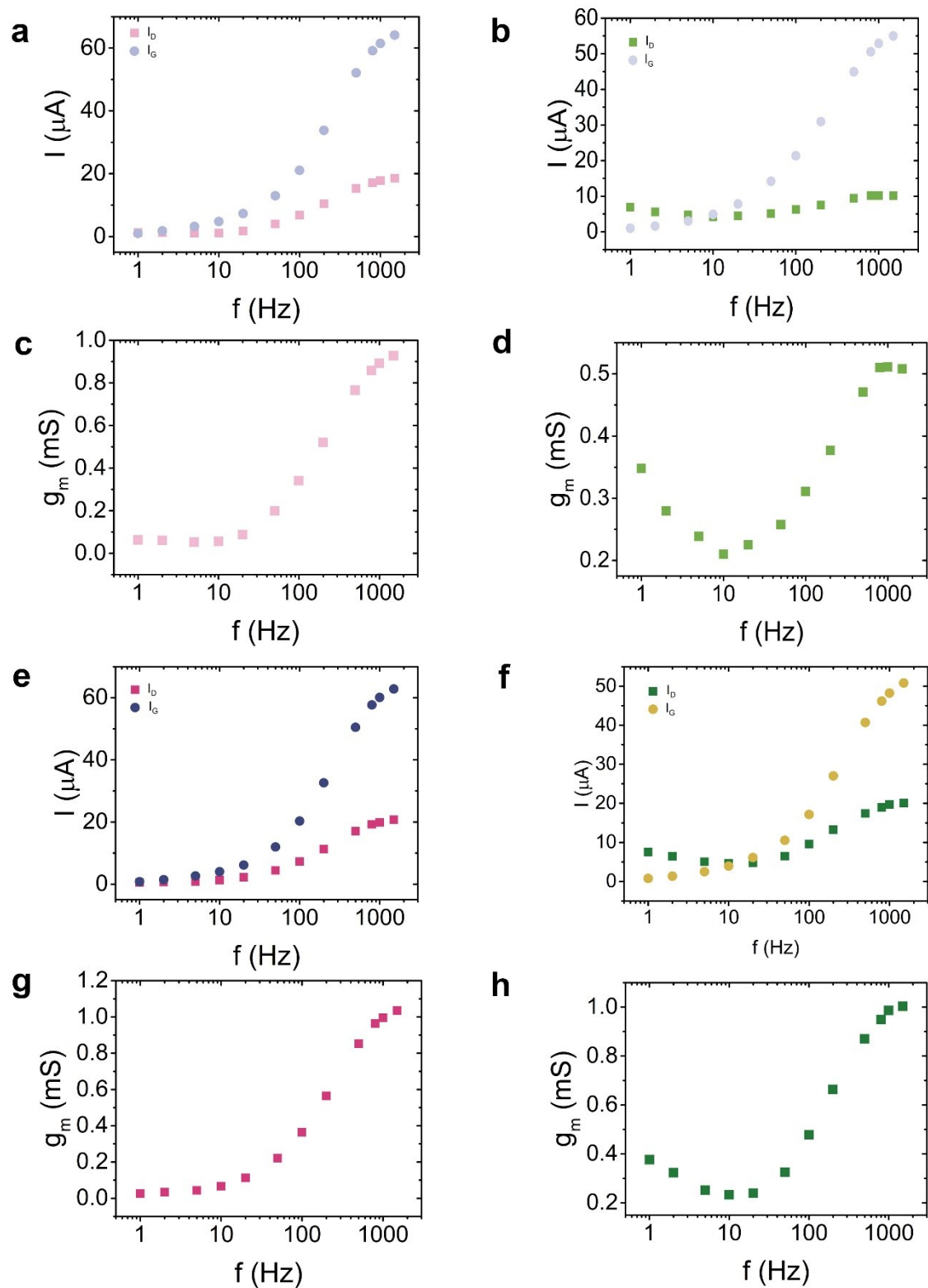
Figure 26. a) I_G (light purple dots) and I_D (light pink squares) versus frequency response from small u-shape transistor, b) I_G (light grey dots) and I_D (light green squares) versus frequency response from small concentric transistor, c) transconductance versus frequency profile from small u-shape transistor, d) transconductance versus frequency profile for small concentric transistor, e) I_G (dark purple dots) and I_D (dark pink squares) versus frequency response from large u-shape transistor, f) I_G (yellow dots) and I_D (dark green squares) versus frequency response from large concentric transistor, g) transconductance versus frequency profile for large u-shape transistor h) transconductance versus frequency profile for large concentric transistor.

Moreover, is possible to observe a shift of $V_{GS,gm\,max}$ at increasing W/L, which reflects the different dependence of I_{DS} modulation upon to V_{GS} sweep.

Besides these, rather trivial, effects on transconductance values, it is important to notice how, in the u-shaped geometry, $V_{GS,gm\,max}$ is positively shifted, hinting to significantly more difficult ion de-doping, with respect to concentric geometry. It is possible to envision various explanations for these positive shifts, which may involve the geometrical dependence of the electric field density, but further investigations are needed in this regard.

Aside from DC characterisation, miniaturized EGOTs are also evaluated concerning AC behaviour. An additional bathing electrode is used as signal source, injecting sinusoidal waves with peak-to-peak amplitude equal to 20 mV in 1 M PBS, and keeping DC biases equal to 0 V at the gate and to -0.7 V at the drain. This mimics the operational scenario of a signal transduction experiment, and both I_G and I_D current are measured, determining I_G, I_D and transconductance vs frequency responses, as described in Section 4.8. The frequency-related response of these devices, showing high-pass behaviour, is shown in **Figure 26** (left colon u-shape devices and right column concentric devices). To the best of our knowledge, there is no evidence in the literature about organic transistors with high-pass behaviour. This unusual response could be attributed to a direct influence of capacitive displacement current at the gate (which increases with frequency) on the recorded current at the drain. This clearly induces a waterfall effect on the trend of transconductance versus frequency. Surprisingly, at high frequencies, I_G is always greater than I_D current, as shown in **Figure 26 a**,**b**,**e** and **f**. This dominance of I_G at high frequencies is due to the small physical dimension of the channel, which yields low I_{DS}, even when the channel is in its ON-state.

This current is usually orders of magnitudes higher than the displacement current which can be recorded at the gate electrode (I_G) in standard PEDOT:PSS organic transistors. As a result, the current at the drain electrode (our observable) is frequently attributed only to the current between source and drain (I_{DS}). For sake of precision, it must be noticed that $I_D \approx I_{DS} + I_{GD}/2$ [33]. If

this is not a problem at the steady state, where I_{GD} approaches 0 since it is purely capacitive and depends on the voltage variation rate, this becomes prominent at high frequencies, especially if I_{DS} is low.

Simplistically referring to the purely capacitive model of the electrical double-layer, $I_G = -(I_{GS} + I_{GD}) = C*(dV_G/dt)$. A frequency increase results in higher voltage variation rates and, hence, in higher currents. This prompts the way for novel strategies of EGOT-based BMIs, which may take advantage of usually neglected parasitic aspects of EGOT working principle to widen their bandwidth. It is envisionable to couple miniaturized EGOTs with large ones (as those presented in section 6.1) to achieve differential responses to different frequency bands and, subsequently, to different types of brain activity, on the same BMIs thereby retaining the most important feature of EGOTs current recording with respect to voltage ones, namely impedance adaptation.

In conclusion, a new generation of ultra-conformable ECoG arrays that exploit OMIEC-based transistors rather than electrodes (from MEA to MTA-Multi-Transistor Array), entirely fabricated by MEMS technologies, is presented in this work. Semiconductive channels are obtained by electrodepositing PEDOT/PSS directly on the electrodes without using printing techniques, sacrificial layers or layer-by-layer protocols. Furthermore, due to arrays geometrical constraints, is possible to observe high pass behaviour exploiting capacitive phenomena. Further investigation will be carried out to verify if this entirely peculiar response is suitable to *in vivo* and even clinical scenarios.

6.3 Organic electronic platform for real-time signal sorting

The brain is continuously filtering away irrelevant information while incorporating relevant data into an internal representation that is used to

forecast what will happen next. In an extreme reductionist sense, this translates into the ability to select and process only relevant frequency-encoded events while ignoring additional chaotic stimuli.

While this task is performed in the brain by algorithms and machinery which have been perfected over eons of evolutionary processes, replicating it with man-made, relatively coarse information technology necessitates power-consuming off-line signal processing strategies and architectures, inevitably posing technological and computational hurdles.

At the same time, as widely reported in this thesis, mankind efforts towards the acquisition of a growing knowledge of brain functioning mechanisms require technological and computational research focused on the development of efficient brain-machine interfaces, with the ultimate goal of establishing a bidirectional communication between the brain and electronic devices[52,53]. As said, organic electronics as emerged as eligible technological platform towards the ambitious goal of knowing, interfacing, and emulating human brain, resulting in the field of Organic Neuroelectronics.

This multi-faceted task involves three main processes that must be performed by BMIs, namely signal transduction, signal amplification and signal sorting.

This section aims at providing a possible solution to the latter process, by presenting an organic flexible architecture for real-time signal sorting, prone to miniaturization and integration in BMIs, and specifically designed to be coupled to EGOT-based *in situ* amplifiers. The proposed technology makes advantage of organic analogues of passive circuit elements, namely organic resistors, and electrolyte-organic capacitors, as building blocks for low- and high-pass passive filters to be coupled to EGOTs. Its signal sorting capabilities, as well as the inherent filtering features of non-miniaturized EGOT, are herein presented and benchmarked against digitally generated model signals of increasing complexity, starting from "monochromatic" sinusoidal waves up to audio traces.

6.3.1 Organic building blocks

The choice of materials to implement the proposed signal sorting architecture is oriented to achieve prompt translatability, using only polyimide substrates, gold leads and poly(3,4-ethylenedioxythiophene) polystyrene sulfonate as organic resistor, as semi-conductive channel, and gate electrode material in EGOTs and as interfacial layer in organic electrolyte capacitors, **Figure 27 a**. Application-specific fabrication details
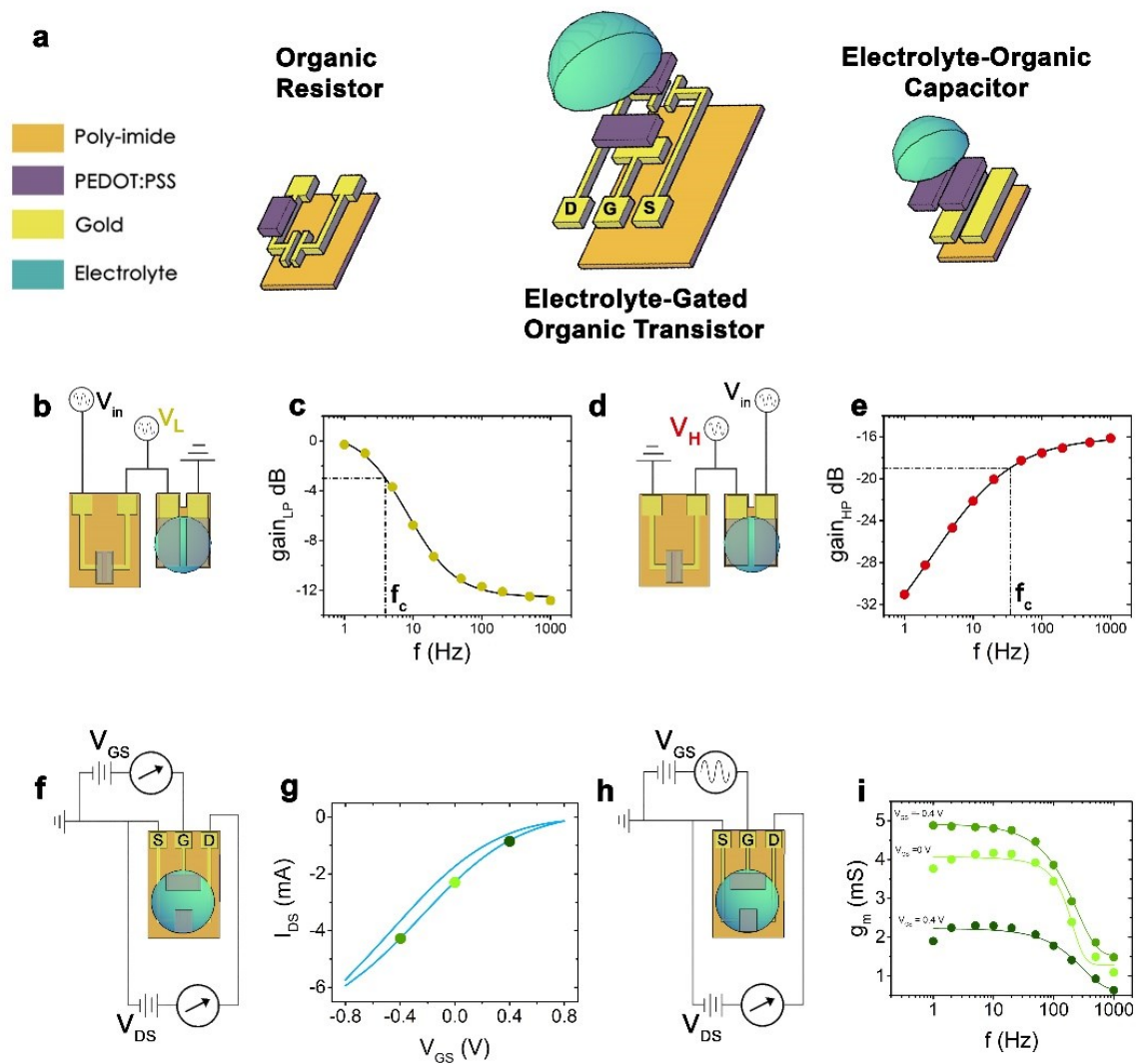
Figure 27. a) Organic building blocks illustrated layer-by-layer, b) Connection layouts of the organic low-pass filter, c) Frequency profile of organic low-pass filter, d) Connection layouts of the organic high-pass filter, e) Frequency profile of organic high-pass filter, f) Connection layouts of EGOT for DC characterisation, g) I–V transfer characteristic recorded by scanning V_{GS} from −0.8 to 0.8 V at V_{DS} = −0.8 V, green dots mirroring the V_{GS} DC-offset exploited for AC characterisation, h) Connection layouts of EGOT for AC characterisation, i) g_m versus frequency profile at different V_{GS} DC-offset.

are provided in Sections 4.3 and 4.4. Passive low-pass, **Figure 27 b**, and high-pass, **Figure 27 d**, filters can be achieved by connecting in series an organic electrolyte capacitor and an organic resistor, sending to ground the capacitor or the resistor, respectively. In this work, organic low-pass filters feature 6Ω resistance and $295\mu F$ capacitor, while organic high-pass filters are built on 14Ω resistance and $220\mu F$. The input voltage, V_{IN}, is provided at the non-grounded terminal of the series and the output voltage - termed V_L for the low-pass filter and V_H for the high-pass one - is collected at the shared node. The frequency profiles of organic filters are evaluated in response to monochromatic sinusoidal V_{IN} waves with peak-to-peak amplitude of 200mV and frequency values ranging from 1Hz to 1kHz.

Figure 27 c and **e** show the responses of low- and high-pass filters, respectively, in the form of Bode plots obtained calculating the gain of low-pass filters, $gain_{LP}$, as 20 x log10(V_L/V_{IN}) and the gain of the high-pass filter, $gain_{HP}$ as 20 x log10(V_H/V_{IN}). Cut-off frequencies, f_c, are estimated as the frequency values for which $gain_{LP}$ = -3dB for low-pass filters and $gain_{HP}$ = -19dB for high-pass ones (i.e., 3 dB less than the maximum $gain_{HP}$ value achieved in the investigated frequency range). The resulting cut-off frequencies are $f_c \approx$ 5Hz for the proposed organic low-pass filters and $f_c \approx$ 30Hz for the high-pass ones, with slopes equal to -6dB/decade and 9dB/decade, respectively.

Interestingly, the use of organic analogues of passive circuit elements causes two main effects with respect to inorganic solid-state counterparts, namely a red-shift of f_c with respect to theoretically expected values (both for high- and low-pass filters) and a substantially negative gain (around -16dB) of the passed high-frequency band in the case of high-pass filters.

Both these effects arise from the fact that, here, an electrolyte compartment is used as a capacitive element in RC filters. If, on the one hand, this enables the engineering of flexible architectures and the exploitation of the high equivalent capacitance values and of the fine tunability of a PEDOT/PSS-

electrolyte interface, on the other it brings into play substantial deviations from ideality, which should be taken into account.

The principal deviation of the proposed electrolyte organic capacitor with respect to an ideal one arise from the fact that the former features a non-negligible resistance in series with the equivalent capacitor of the electrical double layer, CDL. This resistance, termed R_S, is contributed by the electrolyte solution. It is well known that, for standard RC passive filters, equations 15 and 16 hold, for high-pass and low-pass configurations, respectively:

$$\frac{V_{out}}{V_{in}} = \frac{Z_R}{Z_R + Z_C} \approx \frac{R\omega C}{R\omega C + 1} \tag{15}$$

$$\frac{V_{out}}{V_{in}} = \frac{Z_C}{Z_R + Z_C} \approx \frac{1}{R\omega C + 1} \tag{16}$$

where Z_C and Z_R are the impedances of the resistor and of the capacitor, R is the resistance of the resistor, ω is the angular frequency of the input wave, $\omega = 2\pi\nu$, and C is the capacitance of the capacitor.

The attenuation effect of R_S, observed solely in high-pass organic filters, is manifest re-casting equation 15 into equation 17:

$$\frac{V_{out}}{V_{in}} = \frac{R\omega C_{DL}}{(R + R_S)\omega C_{DL} + 1} \tag{17}$$

Despite following the expected trend of a high-pass filter, namely being 0 at null frequency and growing as a power law of ω, the V_{out}/V_{in} ratio approaches $R/(R + R_S)$ at the limit of infinite frequency, which necessarily is minor than one. The entity of this attenuation is indeed a measure of the solution resistance. In the proposed high-pass filter, **Figure 27 d** and **e**, where R=14 Ω, the plateau at -16dB corresponds to $\frac{R}{R + R_S} \approx 0.156$, which leads to an estimate $R_S \approx 75$ Ω, which is coherent with the structure of the proposed capacitive element of organic RC filters.

Conversely, for the low-pass filter, the addition of R_S yields equation 18 from equation 16:

$$\frac{V_{out}}{V_{in}} = \frac{1}{(R+R_S)\omega C_{DL}+1} \tag{18}$$

Which predicts the ideal behaviour of a low-pass filter (i.e., $\frac{V_{out}}{V_{in}} = 1$ at $\omega = 0$

and $\frac{V_{out}}{V_{in}} = 0$ at $\omega = \infty$.

Concerning the red-shift effect observed on the cut-off frequency, f_c, under the assumption that the formalism of passive inorganic filters can be translated to organic ones, it is possible to subtract member by member equations 17 from equation 15 and equation 18 from equation 16. This means that the denominators must be identical. Terming ω_1 the angular frequency of the input wave in a standard passive inorganic filter and ω_2 the angular frequency of the input wave in an organic passive filter, for both architectures, at equal Vout/Vin and assuming $C_{DL}=C$, equation 19 must hold:

$$R\omega_1 C+1= (R+R_S)\omega_2 C_{DL}+1 \xrightarrow{\text{yields}} \omega_2 = \frac{R}{R+R_S}\omega_1$$

Since $\frac{R}{R+R_S}$ is always less than 1, this means that ω_2 will be always lower than ω_1, quantitatively accounting for the red-shift in terms of solution resistance.

In addition to passive filters, the third building block for the proposed basic sorting-platform is the electrolyte-gated organic transistor. EGOTs test pattern are fabricated and characterized, as described in Section 4.4. EGOTs were characterized in common-source/common-ground configuration, **Figure 27 f** , by acquiring transfer curves, **Figure 27 g**, and evaluating their bandwidth by applying sinusoidal waves at different DC offset at the gate electrodes, recording I_{DS}, as depicted in **Figure 27 h** and **i**. These organic transistors show the expected response, with a low-pass behaviour modulated by the device geometrical parameters [7], and a gain set by the Gate DC-offset, which shows also a minor influence on the cutoff frequency in highly de-doped channels (as discussed in section 5), as shown in **Figure 27 i**.
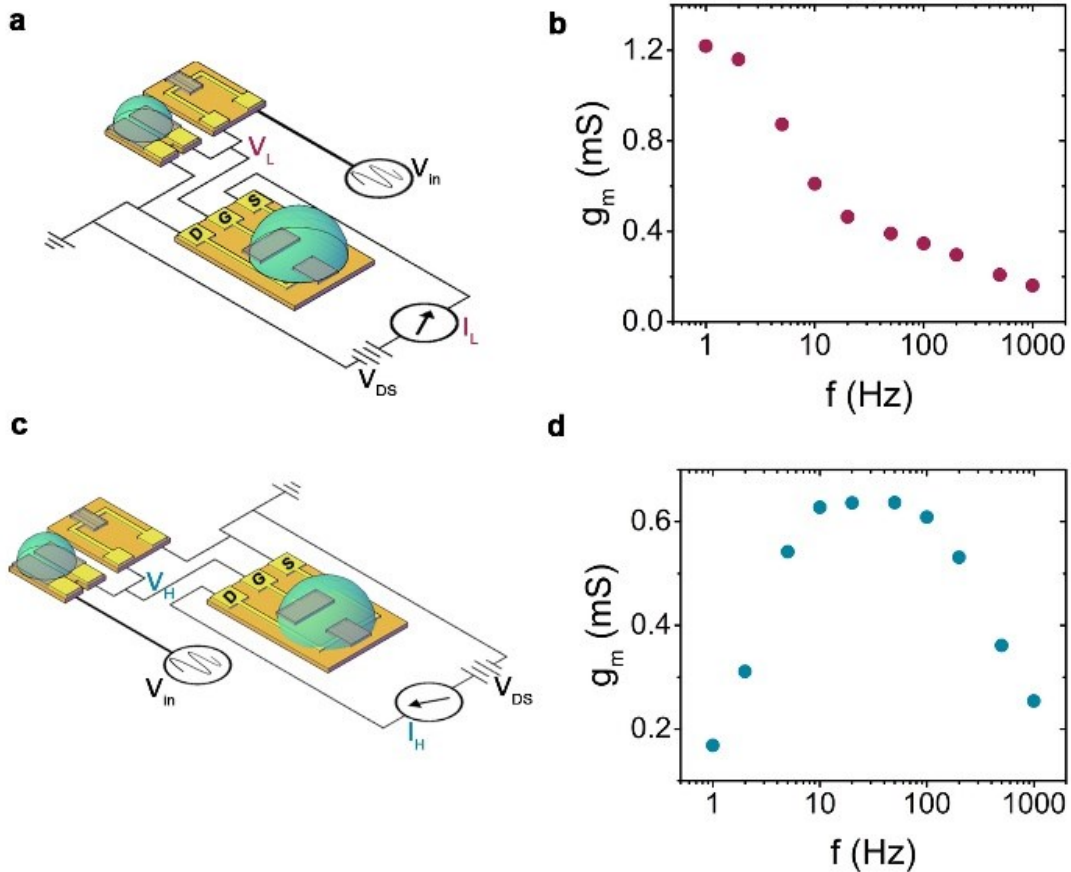
Figure 28. a) Connection layouts of the organic low-pass filter paired with EGOT, b) g_m versus frequency profile for the low band passed EGOT architecture, c) Connection layouts of the organic high-pass filter paired with EGOT, d) g_m versus frequency profile for the high band passed EGOT architecture.

Moreover, coupling EGOTs with organic RC filters it is possible to tighten the bandwidth toward lower frequencies or implement a band pass filter. The first scenario is achieved by coupling the low-pass filter with an organic transistor, **Figure 28 a**, meanwhile the second ones by coupling EGOT with a high pass filter, **Figure 28 c**.

In these configurations the filters output voltages are used as input gate voltages for the EGOTs, keeping V_{DS} constant at – 0.7 V, the cannel currents are measured, I_L and I_H, respectively for the channel current coming from the low filter coupled with EGOT and for the high filter coupled with another EGOT. I_L shows a low-pass filter profile with a cut-off frequency of 5 Hz , as shown in **Figure 28 b**, while I_H exhibits a band-pass profile from 5 Hz to 90 Hz, as depicted in **Figure 28 d**. These two independent architectures can be

paired to foster a platform to sort and amplify a common V_{IN} in two different factorized output signals, as discussed in the next sections.

6.3.3 The sorting platform

In **Figure 29 a**, the sorting platform architecture sketch is reported. A common V_{IN} is driven through the filter inputs and the respective V_{out}, V_L and V_H, are connected to two EGOTs gate electrodes. The channel currents are recorded by fixing V_{DS} equal to -0.7V. To validate our architecture a first characterisation was performed by applying sinusoidal wave with an amplitude of 200 mV$_{pp}$ and frequencies spanning from 1 to 1000 Hz as common input signal. The I_L and I_H currents amplitude are extracted. The amplitude-frequency trends are reported in **Figure 29 c** highlighting the sorting platform frequency-performance, showing a bell-shape for the band-pass branch and a sigmoidal shape for low-pass EGOT. The profile shape is the results of the combination between EGOT's frequency response and filter frequency response. After validating its operation with monochromatic waves, a sweep wave with 200mV$_{pp}$ and frequency interval from 1 to 200 Hz was used as input signal, **Figure 29 b**. The I_L and I_H currents versus time are reported in **Figure 29 b** (bottom panel), highlighting that the designed basic circuit enables to discriminate both in amplitude and in frequency the output responses in real-time. To probe the architecture with a more complex signal, a pre-recorded *in vivo* somatosensory evoked potential (SEP) is digitalized and driven, as described in Section 4.8, as signal input to finely test sorting platform performances in frequency discrimination. In order to be able to translate this circuit with a standard recording probe, implementing more biocompatible BMIs, we want to test its sensitivity in discriminate some of the relevant frequency band, that usually are investigated to properly characterised a SEP:α, β, low γ, γ$_L$, and high γ, γ$_H$, bands [43,58]. In **Figure 29 d** the pre-recorded SEP is shown. Its amplitude was increased to 200mV$_{pp}$ in order to use it as a V_{IN} model signal. I_L and I_H were

recorded as usual by keeping drain-source voltages at -0.7 V. Defining η as the percentage of total power in frequency interval, the analysis of the frequency content in the relevant electrophysiological band was performed, as described in Section 4.11.1.

Briefly, η is evaluated as the ratio between the I_L (I_H) power in a specific frequency band and the I_L (I_H) broadband power, **Figure 29 e**. Even with complex signal, the sorting architecture acts in discriminating event relate at
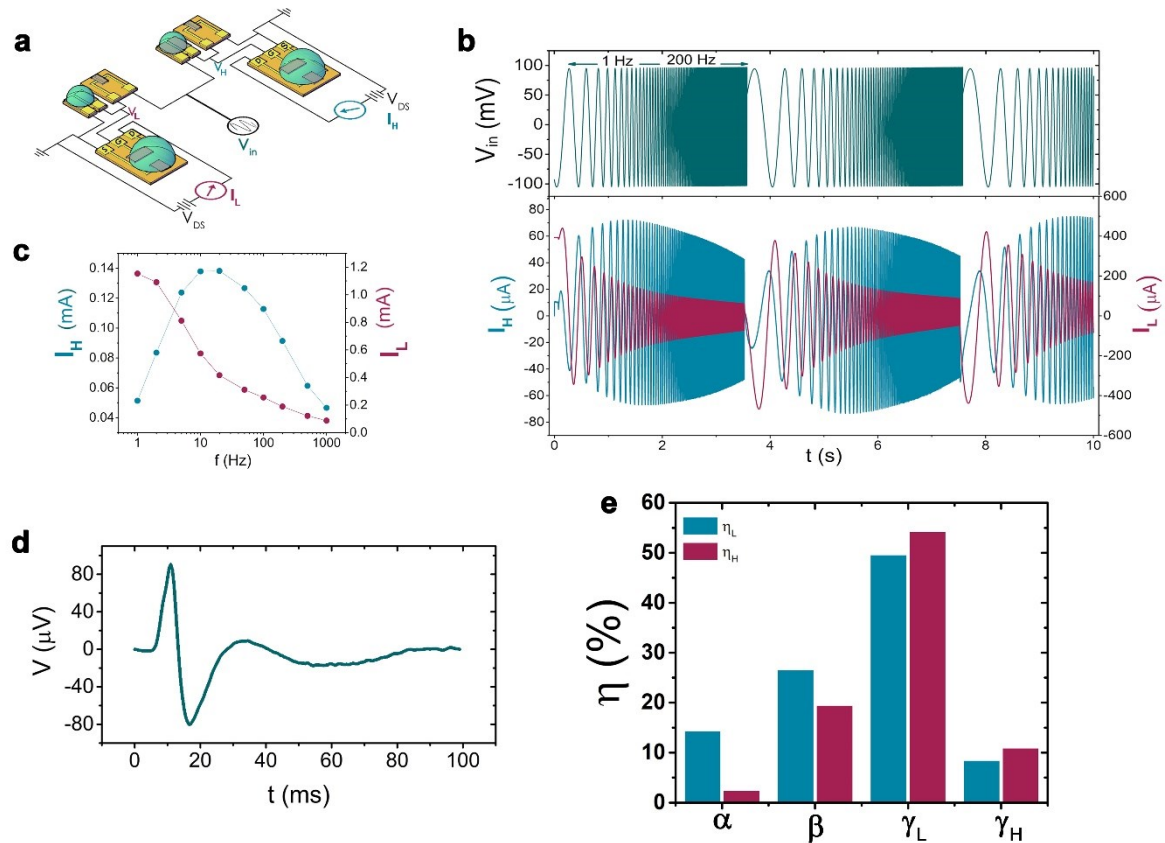
Figure 29. a) Sorting platform connection layouts, b) Sweep wave exploited as V_{IN} for the sorting platform(top panel) and I_H and I_L current output (bottom panel), c) The frequency response of I_H and I_L determined by supplying the sorting platform with a monochromatic sinusoidal wave, d) Pre-recorded in vivo somatosensory evoked potential used as input for the sorting platform, e) percentage of total power in frequency electrophysiological interval alfa α 5-15 Hz; beta β 15–30 Hz; low-gamma γL30–80 Hz; high-gamma γH 80–150 Hz.

different frequency domain. This architecture can low-pass and discriminate with higher gain α and β frequency band, meanwhile the bandpass branch discriminates event with frequency higher than 30 Hz. Since the EGOT implemented in this design has a cut-off frequency of roughly 120 Hz, and

since, at high frequency, the gain of the two branches are comparable, the high-gamma percentage is almost equal.

Moreover, it is possible to exploit the paired RC organic filter as an independent sorting platform as shown in **Figure 30 a**.
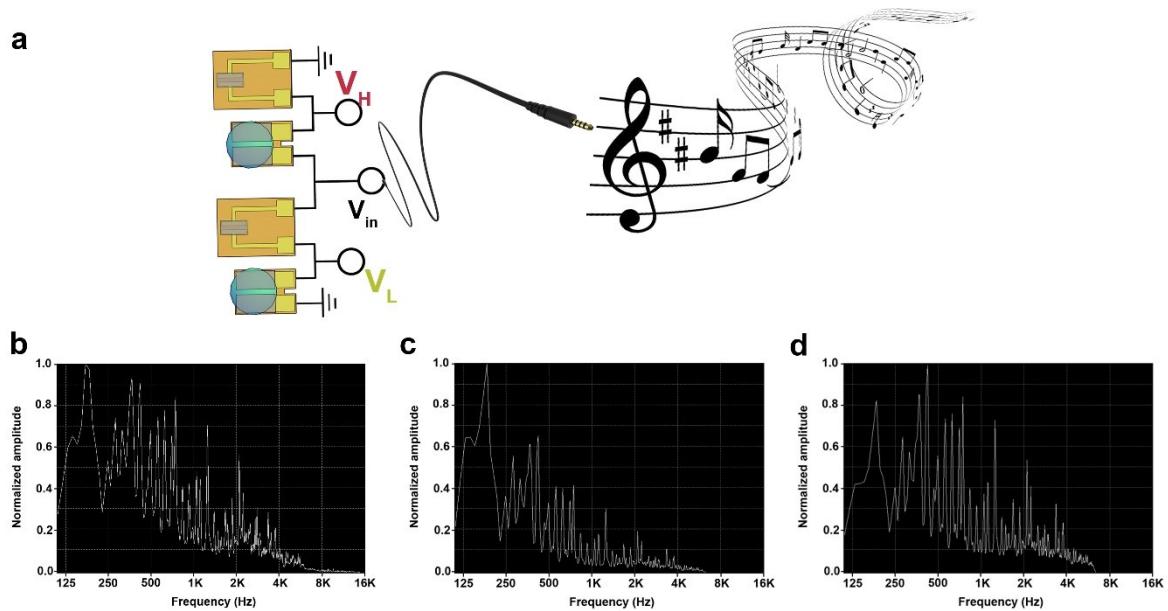
Figure 30. a) Connection layout for paired low- and high- pass organic filter for digitalised audio track sorting, b) Normalized input signal spectrum, c) Normalized low-pass output signal spectrum, d) Normalized high-pass output signal spectrum.

In this case the paired organic RC filters are exploited to perform audio equalization. An audio track, namely 7 seconds of the introduction of "Sweet Child Of Mine" by Guns 'n Roses, is converted in a voltage versus time signal, as described in Section 4.9. The voltage track is used as V_{IN} for the filter architecture and V_L and V_H are collected. **Figure 30 b** depicts the spectra of the untreated input signal, the low-passed signal spectrum is shown in **Figure 30 c**, and the high-passed signal spectrum is reported in **Figure 30 d**. It is possible to notice in **Figure 30 c** and **d** how the normalized amplitude of the low-pass and high-pass spectra strongly differ in terms of frequency contribution. In **Figure 30 c** a major content of frequency between 120 and 250 Hz can be observed respect to the high-passed spectra, **Figure 30 d**, in

which the dominant spectral contribution is that of frequencies higher than 250 Hz.

In conclusion, the designed basic circuit allows the factorization of a complex and layered multi-frequency signal, both in frequency and in amplitude and it can be easily implemented both with EGOTs and electrodes. Moreover, since all the components are made with polyimide and PEDOT:PSS, the most used materials in biomedical engineering of electronic organic devices, they can be tailored (by changing either device geometrical parameters or the organic materials used for capacitor and resistors)and engineered in implantable devices to segment information in an *operando* regime.

BIBLIOGRAPHY

1. Liu, X., Zhang, M., Richardson, A. G., Lucas, T. H. & Van der Spiegel, J. Design of a Closed-Loop, Bidirectional Brain Machine Interface System With Energy Efficient Neural Feature Extraction and PID Control. *IEEE Trans. Biomed. Circuits Syst.* **11**, 729–742 (2017).

2. Zhou, A. *et al.* A wireless and artefact-free 128-channel neuromodulation device for closed-loop stimulation and recording in non-human primates. *Nat. Biomed. Eng.* **3**, 15–26 (2018).

3. Seu, G. P. *et al.* Exploiting All Programmable SoCs in Neural Signal Analysis: A Closed-Loop Control for Large-Scale CMOS Multielectrode Arrays. *IEEE Trans. Biomed. Circuits Syst.* **12**, 839–850 (2018).

4. Friedlein, J. T., McLeod, R. R. & Rivnay, J. Device physics of organic electrochemical transistors. *Org. Electron.* **63**, 398–414 (2018).

5. Friedlein, J. T. *et al.* Influence of disorder on transfer characteristics of organic electrochemical transistors. *Appl. Phys. Lett.* **111**, 023301 (2017).

6. Tyrrell, J. E., Boutelle, M. G. & Campbell, A. J. Measurement of Electrophysiological Signals In Vitro Using High-Performance Organic Electrochemical Transistors. *Adv. Funct. Mater.* **31**, 1–12 (2021).

7. Liang, Y. *et al.* Tuning Channel Architecture of Interdigitated Organic Electrochemical Transistors for Recording the Action Potentials of Electrogenic Cells. *Adv. Funct. Mater.* **29**, 1902085 (2019).

8. Rivnay, J. *et al.* High-performance transistors for bioelectronics through tuning of channel thickness. *Sci. Adv.* **1**, e1400251 (2015).

9. Khodagholy, D. *et al.* In vivo recordings of brain activity using organic transistors. *Nat. Commun.* **4**, 1575 (2013).

10. Dickson R. Yao & Dion Khodagholy. Translational Neuroelectronics. in *ntroduction to Bioelectronics: Materials, Devices, and Applications* 7, chapter 7 ([AIP Publishing (online), Melville, New York, 2022]Eleni Stavrinidou and Christopher M. Proctor).

11. Conant, D., Bouchard, K. E. & Chang, E. F. Speech map in the human ventral sensory-motor cortex. *Curr. Opin. Neurobiol.* **24**, 63–67 (2014).

12. Bouchard, K. E., Mesgarani, N., Johnson, K. & Chang, E. F. Functional organization of human sensorimotor cortex for speech articulation. *Nature* **495**, 327–332 (2013).

13. Chang, E. F., Wang, D. D., Perry, D. W., Barbaro, N. M. & Berger, M. S. Homotopic organization of essential language sites in right and bilateral cerebral hemispheric dominance: Clinical article. *J. Neurosurg.* **114**, 893–902 (2011).

14. Chang, E. F. *et al.* Categorical speech representation in human superior temporal gyrus. *Nat. Neurosci.* **13**, 1428–1432 (2010).

15. Yao, P.-S., Zheng, S.-F., Wang, F., Kang, D.-Z. & Lin, Y.-X. Surgery guided with intraoperative electrocorticography in patients with low-grade glioma and refractory seizures. *J. Neurosurg.* **128**, 840–845 (2018).

16. Bertani, G. *et al.* Intraoperative mapping and monitoring of brain functions for the resection of low-grade gliomas: technical considerations. *Neurosurg. Focus* **27**, E4 (2009).

17. Hill, N. J. *et al.* Recording Human Electrocorticographic (ECoG) Signals for Neuroscientific Research and Real-time Functional Cortical Mapping. *J. Vis. Exp.* 3993 (2012) doi:10.3791/3993.

18. Chan, A. Y., Knowlton, R. C., Chang, E. F. & Rao, V. R. Seizure localization by chronic ambulatory electrocorticography. *Clin. Neurophysiol. Pract.* **3**, 174–176 (2018).

19. DiLorenzo, D. J., Mangubat, E. Z., Rossi, M. A. & Byrne, R. W. Chronic unlimited recording electrocorticography–guided resective epilepsy surgery: technology-enabled enhanced fidelity in seizure focus localization with improved surgical efficacy: Clinical article. *J. Neurosurg.* **120**, 1402–1414 (2014).

20. Romanelli, P. *et al.* A novel neural prosthesis providing long-term electrocorticography recording and cortical stimulation for epilepsy and brain-computer interface. *J. Neurosurg.* **130**, 1166–1179 (2019).

21. Volkova, K., Lebedev, M. A., Kaplan, A. & Ossadtchi, A. Decoding Movement From Electrocorticographic Activity: A Review. *Front. Neuroinformatics* **13**, 74 (2019).

22. Schalk, G. & Leuthardt, E. C. Brain-Computer Interfaces Using Electrocorticographic Signals. *IEEE Rev. Biomed. Eng.* **4**, 140–154 (2011).

23. Kellis, S. *et al.* Multi-scale analysis of neural activity in humans: Implications for micro-scale electrocorticography. *Clin. Neurophysiol.* **127**, 591–601 (2016).

24. Vinjamuri, R. *et al.* A fuzzy logic model for hand posture control using human cortical activity recorded by micro-ECog electrodes. in *2009 Annual International Conference of the IEEE Engineering in Medicine and Biology Society* 4339–4342 (IEEE, 2009). doi:10.1109/IEMBS.2009.5332746.

25. Miller, K. J. *et al.* Spectral Changes in Cortical Surface Potentials during Motor Movement. *J. Neurosci.* **27**, 2424–2432 (2007).

26. Gunduz, A. *et al.* Neural Correlates of Visual?Spatial Attention in Electrocorticographic Signals in Humans. *Front. Hum. Neurosci.* **5**, (2011).

27. Buzsáki, G., Anastassiou, C. A. & Koch, C. The origin of extracellular fields and currents-EEG, ECoG, LFP and spikes. *Nat. Rev. Neurosci.* **13**, 407–420 (2012).

28. Cogan, S. F. Neural stimulation and recording electrodes. *Annu. Rev. Biomed. Eng.* **10**, 275–309 (2008).

29. Ansaldo, A., Castagnola, E., Maggiolini, E., Fadiga, L. & Ricci, D. Superior Electrochemical Performance of Carbon Nanotubes Directly Grown on Sharp Microelectrodes. *ACS Nano* **5**, 2206–2214 (2011).

30. Qing, Q. *et al.* Nanowire transistor arrays for mapping neural circuits in acute brain slices. *Proc. Natl. Acad. Sci.* **107**, 1882–1887 (2010).

31. Yin, L. *et al.* Silicon Nanomembranes: Mechanisms for Hydrolysis of Silicon Nanomembranes as Used in Bioresorbable Electronics (Adv. Mater. 11/2015). *Adv. Mater.* **27**, 1856–1856 (2015).

32. Chiang, C.-H. *et al.* Development of a neural interface for high-definition, long-term recording in rodents and nonhuman primates. *Sci. Transl. Med.* **12**, eaay4682 (2020).

33. Di Lauro, M. *et al.* Liquid-Gated Organic Electronic Devices Based on High-Performance Solution-Processed Molecular Semiconductor. *Adv. Electron. Mater.* **3**, 1700159 (2017).

34. Cea, C. *et al.* Enhancement-mode ion-based transistor as a comprehensive interface and real-time processing unit for in vivo electrophysiology. *Nat. Mater.* **19**, 679–686 (2020).

35. Berto, M. *et al.* Label free urea biosensor based on organic electrochemical transistors. *Flex. Print. Electron.* **3**, 024001 (2018).

36. Diamond, M. E., von Heimendahl, M., Knutsen, P. M., Kleinfeld, D. & Ahissar, E. 'Where' and 'what' in the whisker sensorimotor system. *Nat. Rev. Neurosci.* **9**, 601–612 (2008).

37. Petersen, C. C. H. The Functional Organization of the Barrel Cortex. *Neuron* **56**, 339–355 (2007).

38. Rivnay, J. *et al.* Organic Electrochemical Transistors with Maximum Transconductance at Zero Gate Bias. *Adv. Mater.* **25**, 7010–7014 (2013).

39. Tyrrell, J. E., Boutelle, M. G. & Campbell, A. J. Measurement of Electrophysiological Signals In Vitro Using High-Performance Organic Electrochemical Transistors. *Adv. Funct. Mater.* **31**, 2007086 (2021).

40. Chari, A., Thornton, R. C., Tisdall, M. M. & Scott, R. C. Microelectrode recordings in human epilepsy: a case for clinical translation. *Brain Commun.* **2**, fcaa082 (2020).

41. Harris, K. D., Quiroga, R. Q., Freeman, J. & Smith, S. L. Improving data quality in neuronal population recordings. *Nat. Neurosci.* **19**, 1165–1174 (2016).

42. Khodagholy, D. *et al.* NeuroGrid: recording action potentials from the surface of the brain. *Nat. Neurosci.* **18**, 310–315 (2015).

43. Vomero, M. *et al.* Conformable polyimide-based µECoGs: Bringing the electrodes closer to the signal source. *Biomaterials* **255**, 120178 (2020).

44. Vomero, M. *et al.* Achieving Ultra-Conformability With Polyimide-Based ECoG Arrays. in *2018 40th Annual International Conference of the IEEE Engineering in Medicine and Biology Society (EMBC)* vols 2018-July 4464–4467 (IEEE, 2018).

45. Vomero, M. *et al.* Flexible Bioelectronics: Flexible Bioelectronic Devices Based on Micropatterned Monolithic Carbon Fiber Mats (Adv. Mater. Technol. 2/2020). *Adv. Mater. Technol.* **5**, 2070009 (2020).

46. Luan, L. *et al.* Ultraflexible nanoelectronic probes form reliable, glial scar–free neural integration. *Sci. Adv.* **3**, e1601966 (2017).

47. Han, S., Polyravas, A. G., Wustoni, S., Inal, S. & Malliaras, G. G. Integration of Organic Electrochemical Transistors with Implantable Probes. *Adv. Mater. Technol.* **6**, 2100763 (2021).

48. D'Angelo, P. *et al.* Scaling Organic Electrochemical Transistors Down to Nanosized Channels. *Small* **15**, 1–13 (2019).

49. Pecqueur, S., Lenfant, S., Guérin, D., Alibart, F. & Vuillaume, D. Concentric-electrode organic electrochemical transistors: Case study for selective hydrazine sensing. *Sens. Switz.* **17**, (2017).

50. Tarabella, G. *et al.* Effect of the gate electrode on the response of organic electrochemical transistors. *Appl. Phys. Lett.* **97**, 123304 (2010).

51. Colucci, R., Barbosa, H. F. D. P., Günther, F., Cavassin, P. & Faria, G. C. Recent advances in modeling organic electrochemical transistors. *Flex. Print. Electron.* **5**, (2020).

52. Even-Chen, N. *et al.* Power-saving design opportunities for wireless intracortical brain–computer interfaces. *Nat. Biomed. Eng.* **4**, 984–996 (2020).

53. Kendall, J. D. & Kumar, S. The building blocks of a brain-inspired computer. *Appl. Phys. Rev.* **7**, 011305 (2020).

54. Di Lauro, M. *et al.* Photovoltage generation in enzymatic bio-hybrid architectures. *MRS Adv.* **5**, 985–990 (2020).

55. Di Lauro, M. *et al.* A Bacterial Photosynthetic Enzymatic Unit Modulating Organic Transistors with Light. *Adv. Electron. Mater.* **6**, 1900888 (2020).

56. Giordani, M. *et al.* Neuromorphic Organic Devices that Specifically Discriminate Dopamine from Its Metabolites by Nonspecific Interactions. *Adv. Funct. Mater.* **30**, (2020).

57. Clarke, G. A. *et al.* Advancement of Sensor Integrated Organ-on-Chip Devices. *Sensors* **21**, 1367 (2021).

58. Di Lauro, M. *et al.* A Novel Biasing Scheme of Electrolyte-Gated Organic Transistors for Safe In Vivo Amplification of Electrophysiological Signals. *Adv. Mater. Interfaces* **9**, 2101798 (2022).

59. Khodagholy, D. *et al.* Organic electronics for high-resolution electrocorticography of the human brain. *Sci. Adv.* **2**, e1601027 (2016).

60. Di Lauro, M. *et al.* Tunable Short-Term Plasticity Response in Three-Terminal Organic Neuromorphic Devices. *ACS Appl. Electron. Mater.* **2**, 1849–1854 (2020).

61. Gkoupidenis, P., Schaefer, N., Garlan, B. & Malliaras, G. G. Neuromorphic Functions in PEDOT:PSS Organic Electrochemical Transistors. *Adv. Mater.* **27**, 7176–7180 (2015).

62. Harikesh, P. C. *et al.* Organic electrochemical neurons and synapses with ion mediated spiking. *Nat. Commun.* **13**, 901 (2022).

63. Gkoupidenis, P., Koutsouras, D. A. & Malliaras, G. G. Neuromorphic device architectures with global connectivity through electrolyte gating. *Nat. Commun.* **8**, (2017).

64. Rondelli, F. *et al.* Pre-synaptic DC bias controls the plasticity and dynamics of three-terminal neuromorphic electrolyte-gated organic transistors. *Neuromorphic Comput. Eng.* (2023) doi:10.1088/2634-4386/acb37f.

Conclusions and perspectives

This thesis addresses the topic of applying organic bioelectronics, specifically electrolyte-gated organic transistors, in translational neuroscience through assessment of device performance, and design, fabrication, and validation *in vitro* and *in vivo* of novel EGOT-based architectures. The two main conceptual fields in which the findings of this thesis are enclosed are organic neuromorphic electronics and organic neuroelectronics.

In terms of neuromorphic electronics, it has been possible to mimic and define two distinct synaptic plasticity events, namely short-term plasticity and paired-pulse plasticity, using a single device architecture. A novel connection layout was devised and validated for the former, achieving reversible fine-tuning of the STP response as well as a frequency dependent switching memory by operating on the gate potential. It has been feasible to establish four key scenarios for the latter by modifying the inter-stimulation interval, which can be addressed as a learning rule that defines how a specific type of synapse participates in information storage and, ultimately, brain-like circuit operation.

This thesis adds to previous of knowledge about EGOT in translational neurophysiology. To begin with, a novel biasing strategy for EGOT operation has been implemented in order to prevent the administration of a bias to the brain during electrophysiological measurements. This novel connection layout, namely the common drain/grounded source, was tested in vitro by presenting an empirical model which estimates the safest voltage window which enable EGOTs operation at maximum transconductance. Furthermore, CDGS-EGOTs were assessed *in vivo* and compared to electrode, with area equal to the gate electrode, in terms of signal-to-noise ratio and minimum trail number to achieve a reliable SEP estimation, indicating that EGOT not only promotes a greater SNR but is also strongest in event recognition at the single trail level. This is a crucial feature in the proper deployment of brain-machine interfaces, which are subjected to a constant

flow of diverse neurological input that must be resolved in real time. An organic circuit for sorting and amplification has been provided for this purpose, with the goal of implementing a bio-integrable circuit for BMIs. This architecture is amenable to downsizing and implementation in conformable bio-integrable circuits for *in operando* filtering due to *ad hoc* choice of materials and of connection schemes.

Additionally, polyimide-based conformable micro-epicortical arrays using paired source and drain electrodes as recording sites were designed, manufactured with MEMs processing, and characterized *in vitro*. In the designed arrays, organic transistors are obtained via electrodeposition of PEDOT/PSS in the absence of additives, to achieve controlled thickness and entirely translational multi-species transistor arrays, MuSTAs.

As a prompt follow-up to this research activity, i) MuSTA will be optimized and tested in animal models, with the goal of establishing new electrophysiological signal acquisition methodologies tailored to this technology platform; ii) The organic filtering circuit will be improved and miniaturized and included into the transduction chain for electrophysiological signal acquisition.

The technological and operational apparatus developed during this thesis will aid in disentangling the complex evolution of organic electronic device performances at the interface with biology, as well as in providing technological routes for the development of novel electronic devices capable of autonomous unsupervised bidirectional interaction with the nervous system.
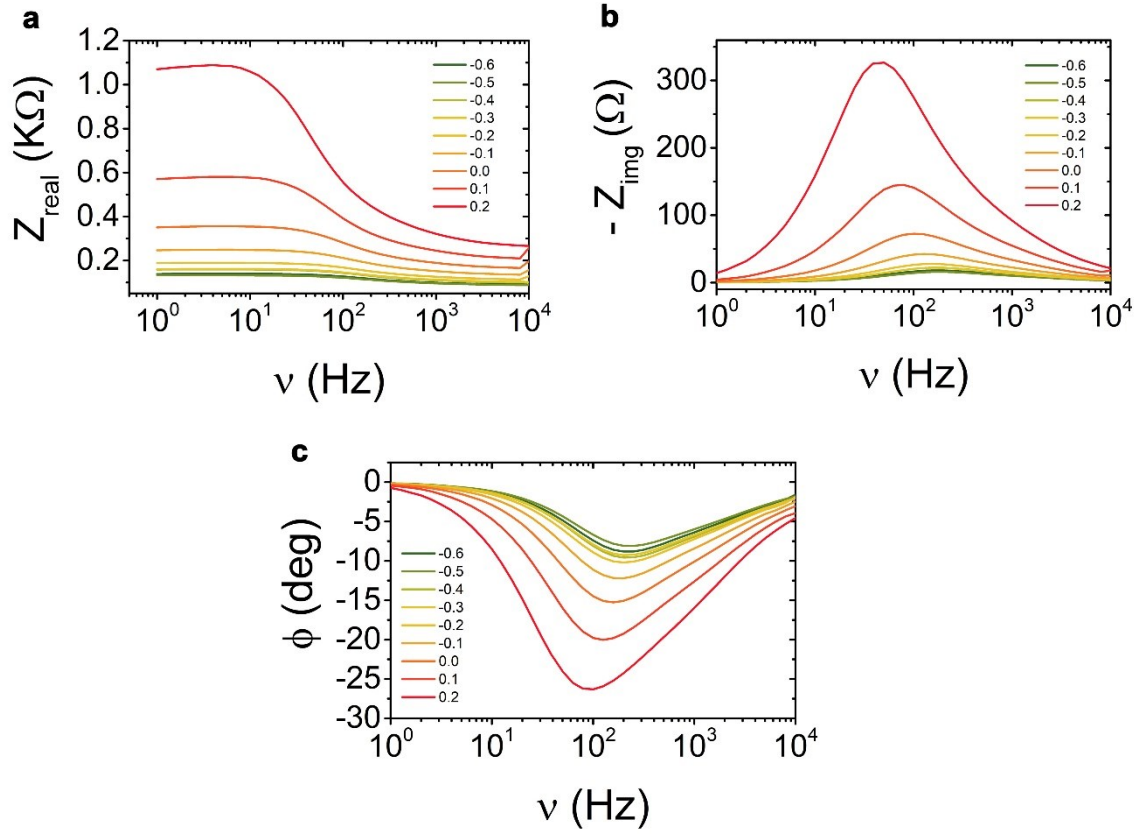
Figure 1. Channel impedance spectroscopy has been recorded at the drain electrode in two-electrodes configuration, using the source electrode as both counter and reference electrode. an external source has been used to provide dc gate bias during measurement. bode plots of real component (a), imaginary component (b) and phase (c) are reported. frequency values corresponding to maxima in (b) and in (c) have been used for the calculation of circuit time constant, τ, according to the well-known $\tau = \frac{1}{2\pi v}$
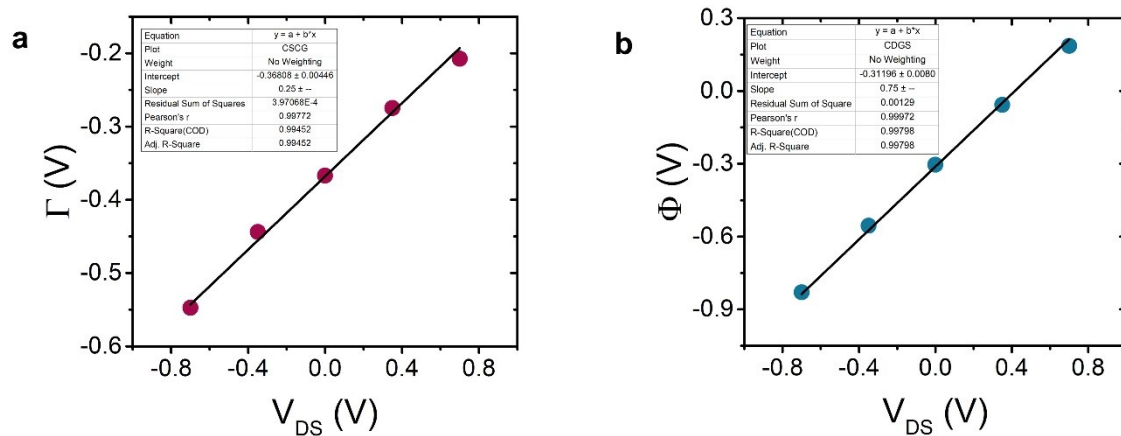
Figure 1. Dependency of Γ and Φ on V_{DS}. a) Linear fit, Γ vs V_{DS}, (black line) with fixed slope equals to 0.25. The slope was fixed at this value after different iteration on different data set. b) Linear fit, Φ vs V_{DS}, (black line) with fixed slope equals to 0.75. The slope was fixed at this value after different iteration on different data set.
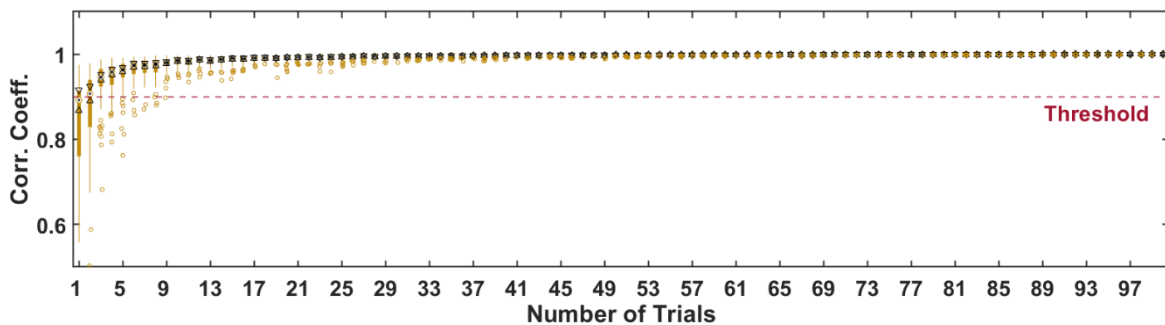
Figure 2. Correlation analysis of voltage recordings. Box-plots (in yellow) of the correlation coefficient values computed between V_{EI} averaged over 100 randomly selected trial groups and V_{EI} averaged over all trials (n=100), iterated increasing group numerosity by steps of 1, reported vs group numerosity. Dashed red line indicates the selected threshold to achieve a reliable estimation of the somatosensory evoked response. Here minimum trial number to obtain a correlation higher than 90% is 3.

SPECS:

Total device length — 3.1 cm

Track body length — 2.3 cm

Total number of pair of gold electrodes — 16

Diameters(from the largest to the smallest)— 390-330-160-100 µm

Distance between two pairs of electrodes — 60 µm

Center to center distance — 750 µm

Total working area—8.399 mm^2

Elecodre trace width — 25 µm

Channel length — 5 µm

External channel width — 877.818 µm

Inner channel width — 299.102 µm

Trace width in the track body — 30 µm

Trace clearence in the track body — 35 µm

Figure 1. Concentric Electrodes Array. a) Electrolyte-Gated Organic Transistors-based test matrix featuring ZIF connector. Tracks and active sites specs are equal to neuroprostehsis parameters. b) Electrolyte-Gated Organic Transistors-based Neuroprosthesis featuring an OMNECTICS connector. c) Recording area featuring 8 recording sites. d) Zoom of a recording site featuring two couple of electrodes depute to be EGOTs channel and or gate.

SPECS:

Total device length — 3.1 cm

Track body length — 2.16 cm

Total number of pair of gold electrodes — 16

Distance between two pairs of electrodes — 60 µm

Center to center distance — 750 µm

Total working area—10.623 mm^2

Elecodre trace width — 25 µm

Channel length — 5 µm

External channel width — 1181.15 µm

Inner channel width — 819.87 µm

Trace width in the track body — 30 µm

Trace clearence in the track body — 35 µm

Figure 2 . U-shape Electrodes Array. a) Electrolyte-Gated Organic Transistors-based test matrix featuring ZIF connector. Tracks and active sites specs are equal to neuroprostehsis parameters. b) Electrolyte-Gated Organic transistors-based Neuroprosthesis featuring an OMNETICS connector. c) Recording area featuring 8 recording sites. d) Zoom of a recording site featuring two couple of electrodes depute to be EGOTs channel or gate.
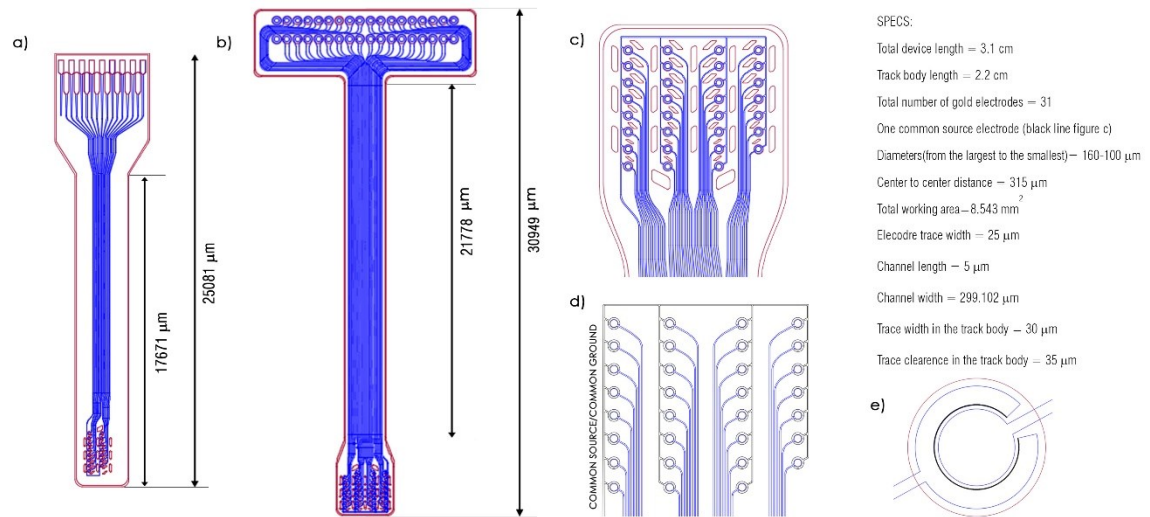
Figure 3. Circle Electrodes Array. a) Electrolyte-Gated Organic Transistors-based test matrix feauturing ZIF connector. Tracks and active sites specs are equal to neuroprostehsis parameters. b) Electrolyte-Gated Organic transistors-based Neuroprosthesis feauturing an OMNETICS connector. c) Recording area featuring 31 recording sites. d) Recording area featuring a common source/common ground electrode (black line). e) Zoom of a recording site featuring two couple of electrodes depute to be EGOTs channel or gate.

List of figures

with V_{GS}, c) 3-D output curve V_{DS} vs V_{GS} vs I_{DS} showing the current amplitude attenuation in steady-state EGOT characterisation, mirroring current amplitude scaling in STP response. 90

157

List of abbreviations

Abb.	Long form
µ-ECOG	Micro-electrocorticography
AC	Alternating current
AFM	Atomic force microscopy
ANNs	Artificial neural networks
BMI	Brain-machine interface
CDGS	Common-drain/Grounded source
CNS	Central Nervous System
CPS	Conductive polymers
CSC	Charge storage capacitance
CSCG	Common-source/common-ground
D	Drain
DC	Direct current
DMSO	Dimethyl sulphoxide
ECOG	Electrocorticography
EDOT	3,4-ethylenedioxythiophene
EEG	Electroencephalogram
EG	Ethylene glycol
EGOFET	Electrolyte-gated organic field-effect transistors
EGOTs	Electrolyte-Gated Organic Transistors
FBR	Foreign body reaction
fc	Cut-off frequency
G	Gate
GOPS	Glycidyloxypropyl-trimethoxysilane
I-V	Current-voltage
LFP	Local field potential
ltd	Long-term depression
LTP	Long-term plasticity
ltp	Long-term potentiation
MEA	Multi-electrode array

MEM	Microelectromechanical system
MOSFET	Metal-oxide-semiconductor field-effect transistor
MuSA	Multi-species Array
MuSTA	Multi-Species Transistor Array
NAPSS	Sodium poly-styrene sulfonate
OECNS	Organic electrochemical neurons
OECTS	Organic electrochemical transistors
OFET	Organic field-effect transistor
OHL	Outer Helmholtz layer
OMIECS	Mixed ionic-electronic conductors
PAR	Parylene
PBS	Phosphate Buffered Saline
PCB	Printed circuit board
PDMS	Polydimethylsiloxane
PEDOT	Poly(3,4ethylenedioxythiophene)
PI	Polyimide
PPP	Paired-pulse plasticity
PSS	Poly-(styrene sulfonate)
RIE	Reactive-ion-etching
S	Source
SEP	Somatosensory evoked potential
SMU	Source/Measure Units
SNR	Signal-to-noise ratio
STDP	Spike-timing-dependent plasticity
STP	Short-term plasticity
w	Synaptic weight
ZIF	Zero insertion force

Acknowledgements